

4558

UNIVERSITY OF HAWAII LIBRARY

MAGMA DEGASSING DURING THE 1912 ERUPTION OF NOVARUPTA,  
ALASKA: TEXTURAL ANALYSES OF PYROCLASTS REPRESENTING  
CHANGES IN ERUPTIVE INTENSITY AND STYLE

A DISSERTATION SUBMITTED TO THE GRADUATE DIVISION OF THE  
UNIVERSITY OF HAWAII IN PARTIAL FULFILLMENT OF THE  
REQUIREMENTS FOR THE DEGREE OF

DOCTOR OF PHILOSOPHY

IN

GEOLOGY AND GEOPHYSICS

MAY 2005

By  
Nancy K. Adams

Dissertation Committee:

Bruce F. Houghton, Chairperson  
Michael Garcia  
Julia Hammer  
Andrew Harris  
Scott Rowland  
David Muenow

## ACKNOWLEDGEMENTS

Previous work by Wes Hildreth, Judy Fierstein, and Colin Wilson established a stratigraphic framework for this project, and their untiring efforts continue to provide insights into eruption details. I would also like to thank Sarah Fagents for her contribution towards the modeling of dome disruption through Vulcanian explosions. Lucia Gurioli showed undying patience and fortitude when helping to establish image analysis techniques. This research would not have been possible without the continued support and guidance of my committee members. I especially have to thank my advisor, Bruce Houghton, for his support and patience as well as the incredible amount of time, attention, and effort he spent contributing to this dissertation and my graduate education. This work was supported by the National Science Foundation (NSF) grant EAR-01-06700. Images were collected on the scanning electron microscope (SEM) belonging to HIGP (Hawaii Institute of Geophysics & Planetology).

## ABSTRACT

Three episodes of explosive activity occurred during the 1912 eruption of Novarupta, Alaska before a switch to effusive dome growth. Episode I was characterized by two chemically distinct magmas erupting in steadily changing proportions with contemporaneous generation of ignimbrites and Plinian fall deposits. Episodes II and III followed and were classical plinian events characterized by a stable plume generating a succession dominated by fall deposits of chemically homogeneous dacitic pumice. Episode IV is defined by the extrusion of a texturally heterogeneous ephemeral dacite dome/plug destroyed through Vulcanian explosions and hence recorded only in an apron of blocks. A rhyolitic melt then emerged and created the stable Episode V dome which occupies the vent today. This dissertation explores the influence of conduit process, e.g., vesiculation and degassing, on these events.

Pumice from the waxing and stable Plinian phases (episodes I-III) of the eruption show similar vesiculation histories. Strong, disequilibrium degassing and delayed nucleation and growth of vesicles produced high vesicularities, thin glass walls, high bubble number densities ( $10^8$  to  $10^9$  cm<sup>-3</sup>), and a predominance of bubbles of diameter 50 to 125  $\mu$ m. Early bubble growth was controlled by diffusion and decompression, but at a bubble size  $\sim$ 30  $\mu$ m in diameter, coalescence became the dominant manner of growth. However, the earliest erupted rhyolitic pumice from Episode I and the last erupted dacite clasts in Episode III were exceptions with different vesiculation and presumably ascent histories. Early rhyolitic pyroclasts show stretched bubbles which are consistent with

shearing during the opening of the conduit. During Episode III, successive samples shift towards a decreased mean vesicularity, and textures are increasingly controlled by bubble collapse which foreshadowed the shift to decoupled degassing and episodes IV and V dome extrusion.

Based on the 1912 fall deposits, pauses in eruptive activity were caused by internal changes to melt rheology in the conduit as well as external forces, e.g., changes in vent geometry. On a longer time scale, slowed magma ascent and degassing, probably beginning in portions of the melt along the margins of the conduit, led to a permanent shift from explosive to effusive eruption style.

## TABLE OF CONTENTS

Acknowledgements.....	iii
Abstract.....	iv
List of Tables.....	xi
List of Figures.....	xii
Chapter 1. Introduction.....	1
1.1 Dissertation goal and objectives.....	1
1.2 Perspectives and philosophies.....	1
1.2.1 Controls on the style and intensity of explosive volcanism.....	2
1.2.2 Magma ascent in the conduit and its signature on pyroclasts.....	4
1.2.3 Vent/conduit structure and its influence on eruptive conditions.....	6
1.3 The study.....	7
1.3.1 The 1912 Novarupta eruption.....	7
1.3.2 Structure of dissertation.....	10
1.3.3 Methodology.....	11
1.3.4 Contributions.....	16
Chapter 2. Abrupt transitions during sustained explosive eruptions: examples from the 1912 eruption of Novarupta, Alaska.....	17
2.1 Abstract.....	17
2.2 Introduction.....	18
2.3 Background.....	20
2.3.1 Eruption description.....	20

2.3.2 Episode II/III stratigraphy.....	21
2.3.3 Melt properties and storage.....	22
2.4 Techniques.....	23
2.4.1 Sample collection.....	23
2.4.2 Density/vesicularity.....	24
2.4.3 Image analysis.....	24
2.5 Results.....	28
2.5.1 Density.....	28
2.5.2 Qualitative observations of vesicles.....	29
2.5.3 Quantitative vesicle size data.....	32
2.5.3.1 Vesicle size distributions.....	32
2.5.3.2 Vesicle volume distributions.....	33
2.5.3.3 Cumulative number densities.....	35
2.6 Interpretation.....	36
2.6.1 Bubble nucleation.....	36
2.6.2 Bubble coalescence.....	40
2.6.3 Bubble collapse: maturation of texture.....	42
2.7 Discussion.....	43
2.7.1 Diversity within samples: heterogeneity in the conduit.....	43
2.7.2 Diversity between samples: temporal changes within an episode.....	45
2.7.3 Pauses and breaks in the Novarupta eruption.....	46
2.8 Conclusions.....	48

2.9 Acknowledgements.....	48
Chapter 3. The transition from explosive to effusive eruptive regime: the example of the 1912 Novarupta eruption, Alaska .....	65
3.1 Abstract.....	65
3.2 Introduction.....	66
3.3 Background.....	68
3.3.1 Explosive and effusive behavior.....	68
3.3.2 Microtextures .....	69
3.3.3 The 1912 eruption.....	70
3.4 The Episode IV block bed .....	71
3.4.1 Field methods.....	71
3.4.1.1 Block size and distribution.....	71
3.4.1.2 Block componentry.....	72
3.4.2 Distribution of ejecta.....	73
3.4.2.1 Data.....	73
3.4.2.2 Interpretation.....	74
3.4.3 Block componentry and morphology.....	75
3.4.3.1 Data.....	75
3.4.3.2 Interpretation.....	76
3.5 Vesicularity of juvenile material.....	77
3.5.1 Techniques .....	77
3.5.2 Density and bulk vesicularity data.....	78
3.5.3 Qualitative observations of vesicularity.....	78

3.5.4 Quantitative observations of vesicularity.....	81
3.5.5 Interpretation.....	82
3.6 Dynamics of block bed emplacement.....	84
3.6.1 Methodology and model parameters.....	84
3.6.2 Results.....	86
3.7 Discussion and conclusions .....	87
3.7.1 Magma ascent and degassing.....	87
3.7.2 Model for dome fragmentation.....	90
3.8 Acknowledgements.....	91
Chapter 4. Episode I: variations in vesiculation and changes in vent geometry and eruptive composition.....	109
4.1 Abstract.....	109
4.2 Introduction.....	110
4.2.1 Magma ascent and degassing.....	110
4.2.2 Goals .....	111
4.3 Previous work .....	112
4.3.1 Eruptive sequence .....	112
4.3.2 Vent structure.....	114
4.4 Current study.....	115
4.4.1 Methods.....	115
4.4.2 Density and bulk vesicularity.....	116
4.4.3 Qualitative observations.....	118
4.4.4 Vesicle size data for selected clasts .....	120

4.5 Interpretation.....	122
4.5.1 Vesiculation history for Episode I melts.....	122
4.5.2 Signature of conduit formation during eruption of phase A.....	124
4.5.3 Comparison of coeval dacite and rhyolite .....	126
4.5.4 Contrasting behavior of dacitic melt during episodes I, II, and III.....	127
4.6 Conclusions.....	128
4.7 Acknowledgements.....	129
Chapter 5. Conclusions .....	145
5.1 Vesiculation and degassing processes during the 1912 eruption.....	145
5.2 General conclusions about vesiculation in silicic magma .....	148
5.3 Transition from closed to open system degassing in silicic magmas .....	149
5.4 Pauses and breaks during explosive silicic eruptions .....	150
5.5 Future directions .....	151
Appendix. Data repository .....	154
References.....	158

## LIST OF TABLES

<u>Table</u>		<u>Page</u>
2.1	Vesiculation parameters for samples from episodes II-III.....	49
3.1	Abundance of lithologies .....	92
3.2	Characteristics of lithologies.....	93
3.3	Vesiculation parameters for samples from episodes IV-V .....	94
4.1	Vesiculation parameters for samples from Episode I .....	130

## LIST OF FIGURES

<u>Figure</u>	<u>Page</u>
2.1 Compositions erupted with time.....	50
2.2 Vent photo.....	50
2.3 Stratigraphy at sample sites 94-1 and 94-Z.....	51
2.4 Density variations throughout episodes II-III.....	52
2.5 Density distributions throughout episodes II-III.....	53
2.6 Range of textures in episodes II-III clasts.....	54
2.7 Coalescence features.....	55
2.8 Qualitative observations of layers C, D, and F.....	56
2.9 High, modal, and low density clasts from Layer G.....	57
2.10 Natural log of population density against vesicle size.....	58
2.11 Volume fraction against vesicle size.....	59
2.12 Cumulative volume percent against vesicle size for layers C, D, F, and G.....	60
2.13 Cumulative volume percent against vesicle size for high, modal, and low density clasts from Layer G.....	60
2.14 Cumulative number density versus vesicle size.....	61
2.15 Onset of collapse.....	62
2.16 Evolution of conduit processes.....	63
2.17 Changes in and to the vent during episodes II-III.....	64
3.1 Photo mosaic of area covered by block bed.....	95
3.2 Photos of block bed.....	96
3.3 Photos of block lithologies.....	97

3.4	Componentry study sites.....	98
3.5	Distribution of block size.....	99
3.6	Distribution of block lithologies .....	100
3.7	Density distributions throughout episodes IV-V .....	101
3.8	Textures of pumiceous blocks .....	102
3.9	Textures of transitional and dense blocks.....	103
3.10	Textures of rhyolite dome (Episode V) .....	104
3.11	Distributions of vesicle volume for pumiceous blocks.....	105
3.12	Explosive conditions for observed block distribution .....	106
3.13	Illustration of eruption style during Episodes III and IV .....	107
3.14	Heterogeneity in Episode IV melt.....	108
4.1	Eruption style and composition with time during Episode I.....	131
4.2	Episode I eruption sequence .....	132
4.3	Vent photo.....	133
4.4	Dispersal of Episode I fall deposits .....	134
4.5	Plinian fall layers at site 89-1.....	135
4.6	Density variations throughout Episode I.....	136
4.7	Density variations throughout episodes II-III.....	137
4.8	Density distributions throughout Episode I .....	138
4.9	Large bubbles in Episode I rhyolite.....	139
4.10	Large bubbles in Episode I dacite.....	140
4.11	Small bubbles throughout Episode I.....	141

4.12	Rhyolite-dacite banded clast.....	142
4.13	Distributions of vesicle volume and number densities for Episode I clasts .....	143
4.14	Velocity and shear profiles .....	144

# CHAPTER 1

## Introduction

### 1.1 Dissertation goal and objectives

The goal of this dissertation was to understand controls and constraints on abrupt and gradational shifts in eruptive intensity and style during the largest eruption of the 21<sup>st</sup> century. Objectives were:

1. Establish mechanisms that drove brief pauses in and the termination of sustained Plinian volcanism.
2. Contrast patterns of ascent and degassing that lead to coeval production of voluminous ignimbrite and plinian fall deposits with those forming only fall units.
3. Contrast the textural diversity of the products of explosive and effusive activity and use this data to interpret contrasting histories of magma ascent and degassing that lead to periods of unstable and stable dome growth.
4. Model Vulcanian explosion(s) responsible for the destruction of a dome using dispersal and textural data.

### 1.2 Perspectives and philosophies

Pauses and/or abrupt shifts in eruptive intensity are a fundamental yet little studied part of many large explosive eruptions. Examples such as Mount St. Helens, May 18, 1980 (Waite and Dzurisin 1981), Pinatubo 1991 (Paladio-Melosantos et al. 1995), Krakatau 1883 (Self and Rampino 1981), El Chichon 1982 (Sigurdsson et al. 1984), and Vesuvius

79AD (Cioni et al. 1999) all demonstrate that stable Plinian plumes may pause or shift abruptly in intensity by several orders of magnitude. Many of these eruptions also show second-order fluctuations in intensity, as recorded by column height, on timescales of hours. The underlying causes of such shifts remain poorly understood while our models for steady state eruptive processes become increasingly elegant and sophisticated (Sparks 1986; Woods 1988; Bursik et al. 1992; Sparks et al. 1992; Koyaguchi 1994; Ernst et al. 1996; Sparks et al. 1997). The quality of hazard advice and eruption forecasts would be improved significantly if such changes could be explained and even anticipated. This study focuses on the origin of such unsteadiness in the largest powerful sustained explosive eruption of the 20<sup>th</sup> century. We examine both breaks in eruptive activity of several hours duration and abrupt transitions into first unstable and then permanent dome growth.

### **1.2.1 Controls on the style and intensity of explosive volcanism**

Changes in mass eruption rates (MER) have long been linked directly to changes in eruption style (Wilson et al. 1980; Jaupart 1996). For example, a decrease in MER from  $10^6$ - $10^8$  kg/s to the order of 0.1-1 m<sup>3</sup>/s (volumetric eruption rate) is seen during the shift from Plinian explosive to effusive activity (Fierstein and Hildreth 1992; Harris et al. 2003). However, more recent models recognize shifts in eruption style and intensity result from a complex system involving multiple feedback mechanisms and thus incorporate additional parameters (Jaupart 1996; Jaupart 1998; Massol and Jaupart 1999; Melnik and Sparks 1999; Melnik 2000; Barmin et al. 2002). The manner and rate of degassing (open- or closed-system), microlite crystallization, magma viscosity,

overpressures, and flow rate are all interconnected in these models and as such introduce nonlinearities into eruption dynamics. Numerical simulations are, however, always restricted; only certain parameters are allowed to vary, so abrupt transitions or pulsations in eruptive intensity/style as seen in natural systems are not well constrained. For example, the eruption at Novarupta, 1912 (as well those at Pinatubo 1991, Mount St. Helens 1980, Taupo 181, Spurr 1992, and Soufriere Hills 1995-1997) was characterized by both abrupt and progressive transitions in style and intensity and included simultaneous production of convecting columns and pyroclastic density currents. The complexity in natural systems highlights a current gap between identifying the broad parameters controlling eruption processes and understanding the interplay between processes.

Changing conditions within the magma chamber, the conduit, and the vent collectively influence eruption dynamics. In the magma reservoir, compositional gradients or the introduction of fresh pulses of new magma may affect the overpressure which drives the eruption (Eichelberger and Izbekov 2000). In the conduit, magma decompresses, loses volatiles, and can partially crystallize (Geschwind and Rutherford 1995; Wolf and Eichelberger 1997; Gardner et al. 1998) which induces changes in melt rheology thereby affecting eruption processes. In the vent or shallow conduit, environmental factors external to the magma influence eruption conditions, e.g., widening of the conduit, migration of the vent(s) (Hildreth and Mahood 1986; Suzuki-Kamata et al. 1993; Wilson and Hildreth 1997). The latter two environments are the focus of this study.

### **1.2.2 Magma ascent in the conduit and its signature on pyroclasts**

During magmatic fragmentation, part of the thermal energy of an expanding magma is converted to kinetic energy; this conversion generates the explosive force that drives eruptions (Cashman et al. 2000). It also directly binds the process of fragmentation to eruption dynamics. Recent numerical and experimental simulations suggest that magma fragments in a brittle fashion when the time-scale of deformation for rapidly accelerating melt in the conduit is shorter than the viscous relaxation time (Dingwell and Webb 1990; Dingwell 1996; Dingwell 1998). Melt fragmentation is thus critically related to ascent rate and to melt rheology which will itself alter in response to the changes in the concentrations of dissolved volatiles, bubbles, and microlites in the melt (Pinkerton and Stevenson 1992; Hess and Dingwell 1996; Manga et al. 1998; Stevenson et al. 1998). Eruption dynamics therefore reflect the relative rates of volatile exsolution, bubble growth, coalescence, and collapse, and degassing-induced crystallization during an eruption (Gardner et al. 1998; Hammer et al. 1999).

Syneruptive degassing processes occurring in the conduit pre-fragmentation can be studied using microtextural analysis (Sparks and Brazier 1982; Cashman and Mangan 1994). Theory developed for the interpretation of crystal size distributions (Cashman and Marsh 1988; Marsh 1988; Cashman 1992) has been applied to vesicle populations (Toramaru 1990; Cashman and Mangan 1994; Klug and Cashman 1994; Mangan and Cashman 1996). Textures of pyroclasts, specifically vesicle size distribution, vesicle shape, and abundance and morphology of microlites, can be quantified by image analysis. Vesicle size and volume distributions (VSDs, VVDs) can be used to relate the processes

of bubble nucleation, growth, coalescence, and collapse to magma ascent histories and their influence on ensuing eruptive behavior (Mangan et al. 1993; Cashman and Mangan 1994; Polacci et al. 2003). For example, size distributions can be presented as population density functions. Kinetic information such as growth rates can be derived from the slope and intercept of log-linear VSD plots (Cashman and Mangan 1994). The overall influence of processes such as prolonged nucleation, coalescence, and ripening on the VSD can also be discerned on these plots; each uniquely affects the size distribution and leaves a specific, identifiable signature (Mangan and Cashman 1996). VSDs and cumulative number densities can also be used to assess supersaturation pressures ( $\Delta P$ ) and degree of disequilibrium degassing according to the classical nucleation theory (Hurwitz and Navon 1994). Following Hirth et al. (1970), the relationship between nucleation rate and energy required for the formation of critical nuclei may be used to estimate  $\Delta P$ . Experimental decompression experiments such as Mangan and Sisson (2000) and Gardner et al. (1999) also provide insights into nucleation conditions for natural samples. Vesicle shape preserves information about the state of stress in the magma at the time of quenching (Marti et al. 1999). Stretching of bubbles is caused by stresses parallel to the flow in the conduit. Ascent velocities and shear profiles may change in response to changes in conduit/vent width (Cas and Wright 1987; Jaupart and Tait 1994; Dobran 2001), thus vesicle shapes can be related to shear profiles across the conduit (Marti et al. 1999; Polacci et al. 2001; Polacci et al. 2003).

### **1.2.3 Vent/conduit structure and its influence on eruption conditions**

Vent geometry and conduit diameter have a strong influence on eruption dynamics (Wilson et al. 1980; Bursik and Woods 1991; Woods and Bower 1995). Conduit width is intimately linked to ascent velocity, shear rates, and mass flux so that changes in one can force changes in another (Jaupart and Tait 1994). For example, plug flow and shear zones can develop in melt ascending within a conduit in response to an increase in conduit width (Dobran 2001). Velocity and shear profiles are themselves linked to the acceleration of the melt that accompanies the onset of vesiculation/degassing of the ascending magma (Polacci et al. 2001). Bubble stretching with a concomitant increase in permeability might occur in melt ascending along the conduit margins in the shear zones (Gonnermann and Manga 2003). This increased permeability might lead to open-system degassing, bubble collapse, and a shift from an explosive to an effusive eruption style (Gonnermann and Manga 2003). Thus, complex relationships and interdependencies between conduit radius, ascent rates, and vesiculation processes critically affect eruption regime. Initial opening and widening of a conduit and vent or narrowing by accumulation of degassed magma can be ascertained using the degree of vesicle elongation per sample. The proportion of melt affected by shear along the conduit walls decreases as conduit width increases and plug flow develops. Onset of permeability and open-system degassing can cause outgassed melt to accumulate on the conduit walls (Houghton et al. 2004a), effectively decreasing the effective conduit width and once again increasing shear and textural lineation.

Changes in vent dimensions or location and fragmentation depth may also be discerned by changes in the nature or abundance of vent-derived wall-rock particles in deposits (Eichelberger and Koch 1979; Wilson and Walker 1985; Suzuki-Kamata et al. 1993). For example, an increase in the amount of lithics might be expected with vent enlargement (Suzuki-Kamata et al. 1993). Likewise, a change in lithic type or lithology might indicate variations in the fragmentation depth in a conduit/vent cross-cutting stratified country rock (Barberi et al. 1989).

### **1.3 The study**

#### **1.3.1 The 1912 Novarupta eruption**

The June 6-8, 1912 eruption of Novarupta, Alaska, USA was the largest eruption of the 20<sup>th</sup> century, exceeded by only four eruptions in the last 1000 years and producing c. 11 km<sup>3</sup> of ignimbrite and c. 17 km<sup>3</sup> of Plinian fall deposits in ~ 60 hrs (Hildreth 1983; Hildreth 1987). Excellent preservation and a pronounced chemical zonation of the eruption products have been fundamental in developing a detailed medial-distal stratigraphy (Fierstein and Hildreth 1992) which has been augmented by detailed analysis of the nature and timing of the proximal deposits (Fierstein et al. 1997; Houghton et al. 2004b). The eruption had five eruptive episodes of first an explosive and then an effusive nature. The stratigraphy and eyewitness accounts point to two short breaks in eruptive activity on the morning of June 7 and the evening of June 8, defining the three episodes of explosive eruption (episodes I, II, and III). Explosive volcanism was followed by two episodes (IV-V) of dome emplacement. The Episode IV dome or plug was dacitic and

was entirely destroyed by Vulcanian explosive activity. It is now represented only by a block and lapilli apron to the west and south of the vent (Houghton et al. 2004b). This activity was followed by the extrusion of 0.005 km<sup>3</sup> of rhyolitic lava to form the current Novarupta dome during Episode V (Houghton et al. 2004b).

A lack of caldera collapse at the 1912 vent has preserved unusually complete proximal eruption products which reveal a complex, pulsatory pattern to near-vent deposition even during the episodes of sustained eruption (Houghton et al. 2004b). Three concentric, nested elements define the Novarupta vent region: the crater, the ejecta ring, and the dome. The crater is a 2-km wide depression representing a funnel-shaped flaring vent formed during Episode I and largely infilled with welded tuff by the end of that episode (Fierstein and Hildreth 1992). The ejecta ring is an asymmetric feature within the crater formed during episodes II and III and ranges in height from 7 m in the southwestern sector to up to 250 m in the northeast (Fierstein et al. 1997). The Episode V dome is 380 m wide and 65 m high and fills the narrow vent inferred to have been active during episodes II-V (Fierstein and Hildreth 1992).

The Plinian fall deposits cover a minimum area of 120,000 km<sup>2</sup> and were divided into eight layers (A through H) by Curtis (1968). Layers A+B, C+D, and F+G were formed during three sustained eruption episodes [I through III, respectively from Fierstein and Hildreth (1992)] and separated by breaks of a few hours. According to visual observations from aboard the steamer *Dora* and the record of tephra falls at Kodiak [Martin (1913), Griggs (1922), in Hildreth (1983)], an eruption column was first noticed at 1300 on 6 June. The time from this first sighting to the end of the first heavy ashfall

was 20 h; the second ashfall lasted ~26 h and the third ~10 h (Hildreth 1983; Fierstein and Hildreth 1992). A lithic-ash layer intercalated within Layer B is inferred to mark the onset of caldera collapse (Hildreth 1991). Between 0900 h and 1200 h on 7 June there was a break in ashfall at Kodiak (Hildreth 1983). If a 4-h time delay is assumed based on the recorded interval between the first sighting of the plinian column and the settling of the first ash at Kodiak, Episode I lasted ~16 h (Fierstein and Hildreth 1992). Signs of erosion or reworking are virtually nonexistent at the contact between Episode I and Episode II or between Episode II and Episode III. Fierstein and Hildreth (1992) infer that breaks between eruptive episodes were no longer than a few hours.

Each explosive episode demonstrated a complex mixture of eruptive styles and compositions. Episode I produced simultaneous pyroclastic falls and voluminous pyroclastic density currents (PDCs) during a progressive change in chemistry from all-rhyolite to dominantly dacite (Hildreth 1983; Hildreth 1991; Fierstein and Hildreth 1992). Fall layers A (all-rhyolite) and B (mixed rhyolite-dacite) and the main valley-filling ignimbrite that created the Valley of Ten Thousand Smokes (VTTS) were deposited by the end of this episode. The development of the conduit and vent added to the complexity of Episode I. Before the beginning of the eruption on 6 June, no vent existed at Novarupta (Fierstein and Hildreth 1992). The vent thus opened and enlarged to create a 2-km wide crater. By the end of Episode I, however, the vent had become established and nested within that outer crater (Fierstein and Hildreth 1992; Hildreth and Fierstein 2000). It remained relatively stable throughout episodes II-V, and the surface expression today is the Episode V lava dome. Episodes II and III deposited Plinian falls (layers C-

H) with only minor proximal intraplinian pyroclastic density currents and were predominantly dacitic in composition (Fierstein and Hildreth 1992).

### **1.3.2 Structure of dissertation**

The core of this dissertation is comprised of three chapters written as papers for scientific journals. As such, each chapter has its own abstract, introduction, background, results, and conclusion sections. Also, the figures for each paper are located at the end of each chapter. Each can read as a stand-alone study, but together they describe aspects of the full story of the 1912 eruption. Chapter 2 was submitted to the *Bulletin of Volcanology* and Chapter 3 to *GSA Bulletin*. Chapter 4 was written in the same format as Chapters 2 and 3 and will be submitted to a journal yet to be decided after completion of the dissertation. Chapter 5 is devoted to the broader conclusions reached in the perspective of the entire 1912 eruption.

In total, Chapters 2-4 cover selected aspects of the five defined episodes of the 1912 eruption. These chapters are presented in the order in which we studied the eruption, not sequentially from Episode I through IV. We started with episodes II and III because these episodes were characterized by a simple pattern of dacitic fall deposits from stable eruption plumes associated with a relatively unchanging vent in terms of geometry and location. Fluctuations and shifts in eruptive intensity were thus dominantly caused by the manner of degassing so that the influences of vesiculation processes and changes in the melt rheology could be extensively examined. Chapter 2 describes this study. Next, in Chapter 3, we examined episodes IV and V and applied the lessons learned concerning vesiculation processes in explosively erupted pyroclasts from

episodes II and III to blocks generated during the disruption of the ephemeral Episode IV dacite dome/plug as well as samples collected from the stable, effusively emplaced Episode V rhyolitic dome. Given the unstable nature of the Episode IV dome, I could study the nature and influence of degassing processes during a transition from explosive to effusive activity. Finally, in Chapter 4, I used Episode I to study the effects on textures of (1) initial vent opening and (2) changes in conduit-vent radius. Both (1) and (2) are associated with a convective column and contemporaneous ignimbrite generation at the time of a progressive compositional shift in the proportions of the dominant eruptive material. Episode I started with >90 % rhyolite but ended with >90% dacite (Hildreth 1983; Hildreth 1991; Fierstein and Hildreth 1992).

### **1.3.3 Methodology**

Novarupta has been the site of extensive fieldwork spanning almost 100 years. Early workers, including Martin, Griggs, Fenner, and Ziess (Hildreth 1983), began investigating the eruption as early as August of 1912. Several expeditions reached the VTTS between 1916 and 1923, but the eruption and its products remained poorly understood until a study by Curtis (1968). The current investigation is part of work that began in the early 1980s and has involved the United States Geological Survey (USGS) Volcano Hazards Program at Menlo Park, the Alaskan Volcanic Observatory (AVO), the University of Hawaii, and the Institute of Geological & Nuclear Sciences (IGNS) of New Zealand. An archive of samples, field notes, photos, and maps collected by Bruce Houghton during trips to Novarupta in 1991, 1994, 1995, 1997, 1998, and 1999 has

resided at the University of Hawaii – Manoa since 2000. Additions were made during recent trips in 2002 and 2003.

After exhaustive stratigraphic logging of sections in the proximal-distal region, key sample sites were selected to be used in a study of pyroclast-textures. Sites were chosen to represent the complete eruptive sequence. Two sets of 1994 samples were used to represent episodes II and III. Three new sites were logged and sampled in August 2003 for Episode I deposits. For episodes I-III, samples were collected from narrow vertical intervals (typically 2 or 3 clasts high) within the exposures to represent changes in style and/or intensity, i.e., transitions between and within eruptive units. Suites of samples of pumices were assembled from each site, and each sample was 50-100 clasts between 16-32 mm in diameter for each chemical composition present in the sample, i.e., dacite, rhyolite, etc. Density measurements were made on each clast from each sample by the method of Houghton and Wilson (1989). The distribution of densities per sample was binned and plotted on histograms, and individual clasts were chosen from the bins representing the modal values as well as the highs and lows for thin sectioning.

Quantitative data used to characterize processes that create signature textures such as vesicle size distributions (VSDs) and vesicle shape were collected from images captured from these thin sections. Vesicle size distributions (VSDs) are a tool to constrain the relative timing of bubble nucleation, growth, coalescence, and potentially collapse in explosive eruptions and to understand how the style, timing, and extent of magma degassing influence ensuing eruptive behavior (Mangan et al. 1993; Cashman and Mangan 1994; Mangan and Cashman 1996). Vesicle shape also preserves information

about the state of stress in the magma at the time of quenching (Marti et al. 1999; Polacci et al. 2001).

Scanning electron microscope (SEM) and scanned images were captured using the thin sections made from each of the subset of clasts from chosen samples. Heterogeneity in vesicle size in a single thin-section necessitated that images at four different magnifications were captured and analyzed. The data were then combined in order to completely characterize vesicle size distribution. For Novarupta dacites, the best combination of magnifications is 4.5x, 25x, 100x, and either 250x or 500x. The lowest magnification (4.5x) images were collected by scanning the thin sections on a Hewlett-Packard flatbed scanner at 1200 dpi resolution. These were captured in order to document the largest vesicles (2-3 mm) in each 16-32 mm clast. Backscatter electron (BSE) images with a resolution of 254 dpi were collected using a JEOL-5900LV SEM operating at a 20 kV accelerating voltage and 1 nA beam current for the higher magnifications. The strategy used for acquisition of images of higher magnification involved nested sets of images. A minimum of two 25x images were taken, carefully chosen to represent the range of vesicle textures in the entire section. Areas with large phenocrysts or high crystal number densities were therefore avoided. Within each of the 25x images, two 100x images were collected, and within each of the 100x, two images of either 250x or 500x were captured. Thus, a minimum of eight 250x or 500x images, four 100x images, and two 25x images were captured per clast. The decision between collecting images at 250x or 500x was based on the size and number density of the

smallest-sized vesicles. Lower limits for the size of measured vesicles were 8  $\mu\text{m}$  and 4  $\mu\text{m}$  for 250x and 500x images, respectively, using a 20 pixel cutoff value.

Images were processed and analyzed using Adobe Photoshop and Scion Image software. The images were captured in grayscale and then transformed into binary images in which vesicles are black and glass is white. Manual editing of the images was required to rebuild vesicle walls broken during thin sample preparation and to remove flaws such as air bubbles or grinding compound. In addition, thin bubble walls were often lost during image acquisition or during the conversion from grayscale to binary and had to be redrawn. The final binary images were analyzed with Scion Image software to obtain both the mean grayscale value and individual vesicle measurements of area and shape.

For each vesicle area measured, an equivalent diameter that equates to a circle with the same area was calculated. Based on this diameter, vesicle data were binned, and areal number densities ( $N_A$ ) were calculated. Conversion from two-dimensional to three-dimensional volumetric number densities ( $N_V$ ) was performed based on the method of Sahagian and Proussevitch (1998). The method relies on the intersection probabilities for spheres to determine conversion coefficients ( $\alpha$ ) for each bin-size.  $N_V$  can then be calculated from  $N_A$  using ( $\alpha$ ) and a mean projected height ( $\bar{H}$ ), i.e., typical diameter for vesicles in that bin-size. The volume fraction for each bin-size was calculated using  $N_V$  and the volume of a sphere with a diameter equal to  $\bar{H}$ . Cumulative number densities were also determined for each clast. Detailed procedural notes can be found on the

spreadsheets used to combine the nested images and convert from areas to volumes; these spreadsheets are collectively housed in the appendix.

In addition to collecting samples for textural analysis, the majority of the 2003 field season consisted of characterizing and sampling the block and lapilli apron of the Episode IV deposit. Layer H is a fine ash that fell after all Plinian activity ceased and is still preserved in some regions of the valley. On top of Layer H, dispersed predominantly to the west and south of the present-day dome, are blocks ranging from cm to m in diameter of pumiceous dacite, dense dacite, breccia, and flow-banded dacite. In Chapter 3, I describe how this deposit can be interpreted as the result of disruption of an early, ephemeral dome or plug by Vulcanian explosions prior to Episode V. At ~700 sites, three dimensions of the largest blocks were measured, GPS points were taken, samples were collected, and descriptions were made of individual blocks. The data was collected along traverses at sites approximately every 20 m. While some blocks remained intact after impact, others broke into up to 20+ pieces. In some cases, the pieces clearly fit together, like pieces of a puzzle, thus the original block size could be reconstructed. Dimensions were then measured on both the reconstructed block as well as the largest individual piece. For componentry purposes, every major block within two rectangular regions of areas 2400 m<sup>2</sup> and 3600 m<sup>2</sup> was recorded. The block bed data was then entered into a GIS. ArcGIS by ESRI was used to create maps showing block distribution. GPS locations for each block and aerial photos were co-registered to 15-minute Alaska DEM data and Arc vector files of topographic maps for USGS Mt. Katmai quadrangles. Dispersal and degassing data were combined by Sarah Fagents in a model

to parameterize the Vulcanian explosions that created the block bed, e.g., required amount of gas, ballistic velocities, etc.

#### **1.3.4 Contributions**

Samples used in the study were collected by Bruce Houghton and Nancy Adams. Data collection and processing, including vesicularity calculations, image collections and restorations, vesicle size and volume distributions determinations, and GIS-database set-up were performed by Nancy Adams. Bruce Houghton greatly assisted with the interpretation and broader implications of the data. Modeling of the Vulcanian explosions that disrupted the Episode IV dome in Chapter 3 was performed by Sarah Fagents using the Fagents and Wilson (1993) model. Wes Hildreth made several useful insights in reviews of the draft manuscripts for Chapters 2 and 3.

## CHAPTER 2

### **Abrupt transitions during sustained explosive eruptions: examples from the 1912 eruption of Novarupta, Alaska**

#### **2.1 Abstract**

Plinian/ignimbrite activity stopped briefly and abruptly 16 and 45 hours after commencement of the 1912 Novarupta eruption defining three episodes of explosive volcanism before finally giving way after 60 hours to effusion of lava domes. We focus here on the processes leading to the termination of the second and third of these three episodes. Early erupted pumice from both episodes show a very similar range in bulk vesicularity, but the modal values markedly decrease and the vesicularity range widens toward the end of Episode III. Clasts erupted at the end of each episode represent textural extremes; at the end of Episode II clasts have very thin glass walls and a predominance of large bubbles whereas at the end of Episode III clasts have thick interstices and more small bubbles. Quantitatively, all clasts have very similar vesicle size distributions which show a division in the bubble population at 30  $\mu\text{m}$  vesicle diameter and cumulative number densities ranging from  $10^7$ - $10^9$   $\text{cm}^{-3}$ . Patterns seen in histograms of volume fraction and the trends in the vesicle size data can be explained by coalescence signatures superimposed on an interval of prolonged nucleation and free growth of bubbles. Compared to experimental data for bubble growth in silicic melts, the high 1912 number densities suggest homogeneous nucleation was a significant if not dominant mechanism of bubble nucleation in the dacitic magma.

The most distinct clast populations occurred toward the end of Plinian activity preceding effusive dome growth. Distributions skewed toward small sizes, thick walls, and teardrop vesicle shapes are indicative of bubble wall collapse marking maturation of the melt and onset of processes of outgassing. The data suggest that the superficially similar pauses in the 1912 eruption which marked the ends of episodes II and III had very different causes. Through Episode III, the trend in vesicle size data reflects a progressive shift in the degassing process from rapid magma ascent and coupled gas exsolution to slower ascent with partial open-system outgassing as a precursor to effusive dome growth. No such trend is visible in the Episode II clast assemblages; we suggest that external changes involving failure of the conduit/vent walls are more likely to have effected the break in explosive activity at 45 hours.

## **2.2 Introduction**

While the steady state behavior of sustained eruption plumes has been adequately modeled (Sparks 1986; Woods 1988; Bursik et al. 1992; Sparks et al. 1992; Koyaguchi 1994; Ernst et al. 1996; Sparks et al. 1997), sudden pauses and abrupt unidirectional shifts in eruptive regime and intensity (e.g., Self and Rampino 1981; Sigurdsson et al. 1984; Self 1992; Paladio-Melosantos et al. 1995; Cioni et al. 1999; Rosi et al. 2001) remain poorly explained. In many theoretical models of large eruptions, thresholds in mass eruption rates (MER) drive first-order shifts in regime, i.e., changes from effusive to explosive eruption (Jaupart and Allegre 1991) or from convecting to collapsing columns (Melnik 2000). In nature, transitions in eruptive style and intensity are complex,

sometimes involving pulsatory behavior (e.g., Carey et al. 1990; Rosi et al. 2001; Kokelaar 2002; Druitt et al. 2002), or simultaneous production of convecting columns and pyroclastic density currents (e.g., Wilson and Walker 1985; Fierstein and Hildreth 1992). The complexity observed in natural systems highlights the need to identify the parameters controlling eruption processes and understanding the interplay between processes.

Eruption dynamics are influenced by processes occurring in (i) the region of magma storage, (ii) the volcanic conduit, and (iii) the vent. The latter two environments are of interest in this study. In the conduit, magma ascent induces changes in melt rheology during degassing and crystallization (Cas and Wright 1987; Jaupart and Tait 1994; Cashman et al. 2000). Flow dynamics are critically related to melt rheology which will alter in response to changing concentrations of dissolved volatiles, bubbles, and microlites in the melt (Pinkerton and Stevenson 1992; Hess and Dingwell 1996; Manga et al. 1998; Rust et al. 2003). Conduit and vent geometries also have a strong influence on eruption dynamics, particularly on ascent velocity and eruption regime (Wilson et al. 1980; Bursik and Woods 1991; Jaupart and Tait 1994; Woods and Bower 1995). Steady removal of wall rock into intense but stable Plinian plumes can lead to systematic vent enlargement (Carey and Sigurdsson 1989) and column collapse (Francis 1993).

In this study we examine in detail two of three major breaks in the largest eruption of the 20<sup>th</sup> century, the 60-hour long Novarupta 1912 eruption (Fierstein and Hildreth 1992; Hildreth and Fierstein 2000). Our study focuses on changes occurring in-and-to the volcanic conduit and vent during Plinian episodes II and III. This eruption is

an excellent case study for examining conduit dynamics and evolving vent geometry during a major explosive event because the changing eruptive styles and breaks in activity are readily identifiable in its voluminous deposits. General questions concerning pauses and breaks in otherwise sustained Plinian eruptions can thus be addressed at Novarupta. Why did explosive volcanism pause at the ends of episodes I and II, and what mechanisms drove the final transition to effusive volcanism after Episode III? What was the nature of the degassing? How did processes occurring in the conduit affect the steadiness of the eruption, i.e., what were they and how could they have caused the pulses in intensity? By studying individual pyroclasts from the eruption and quantifying textures, we address such questions.

## **2.3 Background**

### **2.3.1 Eruption description**

The 1912 eruption at Novarupta, Alaska is a valuable case study because: (1) it was the most voluminous eruption of the 20<sup>th</sup> century (exceeded by only four eruptions in the last 1000 years); (2) caldera collapse occurred 10 km from vent preserving the very near-vent products of the eruption; and (3) the eruption products have a very wide compositional range (50.4-77.7% SiO<sub>2</sub>) defining a chemical stratigraphy which enables correlation of coeval products of highly varying character at widely spaced localities (Fierstein and Hildreth 1992). The 60-hour explosive phase of the eruption began 6 June and included, at its peak of intensity, simultaneous deposition of Plinian fall deposits and voluminous ignimbrites (Hildreth 1983; Hildreth 1987; Hildreth 1991; Fierstein and

Hildreth 1992; Hildreth and Fierstein 2000). Stratigraphy and eyewitness accounts point to two short breaks in the 60 hours of Plinian activity at Novarupta on the morning of 7 June and the evening of 8 June, defining three episodes of explosive eruption (Fig. 2.1). Volumetrically, most of the ignimbrite generation occurred during Episode I; deposition during episodes II-III was dominantly Plinian fall. Explosive volcanism was followed by two episodes of dome/plug emplacement of first dacitic (Episode IV) then rhyolitic (Episode V) composition. Three concentric, nested features define the Novarupta vent region: the crater, the ejecta ring, and the dome (Fig. 2.2).

### **2.3.2 Episode II/III stratigraphy**

The medial-distal Plinian fall deposits are divided into 8 layers (A through H) by Curtis (1968) formed during three Plinian episodes (I through III) separated by breaks of a few hours (Hildreth 1983) (Fig. 2.1). Episodes II and III, the focus of this study, deposited Plinian falls C and D, and F and G respectively, with only minor intraplinian pyroclastic flows and surges. The ejecta has a predominantly dacitic composition (Fierstein and Hildreth 1992). These medial-distal falls are classical Plinian deposits in the sense of both Walker (1973) and Pyle (1989) with inferred column heights of 25 (CD) and 23 (FG) km [method of Carey and Sparks (1986)] and estimated peak mass eruption rates (Fierstein and Hildreth 1992) of  $0.6$  and  $0.4 \times 10^8$  kg/s [after Carey and Sparks (1986), Sparks (1986)] or  $1-2$  and  $0.2-0.3 \times 10^8$  kg/s [after Wilson and Walker (1987)]. They were followed by deposition of fine ash layers E and H, respectively; broadly synchronous with Layer E in the proximal region is a blast-like pyroclastic density current marking the initiation of Episode III (Houghton et al. 2004b). A more complex

proximal stratigraphy was established by Houghton et al. (2004b) who show that the proximal succession for episodes II and III includes alternations and mixtures of both locally and regionally dispersed fall ejecta as well as thin deposits of pyroclastic density currents (PDCs) with no regional analogs.

### **2.3.3 Melt properties and storage**

Phenocryst content in the Novarupta high-silica rhyolite (77-78 wt% SiO<sub>2</sub>) is 1-3 wt%, whereas the dacites (63-68 wt% SiO<sub>2</sub>) and andesites (58-63 wt% SiO<sub>2</sub>) contain 30-50 wt% phenocrysts (Hildreth and Fierstein 2000). Phenocrysts in the rhyolites include plagioclase, quartz, pyroxene, and magnetite; with the exception of quartz, a similar assemblage is present in the intermediate magmas. Based on FTIR spectroscopic analysis of melt inclusions trapped in quartz phenocrysts in Episode I rhyolitic ejecta, dissolved H<sub>2</sub>O concentrations range from 3.5-4.7 wt% (Lowenstern 1993). Dissolved H<sub>2</sub>O ranges between 2.2-3.1 wt% in melt inclusions from plagioclase phenocrysts from Episode II dacitic pumice, and CO<sub>2</sub> in both rhyolites and dacites falls below the minimum detection limit of 50 ppm (Lowenstern 1993).

While debate continues concerning the storage region for the 1912 rhyolite (Hammer et al. 2002), all authors agree the dacite erupted in episodes II and III was stored in a shallow reservoir beneath Mount Katmai 10 km east of Novarupta (Hildreth 1987; Fierstein and Hildreth 1992; Hildreth and Fierstein 2000; Coombs and Gardner 2001; Hammer et al. 2002). Using water-saturated experiments on pumice, Coombs and Gardner (2001) calculated that this rhyolitic magma chamber was located at a depth of 1.8-4.4 km. Hammer et al. (2002) determined for a continuum of intermediate magmas

(dacite to andesite) a storage depth of 2-4 km, if they were undersaturated with respect to H<sub>2</sub>O either because a vapor phase did not exist or because CO<sub>2</sub> was a significant component. Equilibration pressures for the H<sub>2</sub>O-undersaturated magmas are 50-75 MPa. If the magmas were H<sub>2</sub>O saturated, the depths range from 3-4 km for andesites and 1-2 km for dacites with corresponding pressures of 75-100 MPa and 25-50 MPa, respectively (Hammer et al. 2002).

## **2.4 Techniques**

### **2.4.1 Sample collection**

Suites of samples of dacitic pumices were assembled from two key sections within 4 km of the Novarupta vent (sites 94-1 and 94-Z, Fig. 2.2). Each sample contains 50-100 clasts of 16-32 mm diameter. The vertical sampling intervals were small, typically 2-3 clasts high, and chosen as typical of each eruption layer and spanning the transitions between episodes and the shifts in style/intensity. Samples from these two sites were used to represent the fall layers from episodes II and III, namely layers C, D, F, and G (Fig. 2.3). At site 94-1, 4 km northeast of the Novarupta vent, the fall sequence of layers C through G is well exposed although G is cut by an erosion surface. However, 800 m south of the vent a more complete G is exposed in a canyon at site 94-Z. The stratigraphy at 94-Z and other proximal sites is more complex than site 94-1 and includes the locally dispersed fall and PDC deposits described by Houghton et al. (2004b).

Twenty-two samples totaling ~1400 pumice clasts were collected from the episode II and III deposits exposed at site 94-1: five from Layer C, three from D, and

fourteen from F+G. Twenty-three samples were collected from the 94-Z plinian deposits: fourteen from F and nine from G. In addition, five samples were collected from the deposits of intraplinian PDCs at 94-Z (Fig. 2.3).

#### **2.4.2 Density/vesicularity**

Density measurements were made on each clast from the samples collected at sites 94-1 and 94-Z by the method of Houghton and Wilson (1989). Bulk vesicularity for each clast was then determined using a dense rock equivalent (DRE) density of 2450 kg/m (Spera 2000).

The patterns of clast density/vesicularity across the stratigraphy were used to select a small number of samples from sites 94-1 and 94-Z for measurements of vesicle size (Fig. 2.3 and Table 2.1). Samples 13, 9, 8, and 2 were chosen from site 94-1 to represent layers C, D, F, and G, respectively. Samples 2, 14, and 22 were used to analyze clasts from the complex proximal deposits coeval with layers F and G at site 94-Z.

#### **2.4.3 Image analysis**

Textures of pyroclasts, specifically vesicle size distribution, vesicle shape, and abundance of microlites, can be quantified from image analysis and used to study conduit processes (Cashman and Mangan 1994; Mangan and Cashman 1996; Hammer et al. 1999). Scanning electron microscope (SEM) and scanned images from polished thin sections were used to quantify textural features in pumices from individual stratigraphic levels and to measure changes in vesicularity and crystallinity during the major shifts in eruptive intensity at Novarupta. Vesicle size distributions (VSDs) are a tool to constrain the relative timing of bubble nucleation, growth, coalescence, and potentially collapse in

explosive eruptions and to understand how the style, timing, and extent of magma degassing influences ensuing eruptive behavior (Mangan et al. 1993; Cashman and Mangan 1994; Polacci et al. 2003). Vesicle shape also preserves information about the state of stress in the magma at the time of quenching (Marti et al. 1999). Theory developed for the interpretation of crystal size distributions (Cashman and Marsh 1988; Marsh 1988; Cashman 1992) has also been applied to vesicle populations (Toramaru 1990; Cashman and Mangan 1994; Klug and Cashman 1994; Mangan and Cashman 1996). Kinetic information about bubble nucleation and growth, which may depend on eruptive parameters such as ascent velocity or radial position in the conduit and on pre-eruptive parameters such as melt temperature and volatile content, can be determined from the VSDs if, as at Novarupta, independent assessments of the appropriate time scales are available. For many samples, VSDs do not follow linear trends describing steady state nucleation and growth but instead indicate more complex histories of magma ascent and degassing.

A subset of 3-6 pumice clasts from each of the chosen samples was selected for image collection and analysis in thin section. Selection was based on the density data and qualitative observations of all the clasts in a sample. Heterogeneity in vesicle size and shape in a single thin-section necessitated that images at four different magnifications were captured and analyzed. The data were then combined in order to completely characterize vesicle size distribution. For Novarupta dacites, the best combination of magnifications is 4.5x, 25x, 100x, and either 250x or 500x. The lowest magnification (4.5x) images were collected by scanning the thin sections on a Hewlett-Packard flatbed

scanner at 1200 dpi resolution. These were captured in order to include the largest vesicles (2-3 mm) in each 16-32 mm clast. Backscatter electron (BSE) images with a resolution of 254 dpi were collected using a JEOL-5900LV SEM operating at a 20 kV accelerating voltage and 1 nA beam current for the higher magnifications. The strategy used for acquisition of images of higher magnification involved nested sets of images. A minimum of two 25x images were taken, carefully chosen to represent the range of vesicle textures in the entire section. Areas with large phenocrysts or high crystal number densities were therefore avoided. Within each of the 25x images, two 100x images were collected, and within each of the 100x, two images of either 250x or 500x were captured. Thus, a minimum of eight 250x or 500x images, four 100x images, and two 25x images were captured per clast. The decision between collecting images at 250x or 500x was based on the size and number density of the smallest-sized vesicles. Lower limits for the size of measured vesicles were 8  $\mu\text{m}$  and 4  $\mu\text{m}$  for 250x and 500x images, respectively, using a 20 pixel cutoff value.

Images were processed and analyzed using Adobe Photoshop and Scion Image software. The images were captured in grayscale and then transformed into binary images in which vesicles are black and glass is white. Manual editing of the images was required to rebuild vesicle walls broken during thin sample preparation and to remove flaws such as air bubbles or grinding compound. In addition, thin bubble walls were often lost during image acquisition or during the conversion from grayscale to binary and had to be redrawn. The final binary images were analyzed with Scion Image software to

obtain both the mean grayscale value and individual vesicle measurements of area and shape.

For each vesicle area measured, an equivalent diameter for a circle with the same area was calculated. Based on this diameter, vesicles were binned, and areal number densities ( $N_A$ ) were calculated for each bin and adjusted for phenocrysts. Specifically,  $N_A$  refers to the number of cross-sections within a certain size interval per total image area at a particular magnification corrected for vesicles cut by the edge of the image. Conversion from two-dimensional to three-dimensional number densities ( $N_V$ ), i.e., number of vesicles within a certain size interval per unit volume, was performed based on the method of Sahagian and Proussevitch (1998). The method relies on the intersection probabilities for spheres to determine conversion coefficients ( $\alpha$ ) for each bin-size.  $N_V$  can then be calculated from  $N_A$  using ( $\alpha$ ) and a mean projected height ( $\bar{H}$ ), i.e., typical diameter for vesicles in that bin-size. The result corrects for large vesicles cut at less than their maximum diameter and incorrectly counted in smaller size classes. The volume fraction for each bin-size was calculated using  $N_V$  and the volume of a sphere with a diameter equal to  $\bar{H}$  and adjusted so that the cumulative volume fraction matched the measured vesicularity. For the Novarupta data, the summed volume fraction is typically ~10% higher than the measured vesicularity and principally reflects uncertainty introduced by the assumption of a spherical geometry for the bubbles. Given the number of geometric bins (24-28) required to quantify Novarupta vesicle sizes, an expanded scale of  $\alpha$ -values (K.V. Cashman pers. comm.) was used. The cumulative number density ( $N_{V \text{ total}}$ ) referenced to the matrix of the clast, i.e., total clast volume less the phenocrysts, and

determined by summing the number density for each bin size ( $N_V$ ) records the rate and timing of nucleation of vesicles during the rise of a parcel of magma. Cumulative number densities referenced to the melt volume ( $N_{V \text{ total}}^m$ ) have also been determined for each clast to allow for the misleading effect of the vesicle population itself on the number density (Klug et al. 2002). Detailed procedural notes can be found on the spreadsheets used to combine the nested images and convert from areas to volumes; these spreadsheets are collectively housed in the appendix.

## **2.5 Results**

### **2.5.1 Density**

Samples from site 94-1 show most clearly the pattern of changing clast density with time through episodes II and III. Episode II data are remarkably consistent; although densities range from 350-1030 kg/m<sup>3</sup> for the 8 samples (Fig. 2.4), the mean density of samples only increases slightly from the start to the finish of the episode, rising from 630 to 660 kg/m<sup>3</sup>. In contrast, mean density increases gradually but significantly with stratigraphic height in the 14 samples spanning Episode III; the sample representing the close of the episode has a mean density of 900 kg/m<sup>3</sup>.

Pumices collected from Episode III fall deposits at site 94-Z have densities ranging from 410-1570 kg/m<sup>3</sup> with mean values between 740-880 kg/m<sup>3</sup>. When comparing the density distributions from 94-1 and 94-Z samples, the proximal pumices consistently have slightly higher modal densities than those at more distal site 94-1 (Fig.

2.5), reflecting a very mild role of density fractionation in the Novarupta plumes with distance from source (cf., Houghton and Wilson 1989).

Based on their densities, clasts from within seven samples representing the episodes II and III eruptive sequence were selected for image analysis. One clast with modal density for each sample was thin sectioned and measured. From site 94-1, clasts from samples 2, 8, 9, and 13 (layers G through C, Fig. 2.5) were used. The measured density for each of these clasts was 850, 680, 640 and 650 kg/m<sup>3</sup>, respectively.

Characterizing the close of plinian activity more proximally, three clasts from samples 22, 14, and 2 from site 94-Z (layers G and F, Fig. 2.5) were also examined. The measured densities for the three modal clasts at site 94-Z ranged from 810-890 kg/m<sup>3</sup>. In both sections (94-1 and 94-Z), the modal densities of Layer G show a progressive shift away from those of layers C, D, and F (Figs. 2.4, 2.5). To better determine the processes that might be causing the increase, additional clasts were selected representing high and low density extremes in two samples: 94-1-2 (high density 1020 kg/m<sup>3</sup>), 94-Z-22 (high density 1180 kg/m<sup>3</sup> and low density 610 kg/m<sup>3</sup>).

### **2.5.2 Qualitative observations of vesicles**

Diverse textural features characterize the pumices in thin section (Fig. 2.6). Some clasts show uniform distribution of a range of vesicle sizes throughout the slide (Fig. 2.6a). However, other ubiquitously heterogeneous clasts show distinct regions where small bubbles (diameters  $\leq 5-25 \mu\text{m}$ ) predominate and are surrounded by a matrix of mid-to-coarse vesicles ( $75-100 \mu\text{m}$  and  $\geq 175 \mu\text{m}$  diameters, respectively) (Fig. 2.6b). Independent of the degree of heterogeneity, a marked predominance of intermediate-to-

coarse bubbles is conspicuous within some slides (Fig. 2.6c). Bubble deformation is present in some pumices and typically occurs as bands of elongated vesicles crossing larger regions of more equant bubbles (Fig. 2.6a-b). The bands tend to range in width from  $\sim 50 \mu\text{m}$ - $500 \mu\text{m}$ , suggesting the presence of localized shear zones on a range of scales.

Many stages of bubble coalescence are evident in the Novarupta pumices (Fig. 2.7). The expansion of smaller bubbles into larger bubbles can be seen throughout the eruptive sequence [‘donut-like’ features of Klug et al. (2002)]. As in Mazama pumices (Klug et al. 2002), interaction between equally-sized bubbles often results in very thin planar melt films ( $\sim 1 \mu\text{m}$ ) inferred to be caused by approximately equal pressures acting on the film from inside each bubble. Wrinkling and incomplete retraction of bubble walls, signs of wall failure as two bubbles coalesce, occur most frequently when medium-to-coarse bubbles interact. Coalescence generally does not occur until melt films thin to  $\leq 3 \mu\text{m}$  in thickness. If wrinkling occurs, the thickness of the bubble walls appears to be in the range of 1-3  $\mu\text{m}$ . These parameters on film thicknesses coincide with measurements on the dacites and rhyolites studied by Klug and Cashman (1996). They observed wrinkling in walls  $< 5 \mu\text{m}$  thick and rupture at  $< 1 \mu\text{m}$  thickness. Based on these observations and a comparison between the largest bubbles that can coalesce via film thinning for critical thicknesses of 100, 10, and 0.1  $\mu\text{m}$  (Fig. 7 in Klug and Cashman 1996), they suggest the best estimate for critical wall thickness for dacitic and rhyolitic magma is 1  $\mu\text{m}$ .

Qualitative comparisons among the modal clasts from different stratigraphic levels promote some understanding of changes with time in the processes and conditions in the conduit during the eruption. Despite some bands of elongated vesicles, the distribution of vesicles of all sizes in the modal clast from Layer C (Figs. 2.8a, b) is relatively uniform and the vesicle walls appear moderately thin (typically 7-15  $\mu\text{m}$ ). Likewise, the modal pumice from Layer D (Fig. 2.8c) has a very uniform texture, but the vesicles walls are the thinnest of all the examined clasts (typically only 1  $\mu\text{m}$  thick and the average being  $\sim 7$   $\mu\text{m}$ ) and the images are dominated by coarse, coalesced vesicles. Pockets of elongated vesicles between heterogeneous clusters of fine and intermediate-coarse bubbles (Fig. 2.8d) describe pumices from Layer F. Thicker glass walls (typically  $\sim 20$   $\mu\text{m}$ ) and a higher abundance of small vesicles than for the clasts from layers C-F characterize Layer G modal clasts (Fig. 2.9b); also, bubble elongation occurs in regions, but the regions themselves are not narrow bands as in other clasts. High and low density clasts were also photographed for Layer G. The low density clast (Fig. 2.9c) has some 1-2  $\mu\text{m}$  thick walls but is mostly characterized by intermediate-to-thick interstices (10-25  $\mu\text{m}$  wide) while the modal (Fig. 2.9b) and the high density pumices (Fig. 2.9a) are completely dominated by intermediate (10-15  $\mu\text{m}$ ) to thick (15-25  $\mu\text{m}$ ) bubble walls. The principal variability in Layer G pumices appears to be in the bubble size distribution; low density clasts have an even mix of intermediate- and coarse-sized bubbles, modal density clasts have mostly intermediate-sized bubbles with a small population of coarse bubbles, and high density clasts have a few intermediate-sized bubbles among mostly smaller bubbles. In all clasts, however, complex amoeboid bubble shapes suggest an

advanced state of bubble-bubble interaction, e.g., small bubbles in the high density clast (Fig. 2.9a). Features such as wall retraction and planar walls demonstrate that coalescence affected the shapes of bubbles in G pumices. The tortured appearance of individual vesicles, as if they have been pinched, also becomes more developed with increasing density.

### **2.5.3 Quantitative vesicle size data**

#### **2.5.3.1 Vesicle size distributions**

Like crystal size distributions (CSDs) (Cashman and Marsh 1988; Marsh 1988), vesicle size distributions (VSDs) can be expressed as functions of population density. The vesicle population density  $n$  refers to the number of vesicles of each size increment per unit volume and has units of  $\text{mm}^{-4}$ ; it can be determined from the slope of the cumulative number distribution ( $dN_V/dL$ ) where  $L$  is equivalent diameter (mm). Under steady-state conditions, i.e., a balance of vesicles growing into and out of each size range (Cashman and Marsh 1988) where growth rate is independent of vesicle size, a straight line will result when  $\ln(n)$  is plotted against  $L$  (Mangan and Cashman 1996). The plots of  $\ln(n)$  vs.  $L$  for the Novarupta dacites, however, show curved trends (Fig. 2.10) which can be resolved into two segments. Vesicles  $\leq 30 \mu\text{m}$  plot as steeply-sloping straight lines and  $>30 \mu\text{m}$  as curves. The profiles are strikingly similar to other samples from Plinian eruptions of silicic magmas, e.g., Mt. Mazama (Klug et al. 2002), Vesuvius 79 AD (Gurioli et al. 2004), 1.8 ka Taupo (Houghton et al. 2003).

Several factors may be influencing the nonlinearity of the VSDs seen in natural systems. Because rates of bubble nucleation and growth are not constant for a

decompressing magma during an explosive pyroclastic eruption (Lyakhovsky et al. 1996; Blower et al. 2001b; Klug et al. 2002), the steady-state assumption implicit in CSDs does not apply a priori to all VSDs. In addition to nucleation and unrestricted growth, other processes such as bubble ripening or coalescence affect the linearity of the VSD.

Mangan and Cashman (1996) demonstrate that a polymodal bubble distribution, often a signature of coalescence, will produce a segmented VSD in which segment-slope flattens with increasing bubble size. Additional work (Gaonac'h et al. 1996a; Simakin et al. 1999; Mangan et al. 2004) has described VSDs of many different forms, including exponential and power-law relationships.

### **2.5.3.2 Vesicle volume distributions**

As an alternative to VSDs, plots of vesicle volume distributions (VVDs) can be used to interpret the processes and mechanics that produce more complex textural signatures. The distribution of volume fraction against vesicle diameter (Fig. 2.11) can reveal multiple bubble populations and a predominance of small or large vesicles. Median vesicle diameters, also useful when comparing clasts from different fall layers, can be directly determined as the fiftieth percentile on plots of cumulative vesicle volume data versus vesicle diameter size (Fig. 2.12).

For many plinian pumice clasts, VVDs are distinctly polymodal (e.g., Sparks and Brazier 1982; Whitham and Sparks 1986; Orsi et al. 1992; Klug and Cashman 1994; Klug et al. 2002). This is not the case for the 1912 eruption. Subordinate peaks at larger diameters are at best poorly developed in the Novarupta dacites (Fig. 2.11). Most samples do have, however, a tail of coarse bubbles extending up to 3 mm in equivalent

diameter. In addition to the apparent unimodality of the VVDs, the modal size of the bubble population is remarkably consistent at 80  $\mu\text{m}$ . The predominance of a particular vesicle size range, on the other hand, changes throughout the eruption sequence. Layers C and F at site 94-1, both representing sustained activity during the early stages of a Plinian episode, have similar distributions with sharp symmetrical peaks. The two samples of Layer F at site 94-Z have fewer coarse-sized bubbles than F at site 94-1 but still reveal the same general distribution. The mode for Layer D, representing the close of Episode II, is broader and skewed slightly toward coarser sizes. For Layer G (the close of Episode III and final cessation of Plinian activity), the mode for 94-Z is slightly less distinct than the mode for 94-1, but both distributions are skewed toward finer sizes.

The near-unimodal distributions apparent from the volume fraction histograms result in smooth sigmoidal curves with virtually no slope breaks between discrete size populations on plots of cumulative volume fraction versus size (Fig. 2.12). To compare clasts, layers have been grouped by the stage of Plinian activity they represent; samples from layers C and F represent early sustained activity and layers D and G were deposited towards the close of episodes II and III, respectively. Data from layers C and F show remarkably little variation; for both medial and proximal samples of Layer F, the curves are virtually coincident, especially at their intersection with the fiftieth percentile. The median vesicle size values for Layer F samples (Table 2.1) range narrowly between 58-62  $\mu\text{m}$ , and the value for Layer C does not deviate greatly from this range (75  $\mu\text{m}$ ). Clasts from layers D and G are more variable. The two modal Layer G clasts from 94-1 and 94-Z have very similar forms, not unlike the curves of layers C and F. Median values for

modal Layer G are 54 and 59  $\mu\text{m}$  again reminiscent of layers C and F; in comparison the median diameter for the Layer D pumice increases to approximately 100  $\mu\text{m}$ .

High, modal, and low density clasts from within the same sample can also be compared via cumulative volume percent plots to examine diversity among clasts erupted simultaneously (Fig. 2.13). The same pattern emerges for the proximal and medial samples from Layer G. The median value increases from  $\sim 60$   $\mu\text{m}$  to  $\sim 75$   $\mu\text{m}$  from the mode to the low density clast, respectively, and the value decreases to  $\sim 45$   $\mu\text{m}$  for the high density clasts.

### 2.5.3.3 Cumulative number densities

Power-law distributions of bubble size typically show linear trends on log-log plots when vesicle number is a function of size (Gaonac'h et al. 1996a; Gaonac'h et al. 1996b; Blower et al. 2001a; Blower et al. 2001b); this relationship holds for a wide range of vesicle sizes ( $>30$   $\mu\text{m}$  diameter) in the Novarupta data (Fig. 2.14). As  $L$  approaches the smallest vesicle size measured in the clast,  $N_{V>L}$  approaches the cumulative number density ( $N_{V \text{ total}}$ ) of the clast. When  $N_{V>L}$  is plotted against  $L$  on a log-log plot, the trends for all clasts define a best-fit line with a slope of -3.9 (Fig. 2.14). The linearity starts to collapse at  $\log L = 1.5$  (i.e., 30  $\mu\text{m}$ ), and an exponential trend better describes the bubbles  $\leq 30\mu\text{m}$ . So despite the near-unimodal volume distributions seen on plots of volume fraction versus vesicle size for all the samples (Fig. 2.11), cumulative number densities suggest two size populations of bubbles about a size of 30  $\mu\text{m}$  [the same division as seen on the  $\ln(n) - L$  plot (Fig. 2.10)]. The smallest vesicle counted during this study was  $\sim 4$   $\mu\text{m}$  in diameter, so for consistency with earlier work of Blower et al. (2002) and Klug et

al. (2002), the VSD for each sample has been extrapolated to  $L = 1 \mu\text{m}$  (i.e.,  $\log L = 0$ ). The cumulative number density ( $N_{V\text{total}}$ ) for all measured vesicles, i.e., larger than  $4 \mu\text{m}$ , ranged from  $7 \times 10^7 \text{ cm}^{-3}$  to  $5 \times 10^8 \text{ cm}^{-3}$  (Table 2.1). If we fit the trend of bubbles  $\leq 30 \mu\text{m}$  with an exponential curve and extend this to  $1 \mu\text{m}$  vesicle diameter size, extrapolated cumulative number densities vary from  $1-8 \times 10^9 \text{ cm}^{-3}$ . In highly vesicular clasts, cumulative number density ( $N_{V\text{total}}$ ) calculated based on the volume of the entire clast appears low since much of the volume is in fact comprised of vesicles. Vesicle number densities can also be calculated based on melt volume only ( $N_{V\text{total}}^{\text{m}}$ ), i.e., corrected for vesicle volume; at  $4 \mu\text{m}$ , cumulative number density values referenced to the melt volume ( $N_{V\text{total}}^{\text{m}}$ ) range from  $2.5 \times 10^8 \text{ cm}^{-3}$  to  $2 \times 10^9 \text{ cm}^{-3}$  (Table 2.1) and at  $1 \mu\text{m}$  from  $2 \times 10^9 \text{ cm}^{-3}$  to  $2 \times 10^{10} \text{ cm}^{-3}$ .

## 2.6 Interpretation

### 2.6.1 Bubble nucleation

The similarities in bubble number density and size distribution for all the Novarupta pumices are strongly suggestive of similar histories of bubble nucleation and growth for the majority of the melt erupted in 1912, at least during the early stages of ascent in the conduit. Near-unimodal VVDs (Fig. 2.11), such as those modeled by Toramaru (1989; 1990), suggest that vesiculation occurred over a short time interval at an early stage of decompression with little subsequent nucleation. In experiments on water-saturated high silica rhyolites, Gardner et al. (1999) varied decompression rates and hence levels of supersaturation ( $\Delta P$ ). These experimental runs agreed with Proussevitch

and Sahagian (1996; 1998) in that  $\Delta P$  dropped significantly when porosities reached greater than ~10 vol%. Even at the fastest decompression rates (1.0 MPa/s), only one nucleation event occurred (Gardner et al. 1999). If this were so for the Novarupta melt, and the VVDs were created by a single short-lived episode of nucleation and subsequent steady state growth, the expected modes would be narrow and shift to larger values of vesicle diameter with time as seen in experimental samples (Lyakhovsky et al. 1996; Gardner et al. 1999). The Novarupta histogram-VVDs do appear almost Poissonian, however, modes for all pumices are broad, typically 0.05-0.1 mm, and the peak values on the vesicle volume histograms for the modal density clasts do not shift significantly to larger vesicle sizes from Layer C to Layer G (Fig. 2.11). We suggest nucleation for the 1912 melt was more complex than the scenarios in the afore-mentioned models and experiments. Additional nucleation accompanying mid-stage to late-stage growth of earlier formed bubbles would account for the volume fraction distributions with broad peaks and the significant proportion of small bubbles.

In addition to the timescale over which nucleation occurred, the mechanism of nucleation provides insights into conduit conditions, e.g., rates of decompression and ascent rates. Recent experimental work (Gardner et al. 1999; Mourtada-Bonnefoi and Laporte 1999; Mangan and Sisson 2000) has built on the important study by Hurwitz and Navon (1994) involving bubble nucleation in high silica melts. These studies indicate that large supersaturations ( $\Delta P$ s) predicted by homogeneous nucleation theory are correct. In the absence of a large number of efficient nucleation sites, onset of nucleation in melt is delayed until shallow levels and degassing is a markedly disequilibrium process. In

contrast, during heterogeneous nucleation a large number of potential nucleation sites greatly reduces the supersaturations required to initiate bubble nucleation, and nucleation commences early such that during ascent gas and magma remain approximately in equilibrium. Heterogeneities in melt which serve as nucleation sites include crystals, conduit walls, etc.

Hurwitz and Navon (1994) and Navon and Lyakhavsky (1998) propose that bubble nucleation in most natural silicic systems is controlled by heterogeneities. Conversely, Mangan and Sisson (2000) suggest that crystal number densities, i.e., number of potential nucleation sites, as high as  $10^4 \text{ cm}^{-3}$  do not prevent supersaturations high enough to trigger homogeneous nucleation. Furthermore, powerful sustained eruptions are actually favored by high degrees of supersaturation, delayed onset of nucleation, and disequilibrium degassing, so homogeneous rather than heterogeneous nucleation should be the dominant mechanism of bubble formation during Plinian eruptions (Mangan and Sisson 2000; Mangan et al. 2004). They concede, however, a combination of both mechanisms probably occurs in most natural systems. The crystallinity, i.e., availability of potential nucleation sites, of the magma as it enters the base of the conduit influences the interplay of the two mechanisms and subsequently equilibrium versus disequilibrium degassing.

Vesicle number densities provide a link between natural samples and experimental data. The 1912 number densities ( $N_{V \text{ total}}$  and  $N_{V \text{ total}}^m$ ) range from  $10^7$ - $10^9 \text{ cm}^{-3}$  (Table 2.1); experimental results for silicic melts show homogeneous nucleation number densities of  $10^7$ - $10^9 \text{ cm}^{-3}$  (Mourtada-Bonnefoi and Laporte 1999; Mangan and

Sisson 2000) and of  $10^6$ - $10^8$   $\text{cm}^{-3}$  (Hurwitz and Navon 1994; Gardner et al. 1999) for heterogeneous nucleation. In the Hildreth (1983) study, no microlites are seen in the 1912 dacites, but the ejecta are characterized by 30-50% phenocrysts in the ratio plagioclase 5, clinopyroxene 1, and magnetite 1. In the course of our work, only one out of the 11 dacite pumices examined from episodes II-III had microlites, and it was characterized by ~5 % plagioclase microlites (Fig.2.9a). Thus, two possible scenarios emerge for nucleation conditions at Novarupta. 1) Absence of microlites and a general shortage of efficient nucleation sites lead to a delay in nucleation until extreme supersaturation pressures are reached. 2) Abundance of phenocrysts, despite the dominance of plagioclase (known to be an inefficient nucleation site), triggers bubble nucleation at lower supersaturation pressures.

Experimentally, homogeneous nucleation, a.k.a., scenario (1), in silicic melt is not observed in samples with <5 wt%  $\text{H}_2\text{O}$  and <600 ppm  $\text{CO}_2$  unless supersaturations are very high (> 120-130 MPa) (Mourtada-Bonnefoi and Laporte 1999; Mangan and Sisson 2000). Heterogeneous nucleation can occur with supersaturations on the order of 5 MPa (Hurwitz and Navon 1994). Given the modeled storage depths of 2-4 km for the 1912 intermediate magmas (Hammer et al. 2002), a supersaturation pressure reaching 120 MPa seems implausible. Additionally, the pre-eruptive  $\text{H}_2\text{O}$  content in the Novarupta magma is low compared to saturations in which homogeneous nucleation has been triggered experimentally unless  $\text{CO}_2$  was a more significant component than indicated from melt inclusions. Furthermore, experiments by Gardner et al. (1999) and models by Proussevitch and Sahagian (1996; 1998) indicate plausible decompression rates in silicic

explosive systems are not consistent with levels of supersaturation high enough to trigger homogeneous nucleation. We acknowledge, however, that experimental setups are restricted to specific modeling conditions; as such, their application to natural settings is limited, and neither homogeneous nor heterogeneous conditions can definitively be dismissed. So while a comparison between conditions at Novarupta, i.e., volatile content and decompression rates, and experimentally determined parameters contradicts the occurrence of homogeneous nucleation, the high number densities and general explosivity of the 1912 eruption suggest high nucleation rates and hence favor homogeneous nucleation (Mangan et al. 2004). We suggest at Novarupta extreme supersaturations were not reached throughout the melt, and heterogeneous and homogeneous nucleation probably operated in combination. This amalgamation was caused by variations in the melt and within its ascent history.

### **2.6.2 Bubble coalescence**

Significant bubble coalescence strongly influences vesicle size and volume distributions. It has two principal effects on the bubble population: 1) the large bubble populations are enhanced at the expense of smaller sizes often generating a bimodal size distribution (Orsi et al. 1992; Cashman and Mangan 1994), and 2) the shapes of the bubbles become more complex. Gaonac'h et al. (1996a) proposed that growth involving cascading coalescence of bubble populations in highly viscous magma produces power law size distributions. While Blower et al. (2001a; 2002) simulated similar distributions through continuous nucleation, the exponent associated with coalescence distributions was distinguishably higher ( $\sim 4$ ). Given that the power-law relationship for larger bubbles

in the Novarupta pumices is described by an exponent of 3.9 (Fig. 2.14), we infer coalescence strongly influenced vesicle growth for bubbles  $>30\ \mu\text{m}$ . Furthermore, Mangan and Cashman (1996) suggest bubble coalescence produces a curve in which slope flattens with increasing bubble size on a plot of  $\ln(n)$  vs. diameter. Curves fitting the Novarupta data for bubbles  $>30\ \mu\text{m}$  in diameter on Figure 2.10 are indeed characterized by an increasingly flatter slope. Coalescence is also abundantly evident in the shape of intermediate-to-coarse bubbles in the images (Fig. 2.7); shapes are complex and strongly deviate from spherical. Toramaru (1988) and Proussevitch et al. (1993) considered critical film thicknesses and thinning rates of films while examining bubble growth and foam stability. During early stages of foam development bubbles nucleate and grow by diffusion and decompression in an unrestricted fashion defining an exponential size distribution. At this point, coalescence is inhibited by the thickness of the bubble walls. With continued nucleation and growth and hence increasing vesicularity and thinner walls, bubble-bubble interactions and coalescence commences. Klug and Cashman (1996) suggest these interactions begin at  $\sim 30\%$  vesicularity, well below the volume fraction of a true foam (74%). So coalescence probably overlapped in time with bubble nucleation and growth during the 1912 eruption. We suggest the onset of coalescence as a significant growth process is manifested in the VSD data, specifically in the division at the  $30\ \mu\text{m}$  vesicle size. For bubbles  $>30\ \mu\text{m}$  in diameter, growth by coalescence outstripped diffusion and decompression as the dominant growth mechanism.

Klug and Cashman (1994) argue for syneruptive vesiculation and syn- and posteruptive coalescence as the source of the polymodality seen in the vesicle size distributions of the Mount St. Helens pumices. Based on qualitative observations and the high fractal dimension, coalescence was clearly a significant syneruptive process for the Novarupta dacites, but no evidence has been found to suggest post-fragmentation modification of clast textures (e.g., Thomas et al. 1994; Gardner et al. 1996). The 1912 deposits contain pumices up to 50 cm in diameter, and careful field examination of rim-to-core textures shows no obvious shifts in bubble size or density from the clearly quenched exteriors into the interiors of the blocks.

### **2.6.3 Bubble collapse: maturation of texture**

Quantitatively, clasts representing different phases of activity during episodes II and III are surprisingly similar. Trends on plots of population density and cumulative number density against bubble size show undeniable coincidence (Figs. 2.10, 2.14). The most distinctive clast populations occur in Layer G and as such have been studied in greater detail because of the implications for the close of explosive volcanism. Samples from G show a sharp increase in mode and mean density compared to layers C-F (Figs. 2.4, 2.5) reflecting comparatively thicker glass interstices and a smaller bubble population. From F to G, the melt changes from thinner glass walls and a bubble size distribution dominated by intermediate sizes (Fig. 2.15a) to thicker glass walls and a bubble size distribution skewed towards small sizes (Fig. 2.15b). Also conspicuous in Layer G is the increasingly pinched appearance of vesicles; the long diameter of elliptical vesicles often terminates in a tear or V-like shape. Similar textures characterize dome-

related samples from the 1.8 ka Taupo eruption (Fig. 2.15c). We suggest the textural signatures seen in G pumices are created by the onset of bubble wall collapse. Collapse of a bubble would thicken glass interstices and inflict irregularities along the smooth, concave walls of nearby bubbles.

## **2.7 Discussion**

Changing conduit processes imprinted microtextural variations among pyroclasts erupted throughout the Plinian activity at Novarupta. The dynamics of volatile exsolution and ascent governed the shapes and sizes of bubbles in the melt. Textural signatures were created by processes including 1) bubble nucleation, 2) growth by diffusion, decompression, and coalescence, and 3) collapse. All three processes were probably occurring simultaneously, but the significance of each varied in space and time.

### **2.7.1 Diversity within samples: heterogeneity in the conduit**

If the melt represented by pumices collected at the same stratigraphic level entered the conduit at a single instant in time and followed identical paths up the conduit until fragmentation, the range in densities and textures should be narrow. The wide range of densities within the Novarupta samples for pyroclasts essentially fragmented and erupted at the same time might indicate instead that different degassing histories characterized different portions of the melt. Material that enters the conduit and ascends relatively slowly might be expected to have a more mature bubble texture than material with a shorter residence time in the conduit. Hence, the range of textures in pumices from a single stratigraphic level might represent the range of textural maturity induced by

greater or lesser residence time in the conduit. This variation in residence time can be explained by variable ascent rates across the conduit. With continued eruption through a moderate-sized conduit, shear zones develop along the sides of the conduit and bound a non-shearing plug. Ascent of this plug is described by equal velocity bounded by narrow zones of sharply decreasing velocity proximal to the conduit walls (Cas and Wright 1987; Jaupart and Tait 1994; Dobran 2001). Plug flow in the conduit would ensure that melt traveling adjacent to the conduit wall had a longer residence time than melt occupying the center of the conduit. A similar explanation for textural heterogeneities found in Pinatubo 1991 pumice is offered by Polacci et al. (2001). Variations in velocity and shear across the width of the conduit create different ascent histories in terms of rates of bubble nucleation, growth, and collapse and thus variations in textures.

Based on the wide range in densities and the qualitative observations of the Layer G modal density pumice compared to layers C-F, high and low density clasts were also analyzed. While the general characteristics described for the modal density clasts hold for all clasts, a progression of textures is evident. Low density G pumice (Fig. 2.9c) appear very similar to F pumice (Fig. 2.15a) whereas high density G pumice show the thickest glass walls of all examined clasts and the most bubbles with complex shapes. We propose two possible explanations for the range of textures seen in Layer G. 1) Modal density texture represents the least mature pumice. With continued coalescence and depletion of volatiles in the melt, dominant bubble size increases and walls thin producing low density pumice. Eventually, permeability reaches a critical level, gas escape reduces internal bubble pressure, and collapse occurs creating the high density

pumice. 2) Low density texture marks the least mature pumice. Collapse is beginning to occur in modal density pumice but has become a more significant process in the high density pumice. In either scenario, collapse occurs with continued degassing and marks an advanced state of maturation. Vesicle shape comparisons between clasts support scenario (2). With maturity, coalescence produces increasingly more complex bubble shapes. In the high magnification images in Figure 2.9, vesicles in the low density clast are less amoeboid than their analogs in the modal and high density clasts suggesting a lesser degree of maturity.

### **2.7.2 Diversity between samples: temporal changes within an episode**

While density and textural variations within an individual sample might be explained by the velocity profile across the conduit, melt vesiculation processes can be studied by comparing the modal density clasts through time, i.e., from each eruptive unit. Layer C represents sustained Plinian activity during Episode II, and D represents waning activity. Intermediate-sized bubbles dominate Layer C (Fig. 2.8a), but as Episode II continues, the size distribution becomes skewed towards larger vesicles (Layer D; Figs. 2.8c, 2.11). The coarsest bubbles and the thinnest walls of all the examined clasts characterize Layer D. Although the change in VVDs from C to D is slight (Fig. 2.11), the shift could reflect an increasing influence of bubble growth with respect to nucleation, i.e., growth by diffusion, decompression, and predominantly coalescence outstripping nucleation (Fig. 2.16). Progressive and unidirectional changes in the melt are more pronounced during Episode III. Bubble sizes are evenly spread around a peak of 80  $\mu\text{m}$  for clasts from Layer F (94-1-8-9, 94-Z-2-4, 94-Z-14-3 in Fig. 2.11). Layer G clasts (94-

1-2-16, 94-Z-22-24), representing the close of Episode III and the cessation of Plinian activity, are characterized by more abundant fine-intermediate bubble sizes and the thickest glass walls of the analyzed clasts (Figs. 2.9, 2.15b). At 94-1, 71% by volume of the vesicles in the F clast are  $\leq 0.12$  mm in diameter whereas that amount rises to 80% in the G clast (94-1-2-16). The quantitative increase in small bubbles for the G clast perhaps signifies prolonged nucleation and comparatively less growth, but we do not favor this interpretation. The largest vesicles measured for G clasts (94-1-2-16 and 94-Z-22-24) are not significantly smaller than for layers C-F (Fig. 2.11). Furthermore, bubble shapes (Figs. 2.9, 2.15b) and a power-law distribution for vesicles  $>30$   $\mu\text{m}$  (Fig. 2.14) suggest coalescence was still a dominant process during G-time. We believe the skewing towards finer vesicle sizes and the thickening of the glass walls for Layer G pumice were produced by collapse. Thus, the evolution of the melt from F to G favors bubble growth over nucleation and eventually the onset of bubble collapse (Fig. 2.16) and the advent of open-system behavior.

### **2.7.3 Pauses and breaks in the Novarupta eruption**

The ends of episodes II and III mark the start of the two most significant breaks in the 1912 eruption. In both cases Plinian volcanism ceased, but significant differences characterize the two events. The close of Episode III marked an end to sustained explosive volcanism, replaced by extrusion of partially outgassed magma and Vulcanian explosions during Episode IV. The break between episodes II and III ended with a blast-like vent-clearing pyroclastic density current [PDC 4 of Houghton et al. (2004b)] followed by the resumption of vigorous Plinian activity (Fig. 2.1). The deposits of PDC 4

show the most radial distribution of any of the PDC deposits described in Houghton et al. (2004b) and are rich in wall-rock lithic clasts. The lithic population is conspicuously rich in vitrophyre clasts derived from Episode I deposits which formed the vent walls during Episode II. PDC 4 is also rich in pink-oxidized and perlitized rhyolite clasts which we suspect but cannot prove are recycled from the Episode I deposits. Important differences in the microtextures of the dacite erupted immediately prior to the two breaks are also evident. Vesicularity does not change significantly with time through Episode II although Layer D pumices do show a higher degree of bubble coalescence with thin glass walls and a high content of large vesicles with respect to Layer C (Fig. 2.8a, c). In contrast, throughout Episode III both the mean and maximum density of pumices shift; the increase becomes progressively more marked during the accumulation of Layer G (Figs. 2.4, 2.5). Image analyses show that this shift is produced by a decrease in bubble size and an increase in the average thickness of bubble walls (Figs. 2.8d, 2.9b, 2.15a-b).

The contrasts suggest two different mechanisms operated to terminate Plinian episodes II and III. Textural evidence does not support a degassing-driven pause between episodes II and III. Instead we propose that a short-lived blockage of the conduit - perhaps following collapse of the vent walls or shallow conduit - caused this break (Fig. 2.17a). The initiation of Episode III by the blast-like PDC carrying lithologies typical of the shallow walls of the Episode II vent supports this mechanism. In contrast, the close of Episode III and the permanent shift to effusive volcanism is marked by the first appearance of bubble collapse in turn reflecting the development of permeability in the melt and the onset of partial open-system degassing (Fig. 2.17b).

## **2.8 Conclusions**

Plinian/ignimbrite activity stopped briefly and abruptly twice during the Novarupta 1912 eruption before the eruption style changed to effusive. The pause after 45 hours and the termination after 60 hours appear to have different causes. The shift to effusive volcanism at Novarupta, as for other historical high intensity eruptions, was driven by a change to open-system degassing and slow ascent of magma within the conduit and appears to be independent of any external changes to the conduit and vent. Our data show that such shifts in eruption regime, even if they occur suddenly, can be heralded by changes in the microtextures of the Plinian pumices. In contrast, no dramatic shift in magma rheology or ascent dynamics preceded the pause between episodes II and III. External change – probably minor vent wall collapse subsequently cleared by a blast-like explosion at the initiation of Episode III – instead drove the stay in activity.

## **2.9 Acknowledgements**

The authors thank Judy Fierstein and Maggie Mangan for their constructive comments about the eruption at Novarupta and the degassing of silicic magmas. Colin Wilson played a major role in the fieldwork that established a stratigraphic framework for this project. Our work was supported by NSF grant EAR-01-06700. Images were collected on the SEM belonging to HIGP (Hawaii Institute of Geophysics & Planetology).

**Table 2.1** Parameters for representative samples

Eruptive Episode	Depositional Unit	Sampling Site	Sample No. - Clast No.	Density (kg/m <sup>3</sup> )	Ves. (%)	N <sub>A total</sub> (cm <sup>-2</sup> )	N <sub>V total</sub> (cm <sup>-3</sup> )	N <sup>m</sup> <sub>V total</sub> (cm <sup>-3</sup> )	n no./cm <sup>3</sup> /cm	Size Range (μm)	Median (μm)	no. included
III	G	94-01	2-5	1020	58.3	3.8E+05	5.5E+08	2.1E+09	4.4E+12	4-1989	44	2772
		94-01	2-16	850	65.4	1.7E+05	1.1E+08	3.8E+08	4.5E+11	8-2504	59	1318
		94-Z	22-8	1180	51.7	2.3E+05	2.8E+08	6.3E+08	2.0E+12	4-1255	45	1875
		94-Z	22-24	890	63.5	3.3E+05	4.2E+08	1.2E+09	3.1E+12	4-1989	54	2733
		94-Z	22-28	610	75.2	1.2E+05	7.7E+07	2.8E+08	2.9E+11	8-1580	74	2817
III	F	94-01	8-9	680	72.2	2.8E+05	4.0E+08	1.2E+09	3.1E+12	4-3968	61	2762
		94-Z	14-3	830	66.0	2.6E+05	3.5E+08	1.3E+09	2.7E+12	4-3152	62	3824
		94-Z	2-4	810	67.0	3.6E+05	5.5E+08	2.0E+09	4.4E+12	4-1989	58	2553
II	D	94-01	9-25	640	74.0	2.1E+05	2.6E+08	9.6E+08	1.9E+12	4-3152	99	2315
II	C	94-01	13-55	650	73.4	1.6E+05	1.0E+08	4.3E+08	4.2E+11	8-3152	75	2220

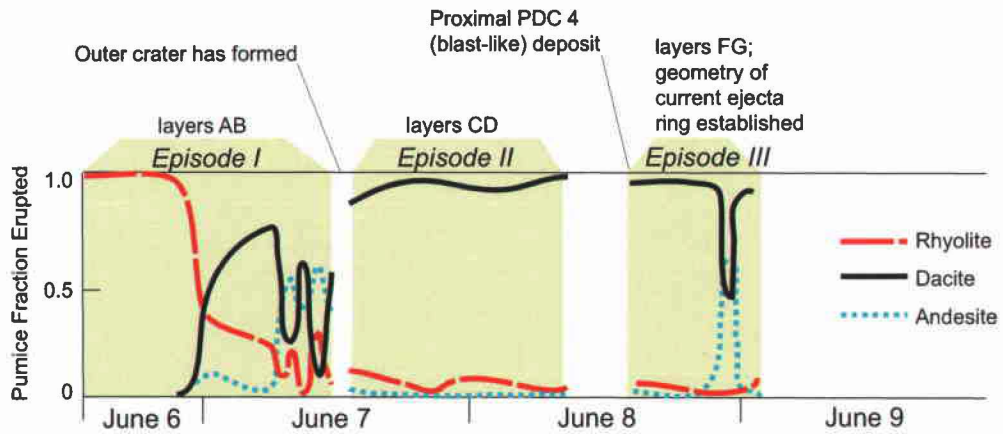
ves. - DRE value of 2450 kg/m<sup>3</sup> was used to calculate vesicularities.

N<sub>A total</sub> - areal number density of vesicles

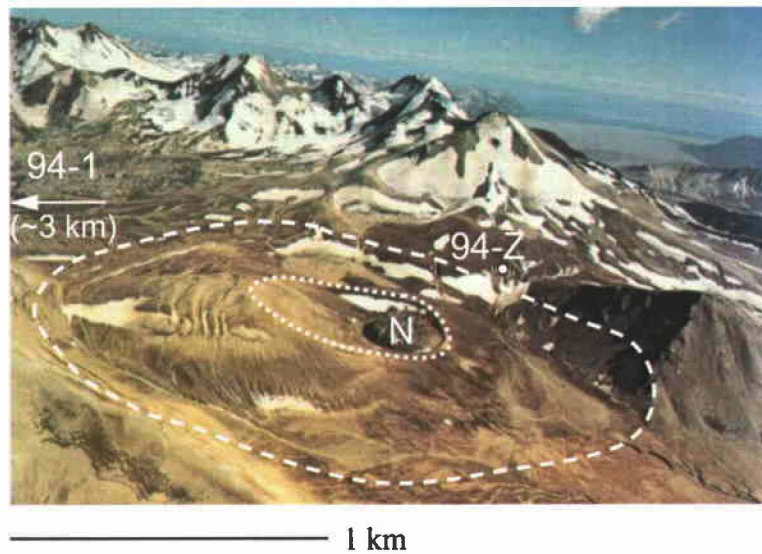
N<sub>V total</sub> - volumetric number density of vesicles; referenced to whole clast

N<sup>m</sup><sub>V total</sub> - volumetric number density of vesicles; referenced to melt only

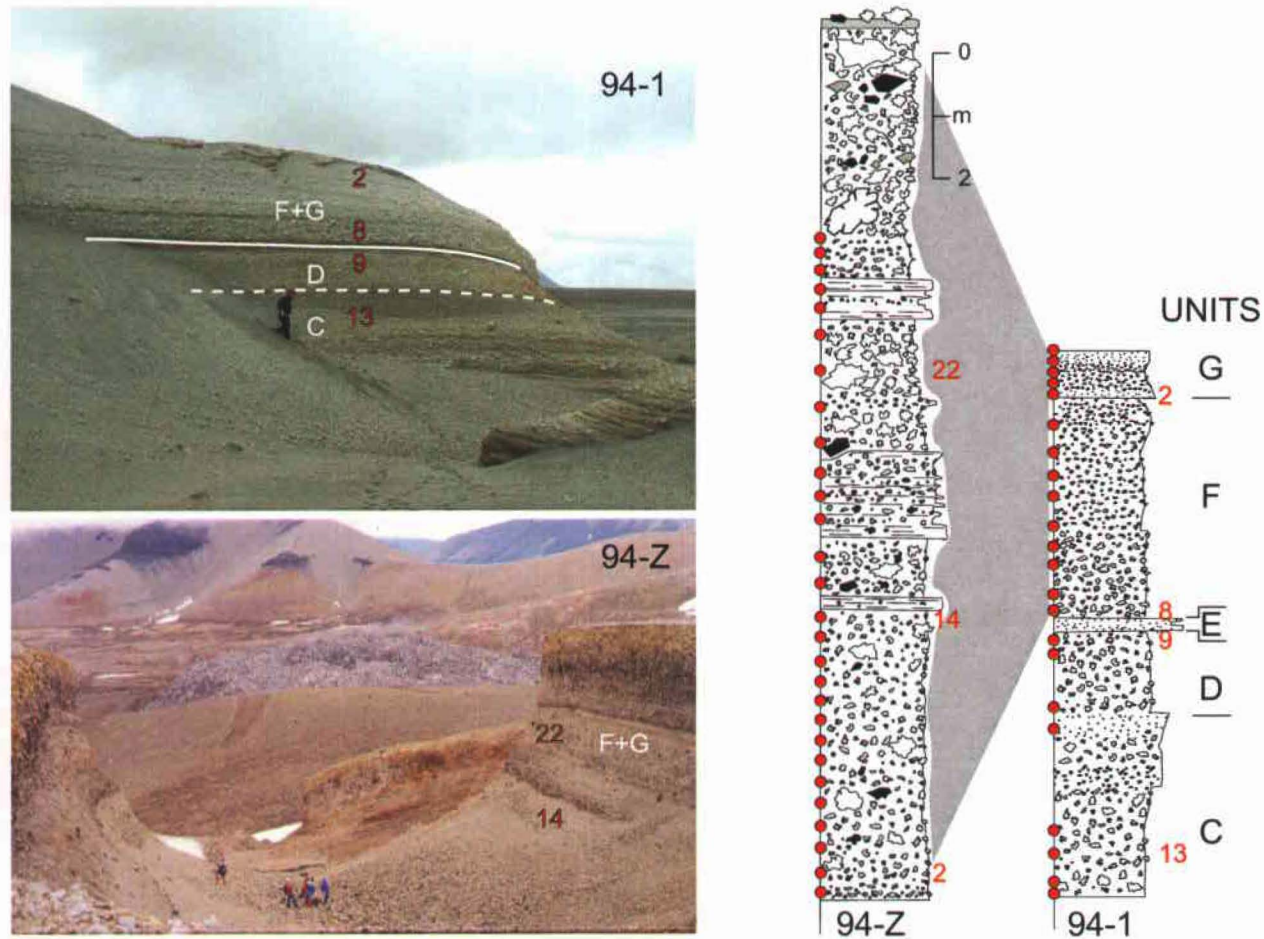
n - population number density



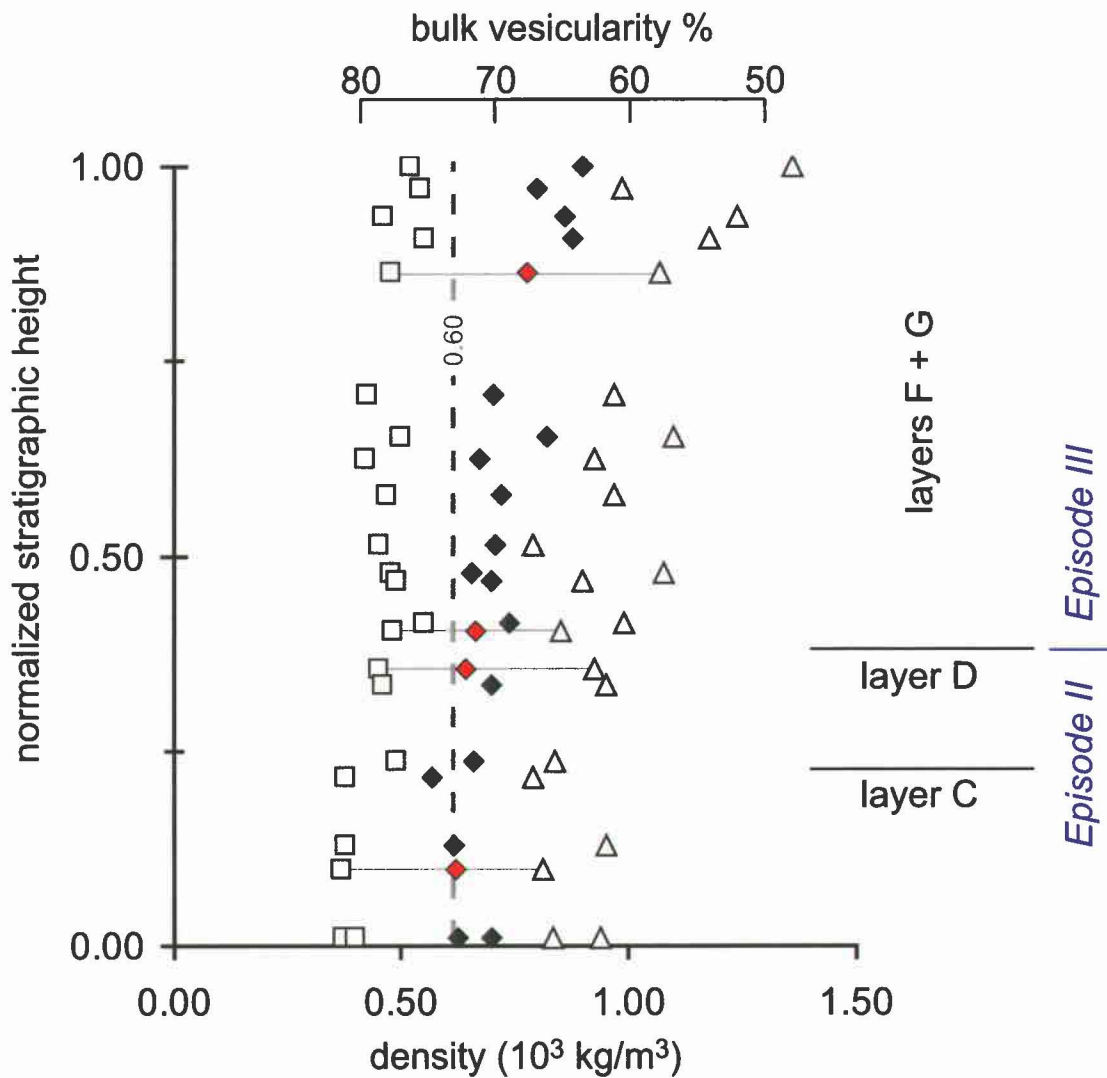
**Figure 2.1** Plot showing the relative amounts of rhyolite, dacite, and andesite erupted with time, modified after Hildreth and Fierstein (2000).



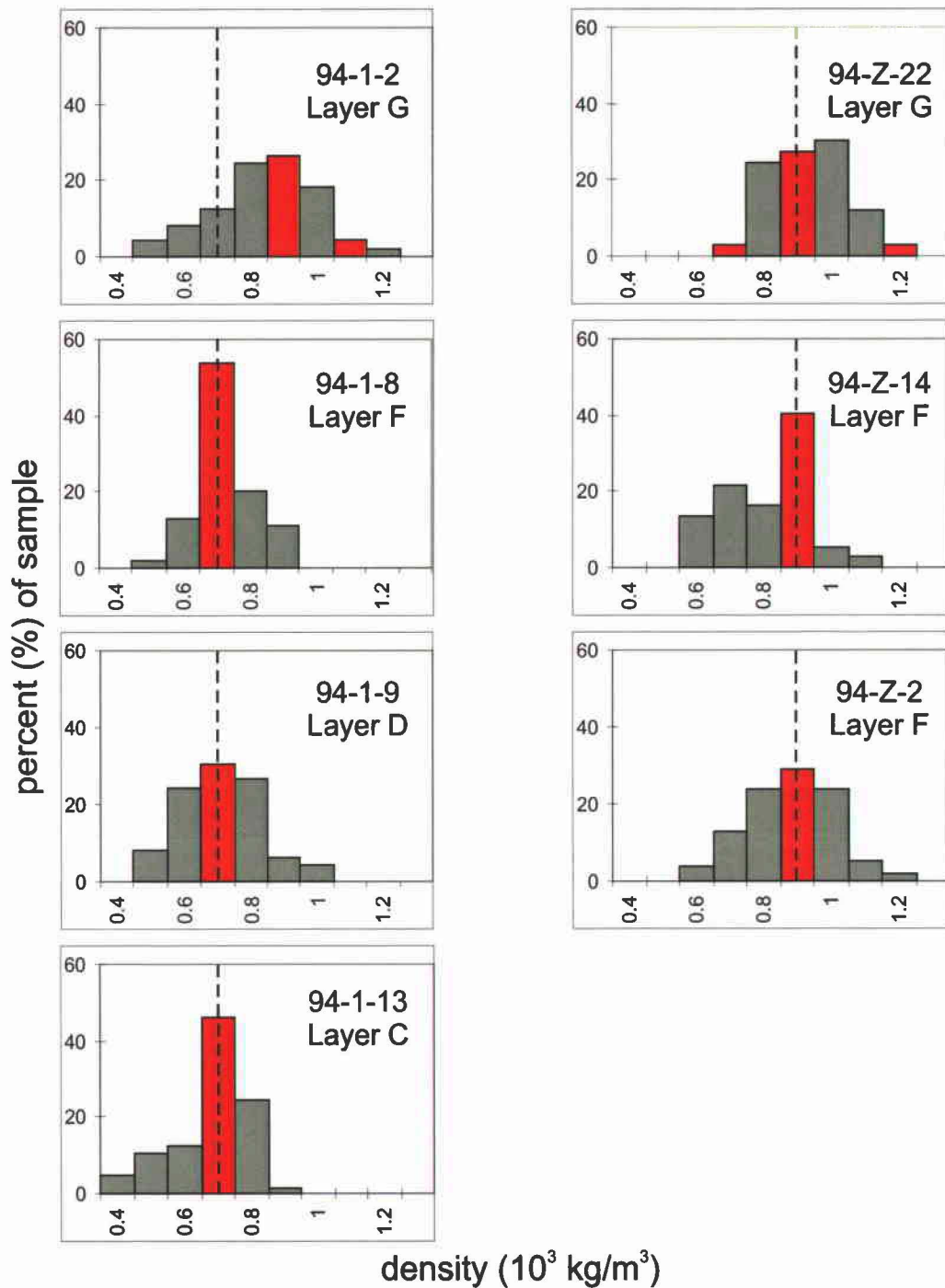
**Figure 2.2** Aerial photo in the ESE perspective of the near vent region. Three concentric, nested features include the dome (N), the ejecta ring (dotted line), and the outer crater (dashed line); sample sites 94-1 and 94-Z also labeled. Photo courtesy of Hildreth.



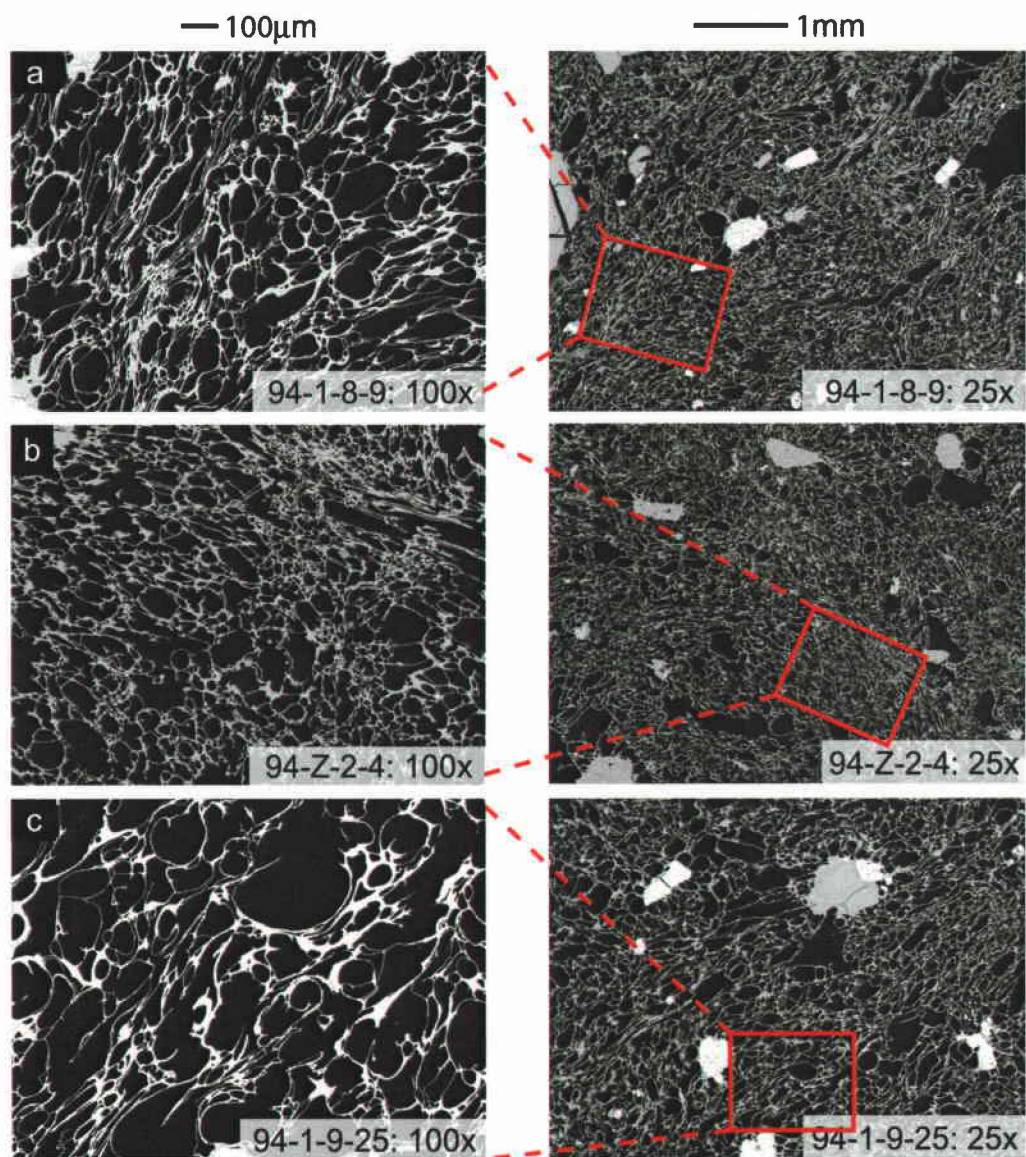
**Figure 2.3** (right) Stratigraphic logs at two sites sampled and analyzed during the current study; red-filled circles represent samples collected for density measurements (50-100 clasts) and number indicates samples from which individual clasts were selected for image analysis. 94-Z consists entirely of Episode III layers F and G. (left) Photos of the two sample sites; the Episode V dome is in the background at 94-Z.



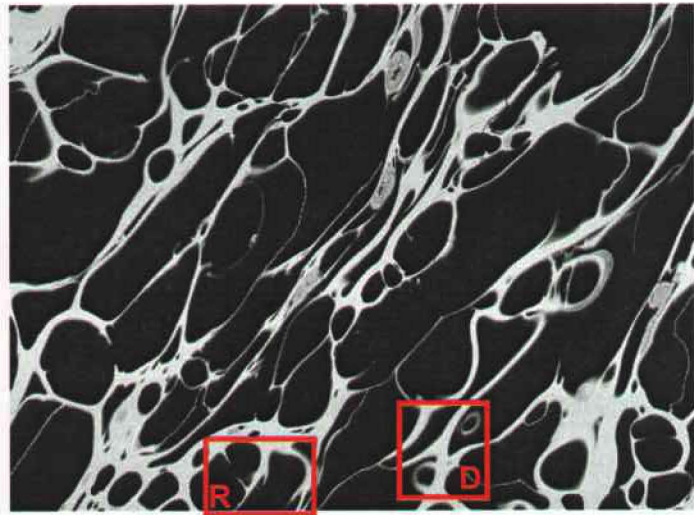
**Figure 2.4** Low, mean, and high density values for samples collected at site 94-1 against normalized stratigraphic height. Triangles represent an average of the three maximum density clasts per sample; squares an average of the three minimum density clasts. Samples used during thin section analyses are shown in red. Mean density value increased from Layer C to Layer G, i.e., as the eruption progressed.



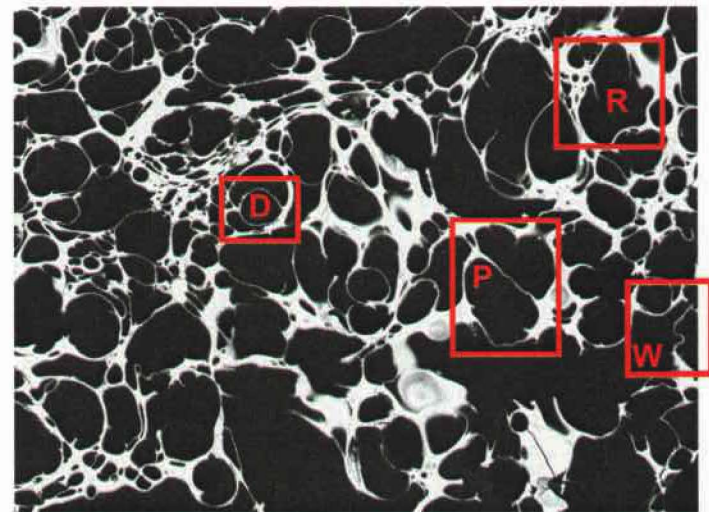
**Figure 2.5** Histograms showing density distribution for the seven samples included in this study. Red bins represent the density range an individual clast was selected from for image analysis. In sample 94-Z-22, modal density ranges between  $900\text{-}1000 \text{ kg/m}^3$ , and the mean density for the sample is  $880 \text{ kg/m}^3$ , so the clast used to represent intermediate density had a density of  $890 \text{ kg/m}^3$ . Additional high and low density clasts were selected from Layer G. Notice the higher modal values in G. The range of higher modal values for site 94-Z reflects fractionation of fall material with distance from the source.



**Figure 2.6** Back-scatter electron images (glass gray-white, vesicles black) representing range of textures present in Episode II and III clasts; rectangular region in righthand images shown at higher magnification in lefthand image. a) range of vesicle sizes evenly distributed b) regions of smaller vesicles surrounded by domains of intermediate-coarse vesicles c) image dominated by coarser bubbles. In a and b, bands of stretched vesicles cut through regions of more regularly shaped vesicles.



94-1-9-25

100 $\mu$ m

94-Z-2-4

100 $\mu$ m

**Figure 2.7** High magnification images with coalescence features (donuts-D, wall rupture-R, wrinkling-W, planar walls-P) located within drawn boxes.

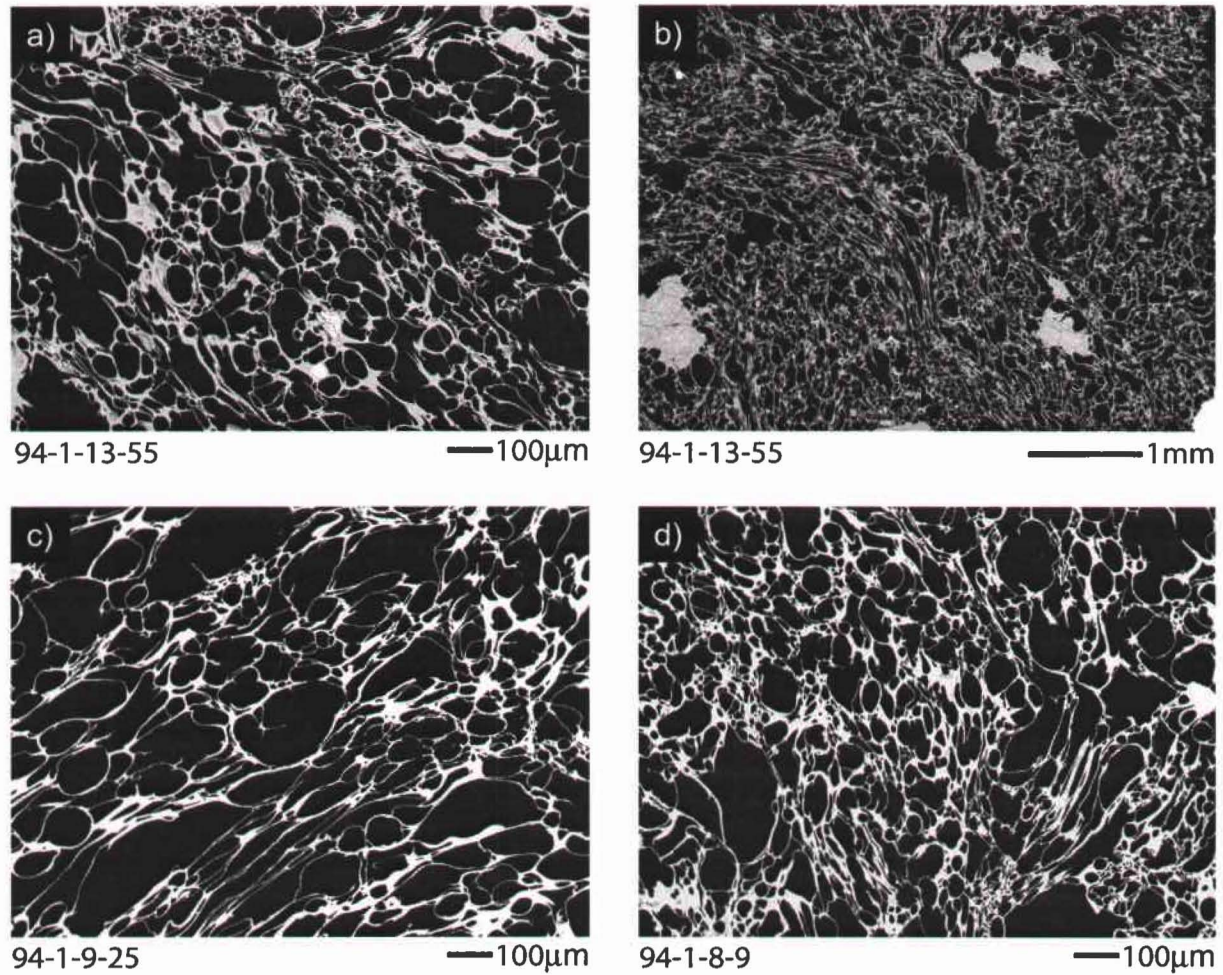


**Figure 2.8** Images representing specific qualitative observations in clasts of different layers. a, b) Layer C; thin bubble walls and bands of elongated bubbles are prominent; c) Layer D; notice the increased abundance of coarser vesicles; d) Layer F; very similar to Layer C.

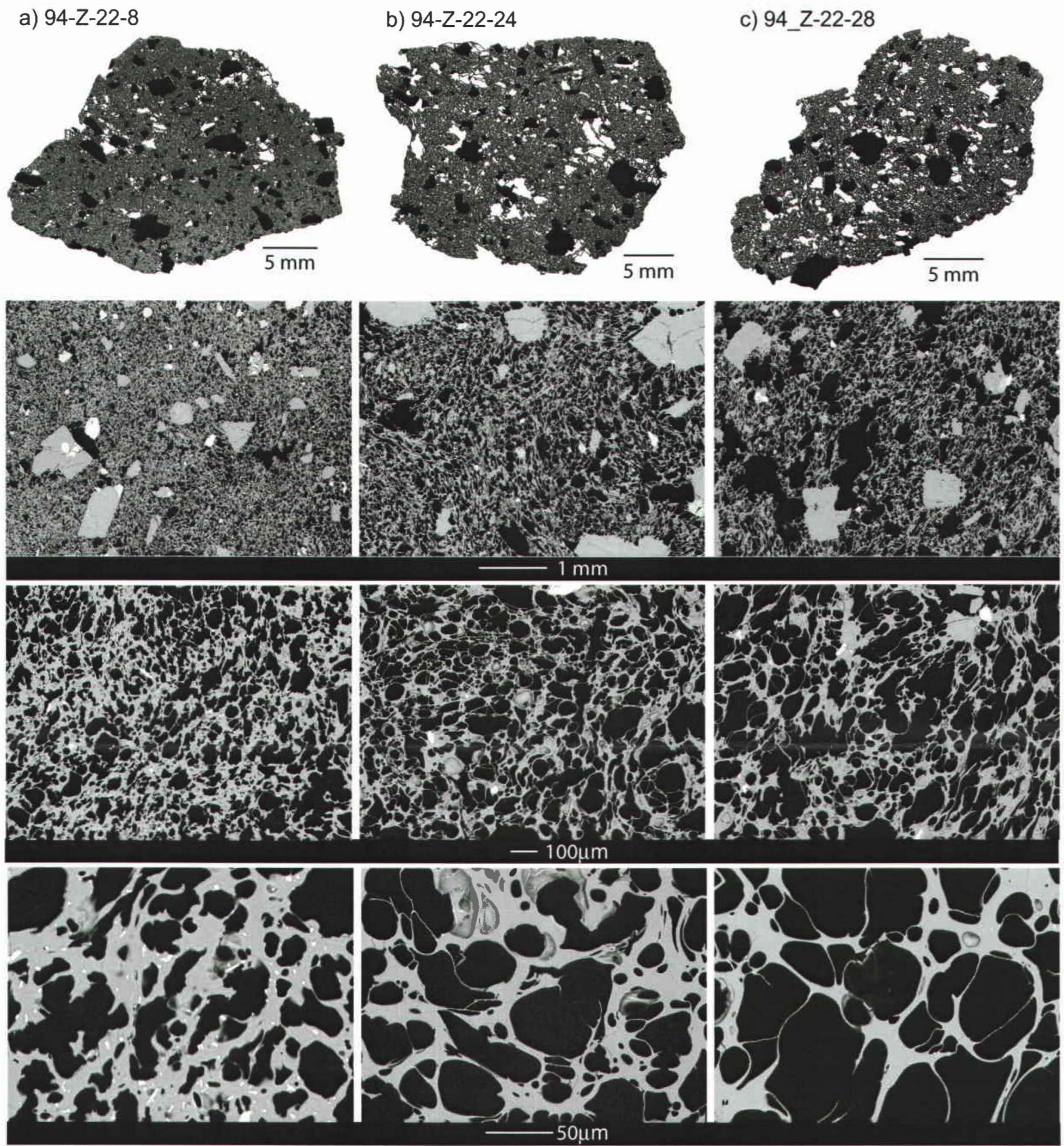


**Figure 2.9** High, modal, and low density clasts (a, b, c, respectively) from Layer G. All show wall thickening and complex bubble shapes.

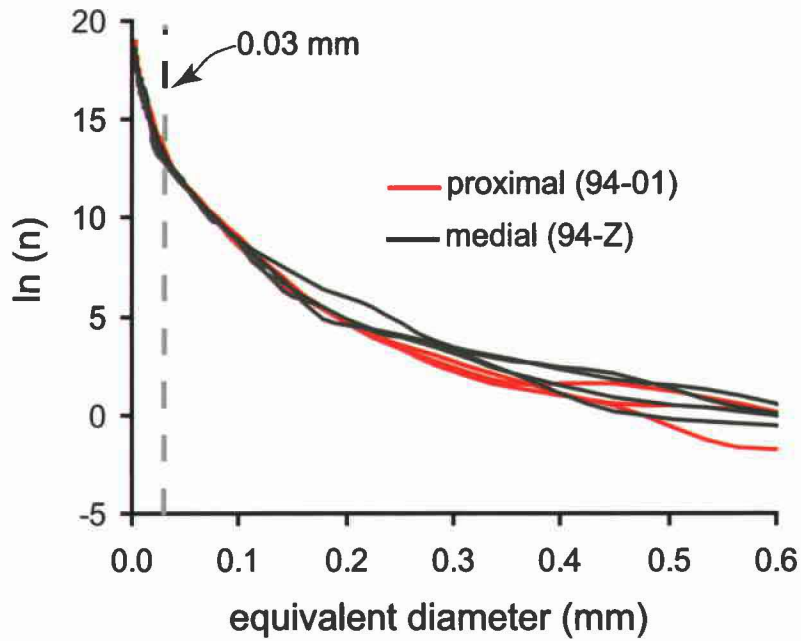


**Figure 2.10** Natural log of population density (no. of vesicles/mm<sup>3</sup>/mm) against vesicle size; vesicles <0.03 mm plot in a straight, steep line and >0.03 mm the data is best described as curved.

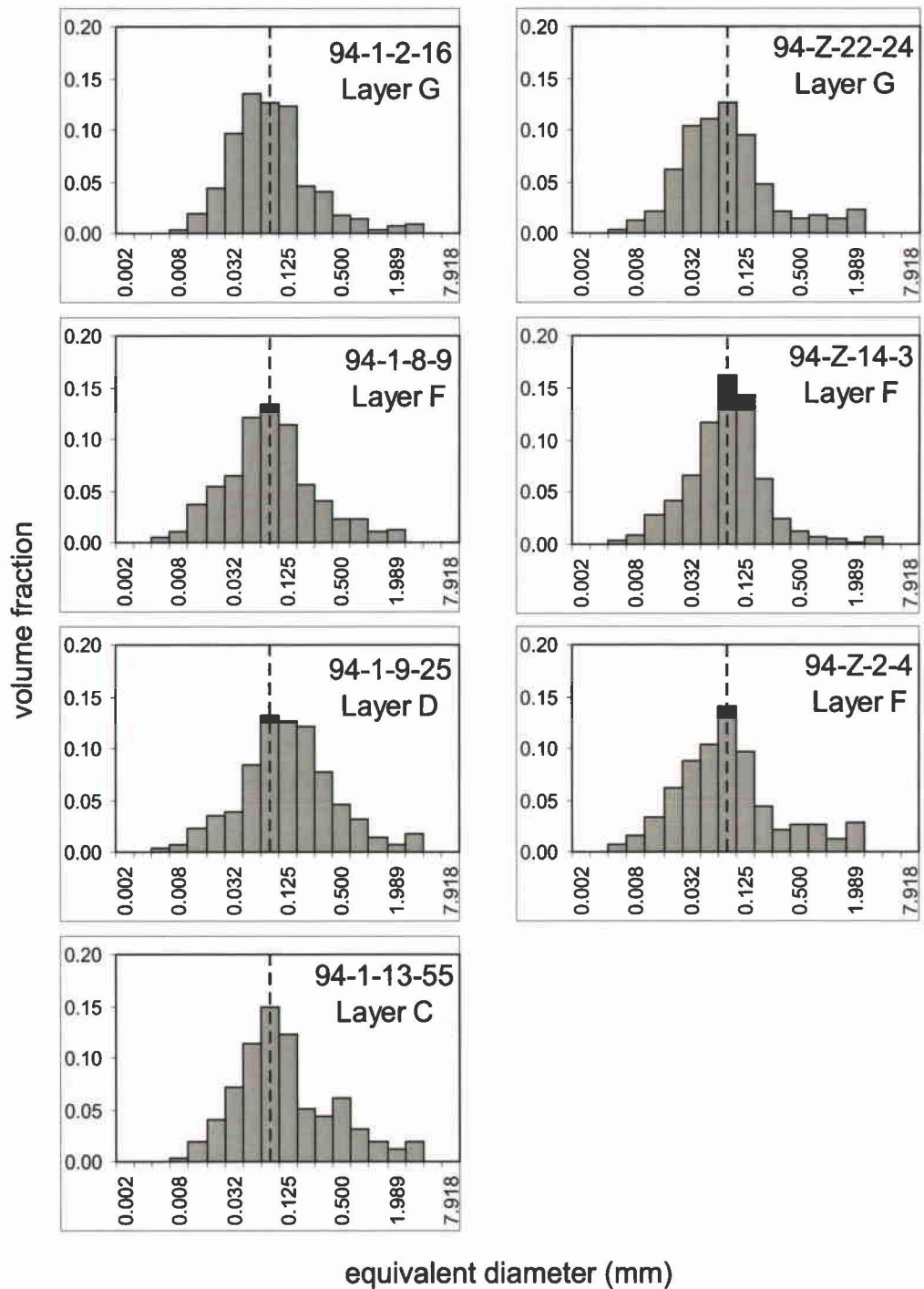


**Figure 2.11** Histograms showing the distribution of volume fraction against vesicle size for the seven studied modal density clasts. Horizontal scale calculated from minimum vesicle size using a geometric factor  $10^{0.1}$  (geometric bin size classes).

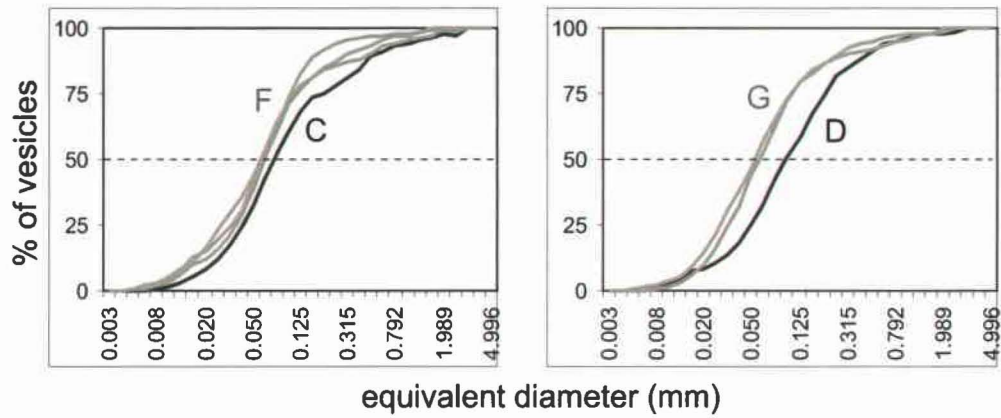


**Figure 2.12** (left) Cumulative volume percent plot for modal density clasts from layers C (black) and F (gray). (right) Cumulative volume percent plot for modal density clasts from layers D (black) and G (gray). The range of median vesicle sizes is wider between the D and G curves than between the C and F curves.

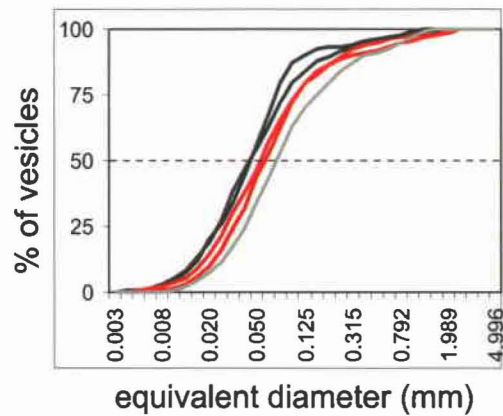


**Figure 2.13** Cumulative volume percent plot for high, modal, and low density clasts from Layer G; modes shown in red, high density in black, low density in light gray.

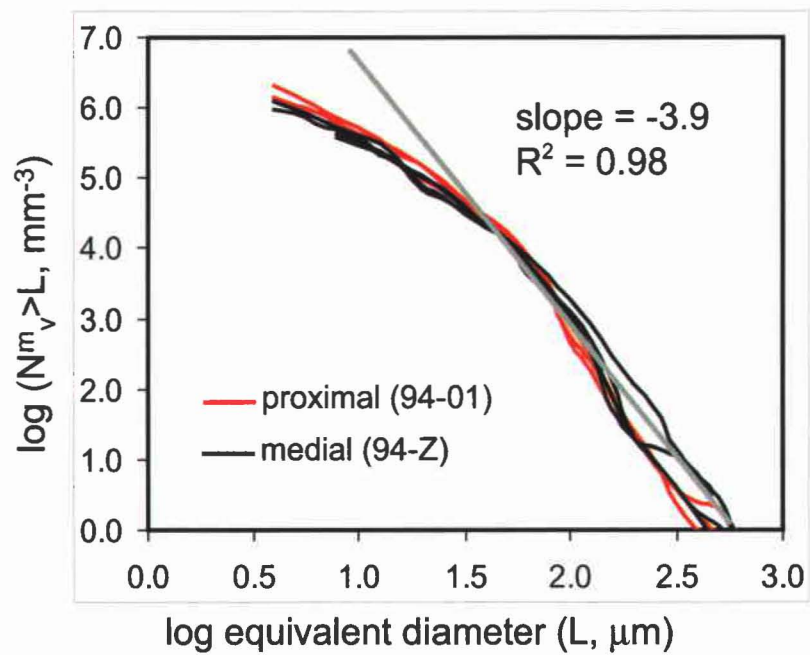


**Figure 2.14** Number of vesicles greater than a given size (cumulative number density referenced to the melt volume) versus size on a log-log plot. The data are best fit by a straight line with a slope of -3.9 until  $\log L = 1.5$  ( $30 \mu\text{m}$ ); for  $\log L < 1.5$  ( $<30 \mu\text{m}$ ), the data are best described as exponential.

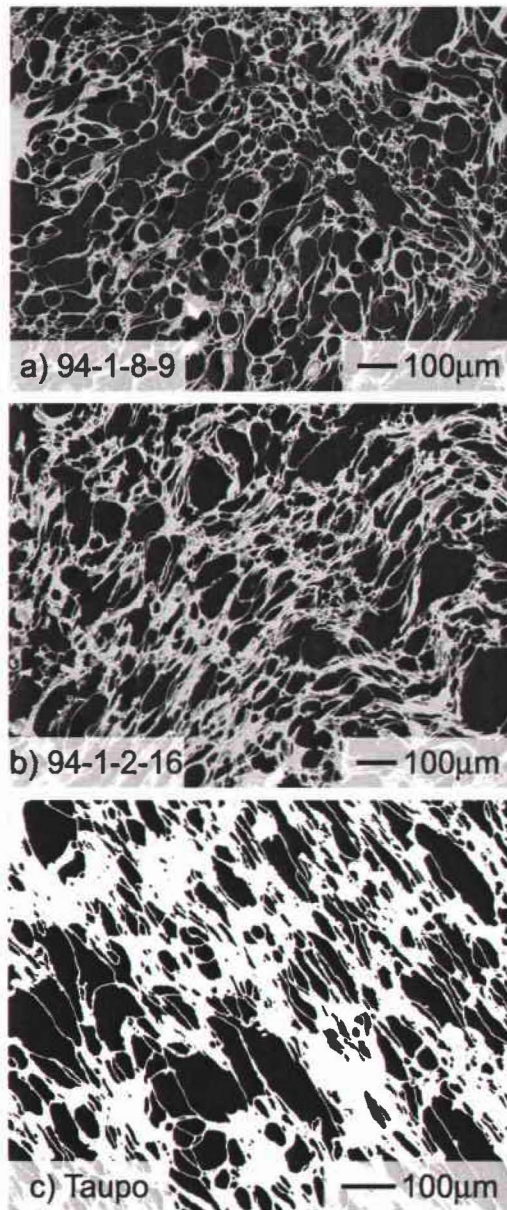


**Figure 2.15** Textures distinctly change from Layer F to Layer G preserving the onset of increased permeability in the melt and gas escape. a) F modal density clast with thin glass walls and a predominance of intermediate-sized bubbles. b) G modal density clast characterized by thicker glass walls, a larger population of small bubbles, and tear-shaped vesicles. c) Sample from Rotongaio ash in the 180 ka eruption of Taupo, New Zealand showing similar textures to Novarupta Layer G. In (b) and (c) textures are the result of bubble collapse and signify maturation of the melt.

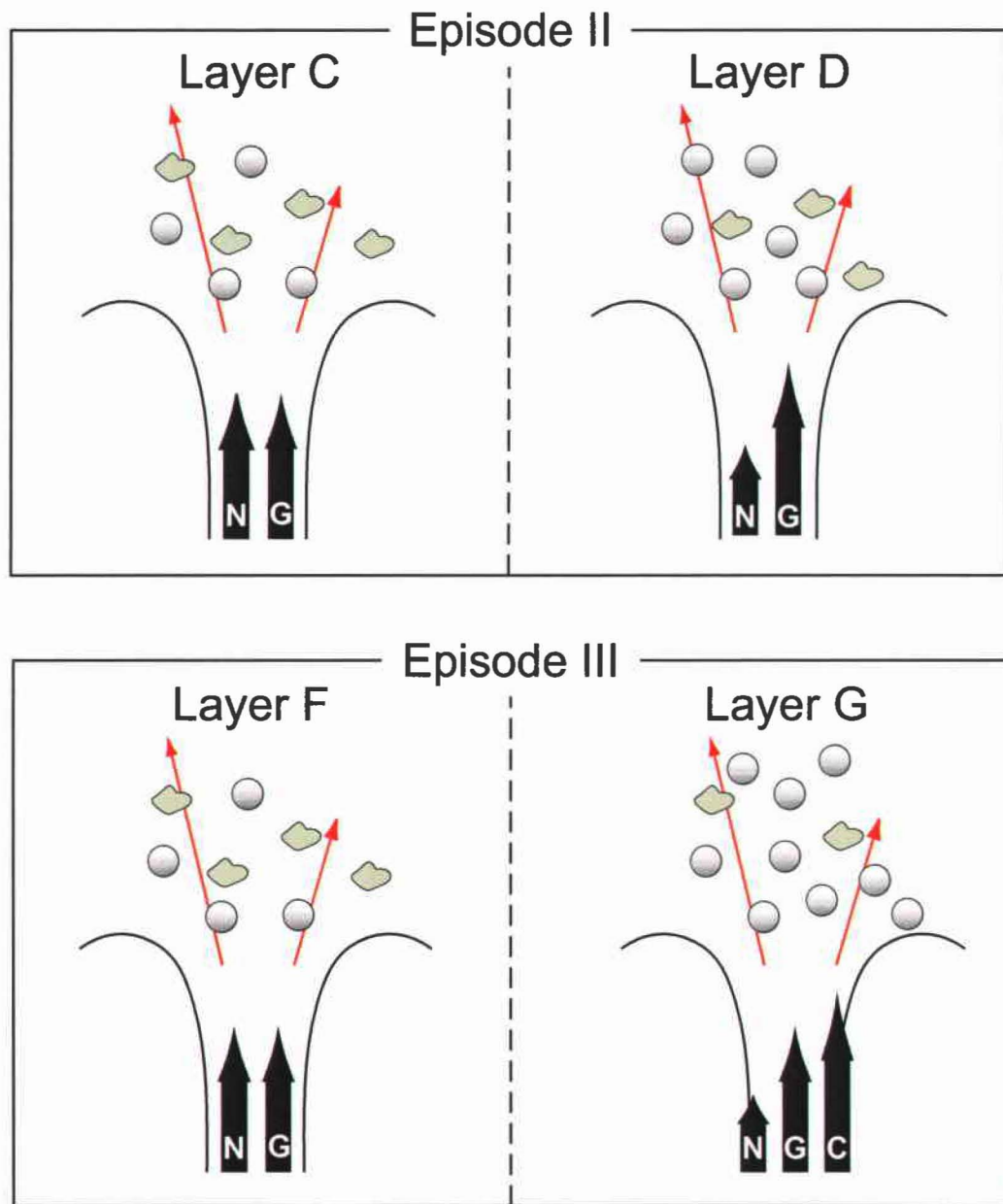


**Figure 2.16** Cartoon illustrating evolution of conduit processes with time based on textural evidence. Size of arrows indicates relative significance of nucleation (N), growth (G), and collapse (C).

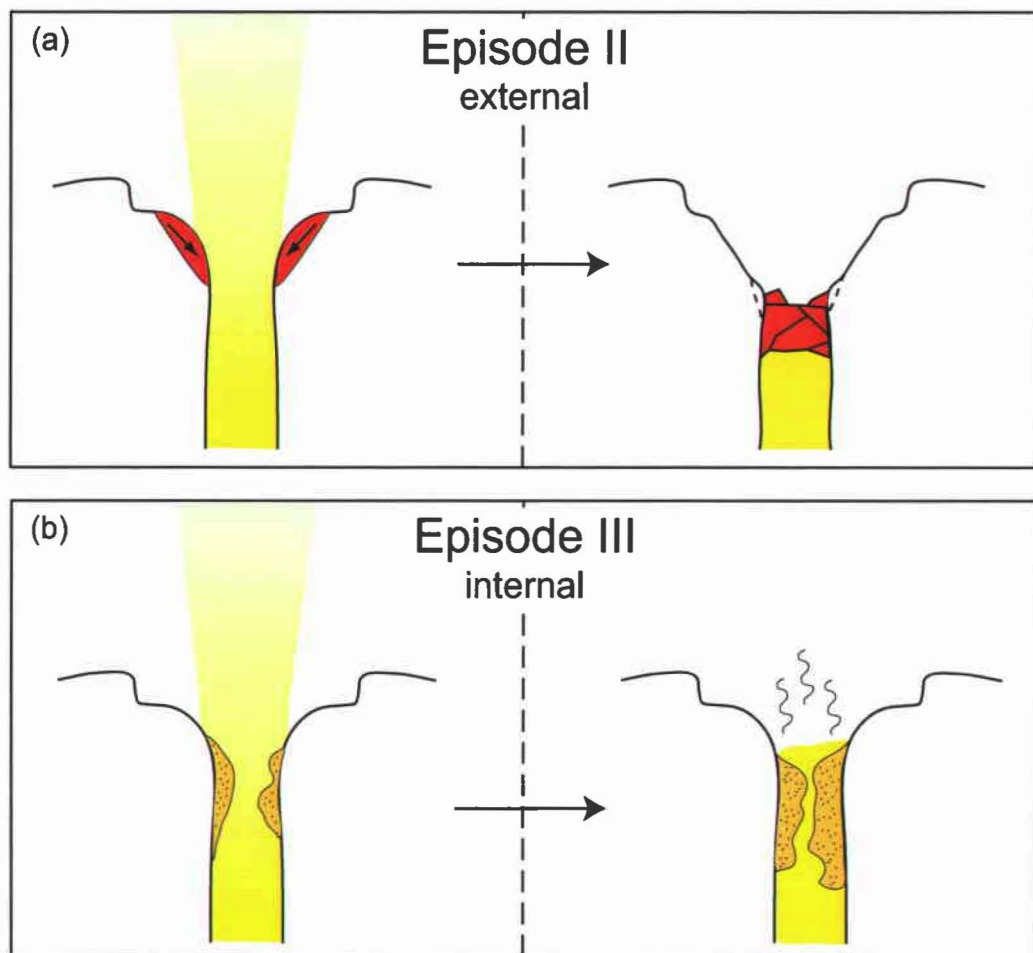


**Figure 2.17** Cartoon illustrating changes to the vent marking the close of Plinian episodes II and III. (a) Instability of vent walls created a blockage and temporarily shut down the eruption during Episode II. (b) For Episode III, internal changes led to the cessation of Plinian activity; maturation of melt allowed free escape of gas. Accumulation of outgassed melt eventually blocked the conduit and was followed by periods of dome growth.

## CHAPTER 3

### **The transition from explosive to effusive eruptive regime: the example of the 1912**

#### **Novarupta eruption, Alaska**

##### **3.1 Abstract**

The transition from explosive to effusive silicic volcanism is a fundamental shift in eruption regime linked to a change in the style of degassing of the erupted magma. This paper focuses on such a transition during the largest eruption of the 20<sup>th</sup> century, the 1912 eruption of Novarupta. Eruption products marking the transition include a dacite block bed which covers an elliptical area of 4km<sup>2</sup> around the vent and overlies the fine ash deposited at the close of Plinian explosive activity. The blocks appear to have mostly followed ballistic trajectories; often blocks broke into pieces upon impact. The largest clasts are up to 12 m<sup>3</sup> in volume or 10<sup>4</sup> kg in mass, and they display a wide range of textures and lithologies dominated by juvenile pumiceous and dense dacite. Approximately 700 blocks have been mapped, measured, and classified into four main lithologic categories: 1) pumiceous dacite, 2) dense dacite, 3) welded breccia, and 4) flow-banded dacite. Textural analyses of pumiceous dacite blocks and dense dacite blocks show portions of the melt underwent highly variable degrees of outgassing. Vesicle size distributions and qualitative observations include markedly coarse bubbles, thick glass walls, and irregularly shaped vesicles, all characteristic of bubble coalescence and collapse. The decrease in and widening range of vesicularity as well as the increasing significance of collapse compared with textural data from Plinian episodes I-

III maps graphically the transition from closed- to open-system degassing. Gas escaping freely led to a termination of magma fragmentation and conduit blockage. Exsolution of volatiles continued, however, in portions of the melt ascending along the axis of the conduit system, promoting extrusion of a dome or plug of partially outgassed and partially actively degassing dacite magma. Block morphology and textures strongly suggest the magma was first erupted as a texturally heterogeneous relatively gas-rich lava dome or plug but the incomplete outgassing of portions of this magma led to explosive disruption. Thus, the block bed formed in a (series of) Vulcanian explosion(s) that followed the close of Plinian volcanism and disrupted dacitic magma which had undergone a very heterogeneous pattern of degassing. Modeling of the dynamics of explosion initiation and ejecta dispersal indicates that a significant concentration in gas over that available within the hot pumiceous dome material is required to produce the explosions responsible for the observed block field dispersal; external water most likely contributed to the ultimate destruction.

### **3.2 Introduction**

Current models link silicic explosive and effusive volcanism to two contrasting patterns of magma ascent and degassing (Jaupart 1996; Massol and Jaupart 1999; Melnik 2000). Explosive eruptions have been characterized by closed-system degassing in which rapid, coupled ascent of exsolved gases and melt lead to late-stage and often disequilibrium degassing (Mangan and Sisson 2000; Mangan et al. 2004). Effusive eruptions follow ascent characterized by open-system degassing where decoupling of

volatiles and melt during ascent in the conduit permits permeable flow and subsequent gas loss to the conduit walls (Jaupart and Allegre 1991; Jaupart 1998; Melnik and Sparks 2002). Eruptions that show explosive-effusive transitions are therefore particularly useful for understanding the switch between closed and open system behavior, i.e., coupling versus decoupling of melt and exsolved gas phases.

The 1980-1986 eruption of Mount St. Helens is an example of an intensely studied volcanic system which made the transition from Plinian explosions to dome effusion (Swanson 1990). After the catastrophic events of May 18, 1980, two domes formed in late June and early August but were explosively destroyed in late July and mid-October respectively. Between October 1980 and 1986, a stable dacite dome grew in a complex series of extrusions which produced ~20 lobes (Moore et al. 1981; Swanson et al. 1987; Anderson and Fink 1989; Fink et al. 1990; Swanson and Holcomb 1990; Anderson et al. 1995). Here we describe indirect evidence for a similar transition during the largest 20<sup>th</sup> century eruption at Novarupta, Alaska, USA in 1912. New field and laboratory data suggest that prior to effusion of the late stage rhyolitic dome at Novarupta [Episode V of Houghton et al. (2004b)], the system erupted a short-lived dacite dome (Episode IV) chemically identical to melt erupted in episodes II and III. The non-survival of this lava, which we infer was destroyed by a succession of Vulcanian explosions, reflects the incomplete and spatially variable pattern of outgassing in the last dacitic melt to reach the vent during the 1912 eruption. Such transitions mark a fundamental shift in eruptive regime thought to be driven by a unidirectional shift from closed to open system degassing.

The block bed created by the disruption of the Episode IV dacite dome is the focus of this paper. We approached this study on three fronts. First, we described the dispersal area of the block bed and block lithologies based on two weeks of intensive fieldwork. Second, we performed microscopic textural analysis on juvenile eruption products to determine ascent and vesiculation patterns. Third, we applied a model of Vulcanian explosion dynamics to better understand the volatile requirements for dome disruption and ejection. The modeling study is the work of professor Sarah Fagents and as such should not be considered as part of this dissertation. However, it is presented here for completeness as it forms an integral part of a manuscript currently under review for *GSA Bulletin*. Based on these three lines of data, the internal changes of the dacite magma during ascent and degassing can be related to a progression of eruptive regimes from plinian to effusion to Vulcanian.

### **3.3 Background**

#### **3.3.1 Explosive and effusive behavior**

Eruptions involving water-rich silicic magmas often follow complex cycles involving different dynamical regimes, i.e., violent explosive phases as well as effusive dome formation. The shift from explosive to effusive eruption is linked to a change from closed- to open-system degassing (Eichelberger et al. 1986; Jaupart and Allegre 1991; Eichelberger 1995; Jaupart 1996). This change is in turn linked to first order factors, e.g., ascent rate, leading workers to predict sudden, drastic transitions between explosive and effusive eruption (Woods and Koyaguchi 1994). Data from recent eruptions suggest the

shift between open- and closed-system behavior is complex and involves nonlinear feedbacks between overpressure, ascent rate, magma viscosity, vesiculation, microlite crystallization, and gas loss (Melnik and Sparks 1999; Barmin et al. 2002; Melnik and Sparks 2002). The microtextures of the eruption products, particularly those formed during the period of transition from explosive to effusive behavior, should therefore preserve this complexity of process.

### **3.3.2 Microtextures**

The complex patterns of magma ascent and degassing during dome growth can be studied via textures of the eruption products. Clast morphology, vesicle size distribution, vesicle shape, and abundance of microlites can be quantified and compared with experimental data (Cashman and Mangan 1994; Mangan and Cashman 1996; Gardner et al. 1999; Mangan and Sisson 2000; Klug et al. 2002; Mangan et al. 2004). When domes have been explosively disrupted, the ejected blocks can be grouped into lithological subgroups; ultimately the size and textural composition of the parent extrusion can be reconstructed. Scanning electron microscope (SEM) and scanned images from polished thin sections can be used to quantify microtextural features and to compare vesicularity and crystallinity among the different eruption products. Vesicle size distributions can constrain the relative timing of processes of bubble nucleation, growth, coalescence, and collapse in eruptions and may be used to understand how the style, timing, and extent of magma degassing influence ensuing eruptive behavior (Mangan et al. 1993; Cashman and Mangan 1994; Polacci et al. 2003). Vesicle size distributions (VSDs) often do not follow the linear trends seen in crystal populations that result from steady state nucleation and

growth (Cashman and Marsh 1988; Marsh 1988; Cashman 1992) but instead indicate complex histories of magma ascent and degassing (Toramaru 1990; Cashman and Mangan 1994; Klug and Cashman 1994; Mangan and Cashman 1996). In this study, we focus on the 1912 eruption of Novarupta to use textures of different lithologies from the Episode IV products to trace the transition from closed to open system degassing.

### **3.3.3 The 1912 eruption**

The eruption of Novarupta on June 6-8, 1912 was the largest eruption of the 20<sup>th</sup> century, producing c. 11 km<sup>3</sup> of ignimbrite and c. 17 km<sup>3</sup> of Plinian fall deposits in ~ 60 hrs (Hildreth 1983; Hildreth 1987). Three episodes of explosive activity produced a succession of Plinian fall deposits and ignimbrite (Fierstein and Hildreth 1992). For many years the prevailing thought was the Plinian eruption was followed by a sharp transition to the passive extrusion of the late stage rhyolite dome now preserved at Novarupta (Curtis 1968; Hildreth 1983). Recent work has recognized that this final episode (Episode V) of stable dome growth was preceded by eruption and disruption of a dacitic dome or plug at the same site (Hildreth and Fierstein 2000; Houghton et al. 2004b). The Episode IV lava was entirely destroyed by explosive activity and is now represented only by a block and lapilli apron surrounding the Episode V dome.

Lack of caldera collapse at the 1912 vent has preserved three concentric, nested structures at the Novarupta vent region: the crater, the ejecta ring, and the Episode V dome. The crater is a 2-km wide depression inferred to be the surface expression of a funnel-shaped flaring vent formed during Episode I (Fierstein and Hildreth 1992). The ejecta ring encloses the current dome which is 380 m wide and 65 m high (Hildreth 1983;

Hildreth and Fierstein 2000). In a  $\sim 4 \text{ km}^2$  area surrounding the vent that includes the ejecta ring and extends beyond the southern boundary of the crater, an apron of dm-m sized Episode IV dacite blocks overlies the fine ash deposited at the close of Episode III (Fig. 3.1). Episode IV therefore represents the transition between explosive activity (Episode III) and extrusion of a long-lived dome (Episode V), and as such, the distribution and products of the Episode IV block bed will be the focus of this study.

### **3.4 The Episode IV block bed**

#### **3.4.1 Field methods**

##### **3.4.1.1 Block size and distribution**

The complete area of block distribution, including regions of poor exposure, was covered in 10 days of field work in July 2003. Over 690 large blocks were mapped in a rough grid with spacings of 10-30 m according to concentration. Documenting a block included marking its position with two kinematic GPS units, measuring maximum, minimum, and intermediate diameter, recording texture and lithology, and collecting a representative sample. A significant number of blocks broke into many pieces upon impact; the point of impact could generally be discerned from the fan-shaped dispersal of the clasts. In such cases, the fragments were fitted together like pieces in a puzzle to reconstruct the dimensions of the original block, and the dimensions of the largest piece were also measured (Fig. 3.2b). When the comminution of the block was extensive and pre-impact block morphology was impossible to ascertain, pieces were gathered into a pile and its dimensions measured (Fig. 3.2c). Error introduced by this method was

assessed in the lab. A block of Styrofoam with known dimensions was carved into >20 pieces. The pieces were shuffled then gathered into a pile and dimensions were measured 10 times (Fig. 3.2d). Average dimension of each pile was  $51\% \pm 3$  greater than the original block, thus, the average dimensions of piles measured in the field were scaled down accordingly. ArcGIS by ESRI was used to create maps showing block distribution. GPS locations for each block and aerial photos were coregistered to 15-minute Alaska DEM data and Arc vector files of topographic maps for USGS Mt. Katmai quadrangles.

#### **3.4.1.2 Block componentry**

The blocks are dacitic in composition but have a wide range of textures and lithologies and include pumiceous and dense dacites and breccias (Fig. 3.3). Many of the blocks were apparently ejected at high temperatures; breadcrust textures are present among all lithologies (Figs. 3.2b, 3.3c). Flow-banding is also common and exists over a range of vesicularities (Fig. 3.3d). Pumiceous and dense dacites were considered juvenile material, i.e., they were newly erupted during Episode IV. The origin of the breccias is more complex. A small portion of the densely welded breccias, or vitrophyres, contains pieces of pre-1912 wall rock; these breccias were classified as nonjuvenile. Lightly and moderately welded breccias, however, appear mostly monolithic; crystal-rich pumice clasts are set in a matrix of similarly vesiculated ash-lapilli sized material. These breccias probably originated as part of the dome carapace but had equilibrated thermally with atmospheric temperatures. Recording lithology therefore consisted of assigning the block to a textural category, estimating degree of vesicularity and crystallinity, and noting the presence of flow bands and breadcrust textures. If the block was a breccia, the degree

of welding was observed, and for flow banded blocks, the type of banding was described. Ultimately, blocks were grouped into breccias, pumiceous dacites, dense dacites, and flow-banded dacites. Breccias were subdivided into lightly, moderately, and densely welded categories, and flow-banded blocks were split into pumiceous, dense, and mixed (mingled pumiceous and dense bands) types. Pieces of blocks were taken at the time of recording and grouped to form samples from each textural subgroup. The number of specimens per subgroup necessarily reflected their relative abundance within the block bed.

To conduct a large-scale componentry exercise, the 100 largest blocks in two fixed areas were counted, measured, and grouped texturally at sites 450 and 608 m west of the center of the Episode V dome (Fig. 3.4). The sites were chosen for their relatively flat slope, remote position from drainages and runoff-influenced zones, and moderate concentration of blocks. Northwest-southeast swaths were made in which every major block was counted until a total of 100 blocks was reached. Collectively, the swaths defined 60 x 60 m and 60 x 40 m rectangles.

### **3.4.2 Distribution of ejecta**

#### **3.4.2.1 Data**

Isolated individual blocks up to 12 m<sup>3</sup> in volume or 10<sup>4</sup> kg in mass form a 4 x 2 km elliptical apron with a N-S dispersal axis (Fig. 3.1). The blocks overlie the Layer H ash deposited at the close of Episode III (Figs. 3.2a, 3.3a); in places the blocks also overlie thin deposits of fluviially and slope-reworked pumice implying that a short time break occurred after the close of the main explosive phase of the 1912 eruption. For two

reasons blocks are inconspicuous in certain sectors within a 0.5-1.5 km radius of the current dome. Blocks are buried by modern alluvial fans S and W of the vent (yellow on Fig. 3.1), and on the steep inner wall of the crater south west of Novarupta, blocks landed but then rolled to accumulate at the break in slope (a-a' on Fig. 3.1).

Distribution by block size has been assessed according to (1) the average dimension of the whole or reconstructed block ( $\bar{d}$ ) and (2) density ( $\rho$ ) multiplied by average dimension ( $\rho\bar{d}$ ) (Fig. 3.5). Both maps show a N-S dispersal axis, and as expected, average block dimension diminishes with distance from the Novarupta vent. On the map of average dimension ( $\bar{d}$ ), the 100 cm isopleth shows much less N-S elongation than the 200 cm, 50 cm, or 25 cm isopleths. This concentric shape occurs because no blocks  $\geq 100$  cm extend directly south of the vent beyond the slope separating the ignimbrite valley floor and the northern flanks of Trident. On the map that allows for density variations among blocks ( $\rho\bar{d}$ ) [method by Parfitt and Wilson (1999)], spurs to the NE and the SE are defined by blocks  $\geq 200$  g/cm<sup>2</sup>. The distribution of block lithologies has also been examined (Fig. 3.6). Higher density blocks, i.e., dense dacites, are slightly concentrated to the south and low density blocks, i.e., pumiceous dacites, to the north, but generally the lithologies are dispersed evenly around the Novarupta dome.

#### **3.4.2.2 Interpretation**

While the isopleths define boundaries beyond which certain sized blocks are not found, the size distribution of the blocks is fairly random. For example, south of the current dome, a 74 cm dense dacite block sits only 260 m from a 27 cm dense dacite block and 770 m from a 25 cm pumiceous block (Figs. 3.5, 3.6). Also, blocks of

approximately the same size but of different lithology and therefore different density traveled nearly equivalent distances, e.g. north of the current dome a 14 cm dense dacite is adjacent to a 15 cm pumice at 1245 m. Given momentum constraints, higher density material should travel further than lower density material of the same size. One explanation for these dispersal discrepancies might include multiple explosions during the Vulcanian phase. The distribution of lithologies in the dome prior disruption in the vent might also influence the dispersal pattern, but this distribution is indiscernible based on the pattern of blocks. Other factors (atmospheric conditions, ejection angles, block shape, etc.) would also certainly affect the final distribution of block size and lithology.

### **3.4.3 Block componentry and morphology**

#### **3.4.3.1 Data**

By number, pumiceous dacites account for the clear majority of the 200 counted blocks at 43.5 % (Table 3.1). Grouping blocks by vesicularity, massive and flow banded pumiceous blocks comprise 53.5% and massive and flow banded dense dacites 24.5%. The remainder is mostly material of intermediate density (flow banded mixed, lightly welded breccia, and moderately welded breccia). If the volume of each block is approximated as the product of the three principal dimensions, both study sites were volumetrically dominated by breccias and pumiceous material. While roughly half of the 200 blocks were pumiceous dacites, approximately one third of the volume of the ejecta in the studied areas is represented by pumice. Collectively breccias represent nearly double the material volumetrically (42%) as they do by point count (21%). Because

pumiceous blocks are more likely to be broken, the correction to inferred dimension of broken blocks further reduces the relative abundance of pumiceous material.

Of the 690 mapped blocks for this study excluding the 200 in the componentry areas, the majority of pumiceous dacites (>60%) broke into pieces upon impact whereas the majority of breccias and dense dacites remained intact (Table 3.2). Not only did a majority of pumices break, but they broke into the most pieces. In fact, 60% of blocks broken into  $\geq 6$  pieces are pumiceous dacites. However, because pumiceous dacites are the most abundant lithology by count, a significant number did remain in one piece.

All lithologies contain some blocks with breadcrust exteriors; of the 690 blocks, 152 were breadcrusted. By lithology, ~30% of pumiceous dacites and ~20% of dense dacites show breadcrust textures whereas over 50% of flow banded blocks are breadcrusted (Table 3.2). Only ~5% of breccias, including the non-juvenile vitrophyres, remained at high enough temperatures to create breadcrust exteriors.

#### **3.4.3.2 Interpretation**

The Episode IV ejecta contain a wider range of juvenile material than seen in the Plinian falls of episodes I through III and indeed in any deposit of a Plinian eruption. While compositionally the blocks are similar to the dacites of episodes II and III, the textural diversity of the deposit suggests an original eruption style much closer to dome emplacement and disruption. The range of block lithologies is matched by that seen in other silicic domes, e.g., the finely vesicular pumice, obsidian, coarsely vesicular pumice, and dense lava categories of Fink and Anderson (2000). The distribution of these textures within a dome is complex (Fink and Manley 1987), but most domes contain two

distinct textural end-members with greater than 50% and less than 30% vesicles which match the pumiceous and dense dacites of the 1912 block bed.

The high degree of breakage apparent in all block lithologies as well as the fan-shaped dispersal of the blocks broken into  $\geq 10$  pieces is consistent with emplacement along ballistic trajectories. Widespread breadcrust textures indicate high temperatures of the ejected material and ongoing vesiculation even after fragmentation and also support the origin of the block bed as a hot, dacite dome destroyed by Vulcanian eruption(s).

### **3.5 Vesicularity of juvenile material**

#### **3.5.1 Techniques**

To study the processes of degassing and vesiculation occurring in the conduit at Novarupta, bulk density of samples was determined after Houghton and Wilson (1989) and the data used to select representative clasts for textural study in thin section.

Heterogeneity in vesicle size and shape in a single thin-section necessitates several strategies for textural analysis. Following Chapter 2, images at different magnifications were captured and analyzed and vesicle size data combined in order to completely characterize the size distribution of the vesicles. Vesicle areas were binned by size and converted to area ( $N_A$ ) and volume ( $N_V$ ) number densities following the method of Sahagian and Proussevitch (1998). The cumulative number density ( $N_{V \text{ total}}$ ) referenced to the matrix of the clast, i.e., total clast volume less the phenocrysts, was determined by summing the number density for each bin size ( $N_V$ ). Cumulative number densities referenced to the melt volume ( $N_{V \text{ total}}^m$ ) have also been determined to allow for the

misleading effect of the vesicle population itself on the number density (Klug et al. 2002).

### **3.5.2 Density and bulk vesicularity data**

Densities measured for the juvenile pumiceous and dense dacite blocks reflect a wide range of vesicularities and textures. The densities of the pumiceous blocks range between 310-1250 kg/m<sup>3</sup> (Table 3.3), and the modal density of this sub-population (900 kg/m<sup>3</sup>) corresponds well to the modes of the pumices deposited during the close of the Plinian activity (900-1000 kg/m<sup>3</sup>) (Fig. 3.7). Not surprising, the measured densities for the dense blocks are much higher; the majority ranges between 1940-2650 kg/m<sup>3</sup>. Out of the 229 pumiceous and dense dacite blocks used to measure density, only three had densities between 1530-1690 kg/m<sup>3</sup>. With the exception of these few transitional pieces, the pumiceous and dense dacites show no overlap in density values; a gap between 1250-1940 kg/m<sup>3</sup> clearly defines the two groups.

The surface of the rhyolitic Novarupta dome which, based on the first eyewitness accounts, has occupied the vent for a minimum of 88 years, was also sampled, and densities were likewise determined. Measurements for this stable, long-lived dome lie almost perfectly in the gap seen in the density data for the block bed dacites (1300-2170 kg/m<sup>3</sup>).

### **3.5.3 Qualitative observations of vesicularity**

High (1060 kg/m<sup>3</sup>), modal (840 kg/m<sup>3</sup>), and low (310 kg/m<sup>3</sup>) density specimens from the sample of pumiceous dacites (HP, MP, and LP, respectively) were selected for image collection and analysis. A transitional (T) block (1690 kg/m<sup>3</sup>) between the

pumiceous and dense dacites and two low density dense dacites (D1 and D2, respectively) (2040 and 2240 kg/m<sup>3</sup>) were also selected to examine the shift between pumiceous and dense juvenile material. Specimens with densities of 1490, 1740, and 1970 kg/m<sup>3</sup> taken from Episode V dome (R1, R2, and R3, respectively) were also analyzed (Fig. 3.7).

Microscopic textures in the dacite pumiceous blocks of the Episode IV dome show a progression in vesicle sizes and wall thicknesses with changing density (Fig. 3.8). Images of LP are reminiscent of pumices typical of the last phase of plinian Episode III (Chapter 2). Internal heterogeneity, i.e., regions where small bubbles are concentrated adjacent to regions rich in medium-coarse bubbles, characterizes LP. Heterogeneity decreases with increasing density; the distribution of a range of vesicle sizes and wall thicknesses are fairly uniform in HP. A significant population of 2-5  $\mu\text{m}$  walls is visible in LP, and while still present, their significance greatly diminishes in MP which is clearly dominated by 10-15  $\mu\text{m}$  walls. Thin walls are absent in HP; observed walls are consistently >25  $\mu\text{m}$  thick. In all three pumiceous blocks, small bubbles are mostly associated with thicker glass walls and appear either spherical or with pinched ends. Banding is absent in MP and HP. However, bands 0.5 – 1 mm in width that include stretched mid-sized vesicles separated by thin glass walls as well as thicker walls with small, pinched vesicles sweep through the images of LP.

While indicators of bubble coalescence are abundant throughout the pumiceous dacite, the variety of features decreases with increasing density (Fig. 3.8). Smaller bubbles expanding into larger ones are preserved only in LP. Wrinkling of thin bubble

walls separating medium-to-coarse bubbles and incomplete retraction of glass films following rupture clearly occur in both LP and MP. Thin, linear glass films separating two bubbles with approximately equal internal pressure are also seen in both LP and MP images. The above mentioned features are almost completely absent from HP, and the bubbles are separated by wide areas of bubble-free glass. However, most of the bubbles have an amoeboid shape, suggesting an earlier history of bubble coalescence. If walls are unable to relax and regain sphericity after two or more bubbles combine, the resulting vesicle would have a complex shape as seen in all three pumices.

Block T, representing the few blocks with measured densities between the pumiceous and dense dacites ( $1500-1700 \text{ kg/m}^3$ ), shows alternating domains distinguishable by coarse vesicles. One type of domain has a population of mm-sized vesicles whereas the largest bubbles in adjacent areas are only  $\sim 25 \mu\text{m}$  in diameter (Fig. 3.9a). In the 2-D view, the domains appear to define finely-spaced bands; however, in 3-D the geometry of the domains is more irregular. Some thin ( $2-5 \mu\text{m}$ ) and intermediate ( $10-15 \mu\text{m}$ ) walls are seen in the coarse-vesicle domain but thick walls ( $>25 \mu\text{m}$ ) clearly dominate when the coarse-vesicles are not present. Amoeboid bubble shapes throughout T indicate coalescence played a significant role in the vesiculation history, but the loss of concavity and overall smoothness of the bubble outline as well as a pinched appearance describes textures created by collapse. The progression of changing textures with increasing density of the pumiceous blocks is continued in the bubble populations of the dense dacites ( $\geq 1690 \text{ kg/m}^3$ ). Coarse vesicles ( $\sim 750 \mu\text{m}$ ) remain in D1 (Fig. 3.9b), but bubble shapes are extremely irregular regardless of size, and the distribution of vesicles is

largely heterogeneous. While foliation is not present, vesicles over  $\sim 500 \times 500 \mu\text{m}$  areas have a stretched or flattened appearance. The contrasts between D2 and the pumiceous dacites (LP, MP, and HP) are even more severe. Voids are sparse, have irregular outlines, and show no clear association with phenocrysts (Fig. 3.9c). Microfractures are also increasingly pervasive in the higher density blocks throughout the glass and crystals.

The most striking feature of the rhyolite Episode V dome specimens is a stretched appearance of the vesicles (Fig. 3.10). Vesicles of all sizes are elongated in the same direction; however, the vesicles themselves are not segregated into bands. As in the Episode IV dacites, vesicle size decreases and glass walls thicken with increasing density (from R1 to R3). Also, bubbles can increasingly be described as pinched or even angular in the denser rhyolite Episode V specimens and microfractures become extensive.

#### **3.5.4 Quantitative observations of vesicularity**

Vesicle volume distributions (VVDs) can be used to assess the contributions of different vesiculation processes, e.g., a dominance of bubble coalescence will generally produce bimodal populations visible on histograms of volume fractions versus bubble diameter (Orsi et al. 1992; Klug and Cashman 1994; Klug and Cashman 1996; Klug et al. 2002). On such plots, the vesicle populations from the pumiceous blocks LP, MP, and HP are unimodal like those of the plinian pumices of Episode III (Chapter 2), but all show a tail extending to 2-3 mm bubble sizes which can be attributed to coalescence (Fig. 3.11). With increasing density (decreasing vesicularity) the size mode for the bubbles shifts from  $125 \mu\text{m}$  (LP) to  $50 \mu\text{m}$  (HP). The data can also be plotted as cumulative volume fraction versus diameter size, and the median vesicle sizes can be determined at

the intersection of the curves with the fiftieth percentile. For the pumiceous blocks, the median sizes of LP and MP are closer in value to each other and larger compared to HP (Table 3.3). The timing and duration of bubble nucleation and collapse is also recorded in the cumulative number densities ( $N_{Vtotal}$  and  $N_{Vtotal}^m$ ). HP has the smallest  $N_{Vtotal}$  and  $N_{Vtotal}^m$  values of the dacite pumices (Table 3.3).

The complex-shaped voids in the thin sections of the denser dacites ( $\geq 1690$  kg/m<sup>3</sup>), i.e., T, D1, and D2, as well as the intermediate (1740 kg/m<sup>3</sup>) and high (1970 kg/m<sup>3</sup>) density Episode V dome samples (R2 and R3) cannot be quantified by the above described methods, thus VVDs and cumulative number densities have not been determined. Statistical problems arise from too few bubbles per clast, and the irregularity in shape makes sphere-based conversions to volume invalid.

### **3.5.5 Interpretation**

All quantitative data from the pumiceous Episode IV blocks point to 1) an extended and diverse vesiculation history, and 2) a continuation of the changes first observed at the end of Episode III (and documented in Chapter 2). Early exponential nucleation and growth was overprinted by bubble coalescence as melt advanced through the conduit and then, in turn, for some portions of the magma by the onset of bubble collapse. Qualitatively, bubble coalescence is apparent throughout the pumiceous dacites, but quantitatively its influence on the bubble size distribution diminishes in the denser blocks as bubble collapse becomes a dominant process. Not only are coalescence features less prominent in HP compared to MP and LP, but the glass walls are noticeably thicker, the distribution of sizes is less heterogeneous, and the dominant bubble size is

smaller (Fig. 3.8), all consistent with collapse of bubbles. The median bubble size is more than 20  $\mu\text{m}$  smaller for HP compared to MP and LP (Fig. 3.11, Table 3.3); coalescence drives bubble size distributions toward larger sizes (Cashman and Mangan 1994), and while coalescence features are also evident qualitatively, collapse has had a stronger effect on the size distribution in HP. The significance of collapse in HP is also reflected by the lower cumulative number density and the smaller modal value on the VVD histogram. Collapse would be expected to reduce the total number of bubbles and the overall bubble size. HP has the smallest  $N_{\text{total}}^{\text{m}}$ , and despite coalescence-created coarse tails, peak values decrease with increasing density on VVD histograms (Fig. 3.11, Table 3.3). We suggest this trend reflects contrasts in residence time in the dome and shallow conduit as discussed in detail below.

The density gap between pumiceous and dense dacite is matched by striking dissimilarity between the bubble populations. However, the dense dacites appear to have similar but more extended vesiculation histories than their pumiceous analogs. Low vesicularity, observably low bubble number densities, and the irregular distribution of clusters of pinched and deformed vesicles in areas of vesicle-free glass suggest the dense dacites are the end products of outgassing and bubble collapse. We suggest the apparent gap between dense and pumiceous dacite of Episode IV is strong, indirect evidence that once bubble collapse is initiated by the onset of permeability, it is a catastrophic process that advances rapidly to completion and generates an outgassed and rheologically stiffened melt phase.

### **3.6 Dynamics of block bed emplacement**

#### **3.6.1 Methodology and model parameters**

To understand better the cause and mechanism of disruption and ejection of the Episode IV dome, the dynamics of explosive dispersal of ballistic blocks around the vent site can be modeled. We adopt the numerical method of Fagents and Wilson (1993) which treats the dynamics of transient (Vulcanian) explosions. This model takes as its starting point an amount of gas held at pressure which, following sudden decompression, displaces and accelerates a dense slug of cap-rock plus a mass of atmospheric gas overlying the explosion site. The Fagents and Wilson (1993) model integrates the equation of motion of the solid and gaseous ejecta to yield the ejection velocity. This velocity is then used as the starting condition to compute the ballistic trajectories and landing points of dome fragments, subject to the aerodynamic forces imposed by the motions induced in the volcanic and atmospheric gases. Mapped locations of blocks can be used to infer initial velocities, pressures, and volatile concentrations. The objective is to determine whether estimated gas masses and pressures can plausibly disperse the blocks to the distances observed in the field.

For the Novarupta Episode IV block bed, bubble collapse to form surface and near-surface dense dacite might have actually hindered outgassing of enclosed and still actively degassing pumiceous lava. Continued gas exsolution would then have led to a rise in gas pressure at greater depths within the dome and conduit. Initiation of an explosion would have occurred once the gas pressure exceeded that due to the overlying dome mass or when the cool outer dome material failed in a brittle manner.

Modifications of the Fagents and Wilson (1993) model permit application to the Novarupta dome disruption scenario. We employ a range of model parameters constrained by the field data:

(i) Bubble textures and breadcrust exteriors to blocks suggest the dome was only partially solidified prior to disruption and ejection. The pre-explosion gas pressure would therefore have had to overcome the lava viscous yield strength and only a minimal tensile strength. An upper limit for these strengths, based on measurements of pristine samples of igneous rocks might be ~10 MPa (Touloukian et al. 1981). However, thermal stress, and the presence of pressurized gases, and high crystal contents in hot dacite dome material could greatly reduce the rock strength to much lower values (Mellors et al. 1988; Sato et al. 1992). Perhaps a more important consideration is the depth from which the explosion initiated, e.g., a depth of 100 m beneath the dome surface corresponds to a hydrostatic pressure of ~2.5 MPa. An extreme limit is perhaps 1000m depth (25 MPa) if fragmentation extended to deep in the conduit. Given the uncertainties in the strength of dome material, we therefore adopt a range of initial pressure of 2.5 to 25 MPa.

(ii) The model requires a value of the mass ratio,  $n$ , of gas to solid ejecta. Pre-explosion gas concentrations can be derived from the vesicularity of ejecta. Let us initially consider that the explosions were driven only by magmatic gas expanding within pumiceous dacite melt but which ejected a range of block types derived from overlying capping lava. The pumice represents ~16.6% by volume of the ejecta, and an average pumice vesicularity of 68% implies that ~11% by volume of the pre-ejection dome material was gas available to drive the eruption. This volume can be converted to gas/solid mass ratio once we know

the gas density, which will be a function of the confinement pressure and gas temperature. Using the 2.5–25 MPa range above with a temperature of 600°C yields gas/solid mass values of  $n=0.002\text{--}0.0045$  (0.2–0.45 wt%).

The model was run for a variety of blocks ranging in size from 0.25 to 2.3 m in average diameter, having densities from 860 kg/m<sup>3</sup> (pumice) to 2390 kg/m<sup>3</sup> (dense dacite), and ejected to distances from 230 to 2200 m from the vent. Differences in the elevations of the ejection and impact sites were also noted. Atmospheric conditions corresponding to the Novarupta location were incorporated into the model, and the optimum ejection angle of 45° was adopted to derive the minimum required velocities. Finally, the ejection and trajectory-tracing algorithms were run to investigate the conditions required to produce the observed block distribution.

### 3.6.2 Results

We find that blocks projected to the medial and distal portions of the block field require significant enhancement in gas over that provided by the pumice alone. Typically, blocks ejected beyond ~1 km require  $n > 0.015\text{--}0.040$  (>1.5–4 wt%), and ejection velocities in the range 100–200 m s<sup>-1</sup> (Fig. 3.12). Some blocks, particularly the smaller, low-density pumice clasts, require gas/solid mass ratios and ejection velocities that we deem to be unrealistically high ( $n > 10\text{--}20$  wt%,  $u > 400$  m/s). In these cases, a role for convective support and/or wind dispersal is probably implied for these distances to be attained. Alternatively, some of these blocks may have broken in flight. Larger blocks falling within 1 km of the vent require much lower ejection velocities (45–75 m/s) and gas/solid mass ratios (0.4–1 wt%) (Fig. 3.12) much closer to those provide by pumice-

derived gas alone (0.2–0.45 wt%). However, given that we have adopted only the optimum ejection angle, these values are minima – the proximal blocks could just as plausibly have been ejected in more intense, gas-rich explosions but at greater launch angles, to follow steeper trajectories and land closer to the vent. Nevertheless, significantly higher gas abundances are implied for at least some of the 1912 explosions.

### **3.7 Discussion and conclusions**

#### **3.7.1 Magma ascent and degassing**

Textures in the dacitic pyroclasts of Episode III and the Episode IV block bed reflect the changing degassing conditions of a system shifting between explosive to effusive eruption styles via an interval of transient growth of an unstable and texturally heterogeneous lava dome. Reduced mass flux and ascent velocity by the end of Episode III was accompanied by a partial switch between closed- and open-system degassing which preferentially affected melt ascending along the margins of the conduit (Chapter 2). Melt along the conduit axis continued to ascend rapidly and to nucleate and grow vesicles, but rheological stiffening accompanying degassing caused stagnant melt to increasingly line the conduit margins and effectively reduced the radius of the conduit. This degassed material eventually blocked the shallowest levels of the conduit, and Plinian activity stopped altogether. However, volatile-rich material which remained deeper in the conduit continued to rise, driving the outgassed but still fluid melt through the conduit to form a dome or plug.

We thus picture a combination of coeval open- and closed-system degassing occurring in the conduit during an essentially unstable transition period (between stable Plinian eruption in Episode III and stable dome growth in Episode V). The pumiceous component of the assemblage of blocks represents the initially deeper melt characterized by an ascent history similar to the dacite of Episode III, i.e., it experienced closed-system and disequilibrium degassing. Ascent of this deeper magma drove dome extrusion, and it involved the relatively dense, outgassed magma in its ascent. Fingers of relatively hot, vesiculating magma intruded the cooler, denser, and largely outgassed material (Fig. 3.13) so that the dome/plug was characterized by both dense and pumiceous dacite (Fig. 3.14). The bimodal distribution of textures, i.e., dense versus pumiceous dacite, may reflect rapid 1) onset of a short period of permeability and gas escape from melt, or 2) a time gap between the arrival of the melt forming the dense dacite at the end of Episode III and ascent of the pumiceous dacite. Westrich and Eichelberger (1994) suggest bubble collapse is followed quickly by a decrease in permeability and the system then closes to gas flow; the time interval of bubble collapse is, a priori, short. At Novarupta, loss of permeability through catastrophic bubble collapse in portions of the ascending melt might have led to a release of exsolved volatiles and disruption of the dome through Vulcanian explosion(s). Perhaps Episode IV was analogous to historic eruption of silicic domes which exhibit cyclic activity of extrusion and disruption caused by reduced permeability and subsequently increased pressurization, e.g., Lascar Volcano, Chile, and Soufriere Hills Volcano, Montserrat, British West Indies (Matthews et al. 1997; Voight et al. 1999). The model proposed by Matthews et al. (1997) involves extrusion of dome lava

accompanied by vesiculation in the conduit and dome interior. Partial degassing through permeable vesicular magma leads to bubble collapse and inhibition of open-system degassing. Minor explosions are related to discrete collapse events in the shallow environment, and major eruptions involve loss of permeability at greater depths. In terms of textures, the Episode IV dome fits this model for cyclic dome growth. The distribution of blocks by size does not exclude multiple explosions, but currently we can only speculate if the activity during Episode IV was cyclic in nature.

Why was the Episode IV dome unstable and Episode V characterized by stable dome growth? We suggest a greater degree of textural heterogeneity in the dacite melt effected the outcome of the Episode IV dome. Compared to lava from the stable Episode V dome, Episode IV blocks have a wider range of vesicularities and bubble sizes. While both episodes show textures implying bubble collapse, the diversity in textures within the Episode IV magma shows that portions of it were characterized by closed-system vesiculation. A component of the dacite melt that underwent rapid disequilibrium degassing resulted in a dome that was at minimum on the verge of fragmentation/eruption; modeling suggests a possible addition of external water. Conversely, the textures in the Episode V dome represent long-term and more consistent open-system degassing, which follows for a melt resident in the shallow conduit since the close of Episode I. These textures perhaps represent a later stage of development involving extended residence in the shallow conduit and passive outgassing.

### 3.7.2 Model for dome fragmentation

Our preferred model for fragmentation of the Episode IV dome includes rapid expansion of magmatic volatiles formerly trapped in rising pumiceous dacite. One scenario that might involve such rapid expansion and catastrophic release of gases follows the model discussed by Matthews et al. (1997). The Episode IV block textures are indicative of cyclic dome growth involving disruption after an increase in pressurization caused by reduced permeability (e.g. Matthews et al. 1997). Continuing with that scenario and again considering the heterogeneity of the Episode IV dome, volatiles escaping from the pumiceous material could be partially trapped and concentrated by denser material. A weakness such as a fracture or gravitational collapse of part of the dome edifice might have breached this pressurized gas that was localized within the dome complex and triggered an explosion. Similar models are suggested by Voight and Elsworth (2000) for dome collapse and by Ui et al. (1999) for generation of block and ash flows. In section 3.6, we shifted our attention from textural observations and considered the amount of gas needed versus the amount available to ballistically emplace blocks characterized by the Episode IV densities, shapes, and distances traveled. In these terms of gas/solid mass ratios, a second scenario is envisioned. The high gas/solid mass ratios required for the dispersal of smaller, low-density blocks suggest an additional source of gas, perhaps via external water, to the system. Given the Alaskan climate and the timing of the eruption, two possible precipitants may be relevant. Rainfall that occurred after the dome was largely extruded but was still relatively hot could have entered the magma through cracks and microfractures. Alternatively, while

snowfall is not common from late June through August at Katmai, snow that predated the Plinian eruption on 6 June could have been trapped below the pyroclastic fall deposits which filled the crater. Both of these sources might have provided sufficient external volatiles to assist Vulcanian explosions driven predominantly by the expanding magmatic volatiles. Furthermore, the intrusion of external water to pockets of trapped gas (as previously described) might trigger fragmentation of portions of the dome and lead to ultimate destruction.

### **3.8 Acknowledgements**

Colin Wilson and Judy Fierstein played a major role in the fieldwork that established a stratigraphic framework for this project. Our work was supported by NSF grant EAR-01-06700. Images were collected on the SEM belonging to HIGP (Hawaii Institute of Geophysics & Planetology).

**Table 3.1** Relative abundance of lithological groups in individual componentry areas.

	Rectangle 1 (%)			Rectangle 2 (%)			Combined (%)		
	D1*D2*D3	(avgD) <sup>3</sup>	count	D1*D2*D3	(avgD) <sup>3</sup>	count	D1*D2*D3	(avgD) <sup>3</sup>	count
<b>breccia dw</b>	14.6	19.3	11.9	11.1	13.7	9.1	13.2	16.9	10.5
<b>breccia lw</b>	1.6	2.1	3.0	4.1	4.6	3.0	2.6	3.2	3.0
<b>breccia mw</b>	20.5	28.5	6.9	33.4	39.4	7.1	25.9	33.2	7.0
<b>dense dacite</b>	3.2	4.0	20.8	11.2	14.0	18.2	6.5	8.3	19.5
<b>fb dense</b>	1.7	2.3	5.9	2.1	2.3	4.0	1.8	2.3	5.0
<b>fb mixed</b>	0.1	0.2	1.0	1.3	1.3	2.0	0.6	0.7	1.5
<b>fb pums</b>	27.4	28.3	9.9	5.0	6.2	10.1	18.2	18.9	10.0
<b>pums</b>	30.9	15.2	40.6	31.8	18.4	46.5	31.3	16.5	43.5

**Table 3.2** Characteristics of eight lithological groups.

Lithology	min <sup>1</sup>	mean	max <sup>2</sup>	breadcrust		% of pieces					% of lithology					
	density	density	density	% of	%	# of broken pieces					# of broken pieces					
	(kg/m <sup>3</sup> )	(kg/m <sup>3</sup> )	(kg/m <sup>3</sup> )	bc	of lith	1	2--5	6--10	11--20	20+	1	2--5	6--10	11--20	20+	
breccia dw	1870	2180	2400	3	4	23	15	5	5	0	73	19	5	3	0	100
breccia lw	1080	1170	1260	0	0	3	1	0	0	0	90	10	0	0	0	100
breccia mw	1370	2080	1720	3	7	9	15	8	5	0	47	33	15	5	0	100
dense dacite	1940	2390	2650	28	21	36	35	17	13	0	62	24	11	3	0	100
fb dense	<sup>3</sup> 2190	<sup>3</sup> 2190	<sup>3</sup> 2190	6	41	3	1	4	5	0	55	9	23	14	0	100
fb mixed	1290	1470	1740	3	83	1	0	2	2	0	50	0	33	17	0	100
fb pumiceous	730	1120	1560	7	65	0	2	7	9	0	0	18	53	29	0	100
pumiceous	310	860	1250	49	31	25	30	57	60	100	37	18	30	14	2	100
						100	100	100	100	100						

<sup>1</sup> average of three minimum density blocks

<sup>2</sup> average of three maximum density blocks

<sup>3</sup> only one of the collected samples was fb dense

**Table 3.3** Parameters for representative samples.

	Block	Description	Density (kg/m <sup>3</sup> )	Crystallinity (%)	Ves. (%)	N <sub>A total</sub> (cm <sup>-2</sup> )	N <sub>V total</sub> (cm <sup>-3</sup> )	N <sup>m</sup> <sub>V total</sub> (cm <sup>-3</sup> )	<i>n</i> no./cm <sup>3</sup> /cm	Size Range (μm)	Median (μm)	no. included
LP	K2022D		310	16	87.3	1.5E+06	1.2E+08	4.9E+08	5.1E+11	8-2504	68	2558
	Pum03-12	pumiceous	670		72.5							
MP	K2022G	dacite	840	19	65.8	2.3E+06	3.4E+08	8.0E+08	2.8E+12	4-2504	84	1774
HP	K2022B	blocks	1060	24	56.6	1.5E+06	1.1E+08	2.6E+08	4.2E+11	8-1989	45	2780
	Pum03-19		1220		50.1							
T	Pum03-57	transitional	1690	98*	31.2							
D1	dd03-37	dense dacite	2040	33	16.7							
D2	K2023A	blocks	2240	100*	8.6							
R1	K2628	Novarupta	1490	3	38.1	8.6E+05	5.9E+07	1.0E+08	2.4E+11	8-630	92	1695
R2	Rdome03-28	rhyolite	1740	6	27.3							
R3	Rdome03-19	dome	1970	5	17.7							

Blocks were chosen for vesicle quantification to span the densities measured per lithology. Vesicle shapes in higher density clasts (>1600 kg/m<sup>3</sup>) prevent vesicle volume calculations. DRE values of 2350 and 2450 kg/m<sup>3</sup> were used to calculate vesicularities for rhyolites and dacites, respectively. N<sub>A total</sub> is areal number density of vesicles; N<sub>V total</sub> is volumetric number density of vesicles referenced to the whole clast; N<sup>m</sup><sub>V total</sub> is volumetric number density of vesicles referenced to the melt only; *n* is population number density.

\*An approximate value; microlites are abundant.

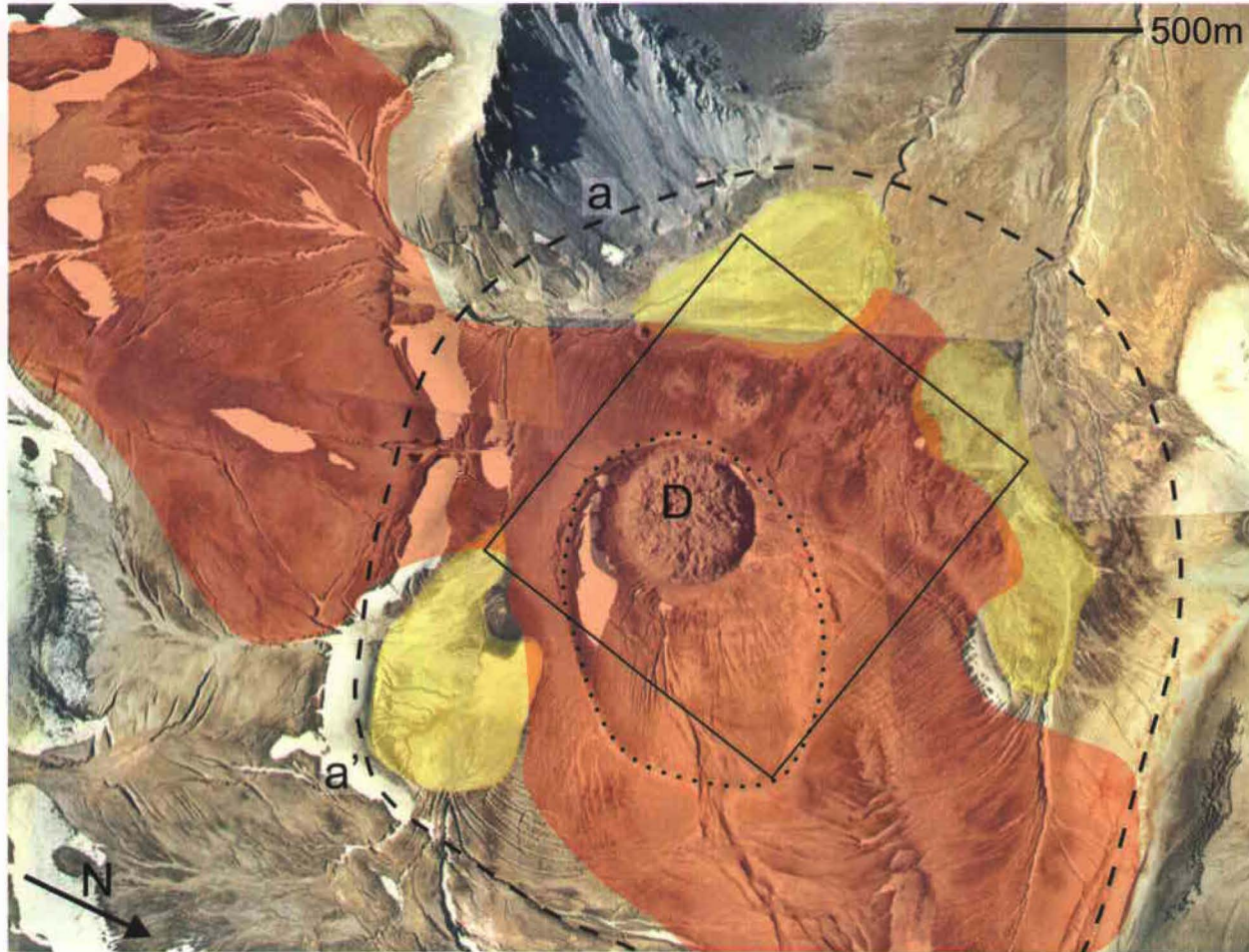


**Figure 3.1** Aerial photo mosaic of Novarupta vent region. Ejecta ring delineated by dotted line; crater rim traced by dashed line. Features include current dome (D), alluvial fans (yellow), and steep crater wall (a-a'). Area covered by block bed and mapped is highlighted in red. Rectangular region is enlarged in Figure 3.4.



**Figure 3.2**  
 Approximately 700 blocks were mapped for this study. a) Outsized and often broken blocks lie directly on fine ash; Epidsode V dome in background (D). b) Many blocks broke upon impact but the pieces fit together like a puzzle. c) Comminution of some blocks was too severe for reconstruction; dispersal boundary of individual block pieces marked by yellow line. d) Pile method, used when blocks were too broken to reconstruct along original dimensions (as in c), was assessed in the laboratory for error.



**Figure 3.3**  
Blocks showed a range of lithologies and surface textures. a) Pumiceous dacite block characterized by coarse vesicles. b) Breadcrusted breccia block. c) The original dimensions of this highly fractured, bread-crust dense dacite block remain discernable after impact. d) Mixed flow-banded block of pumiceous and dense dacite.

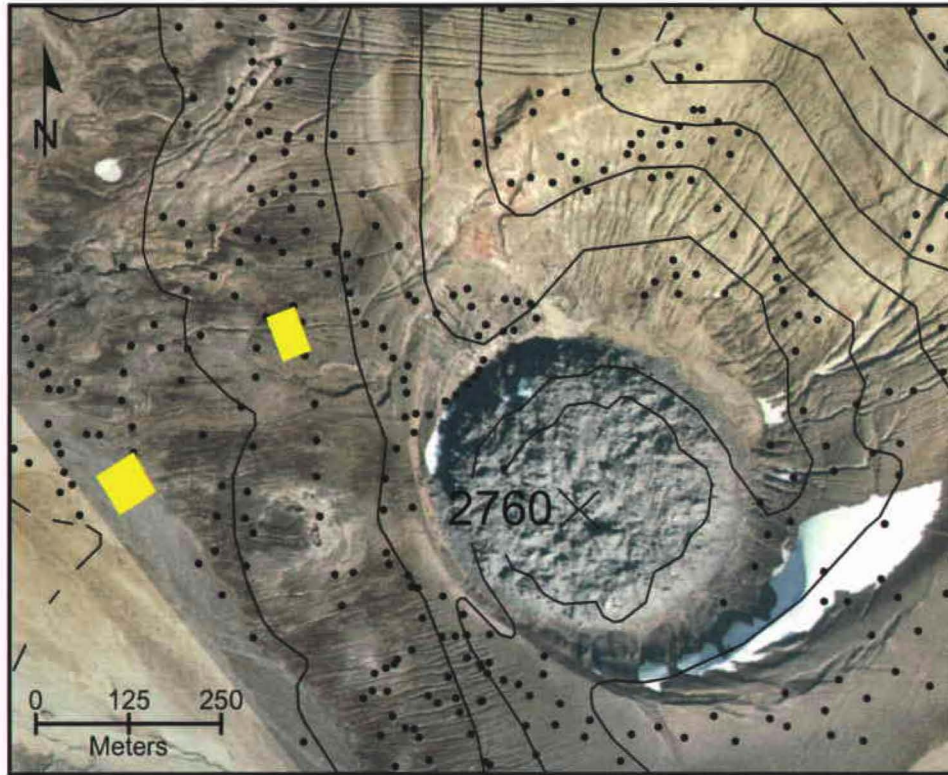


**Figure 3.4** Topographic contours (interval = 100 ft.) superimposed on aerial photos of the Novarupta dome region (enlarged delineated region on Figure 3.1). Black dots mark positions of mapped blocks. The 60x40 m and 60x60 m areas used for the componentry studies are shown in yellow.

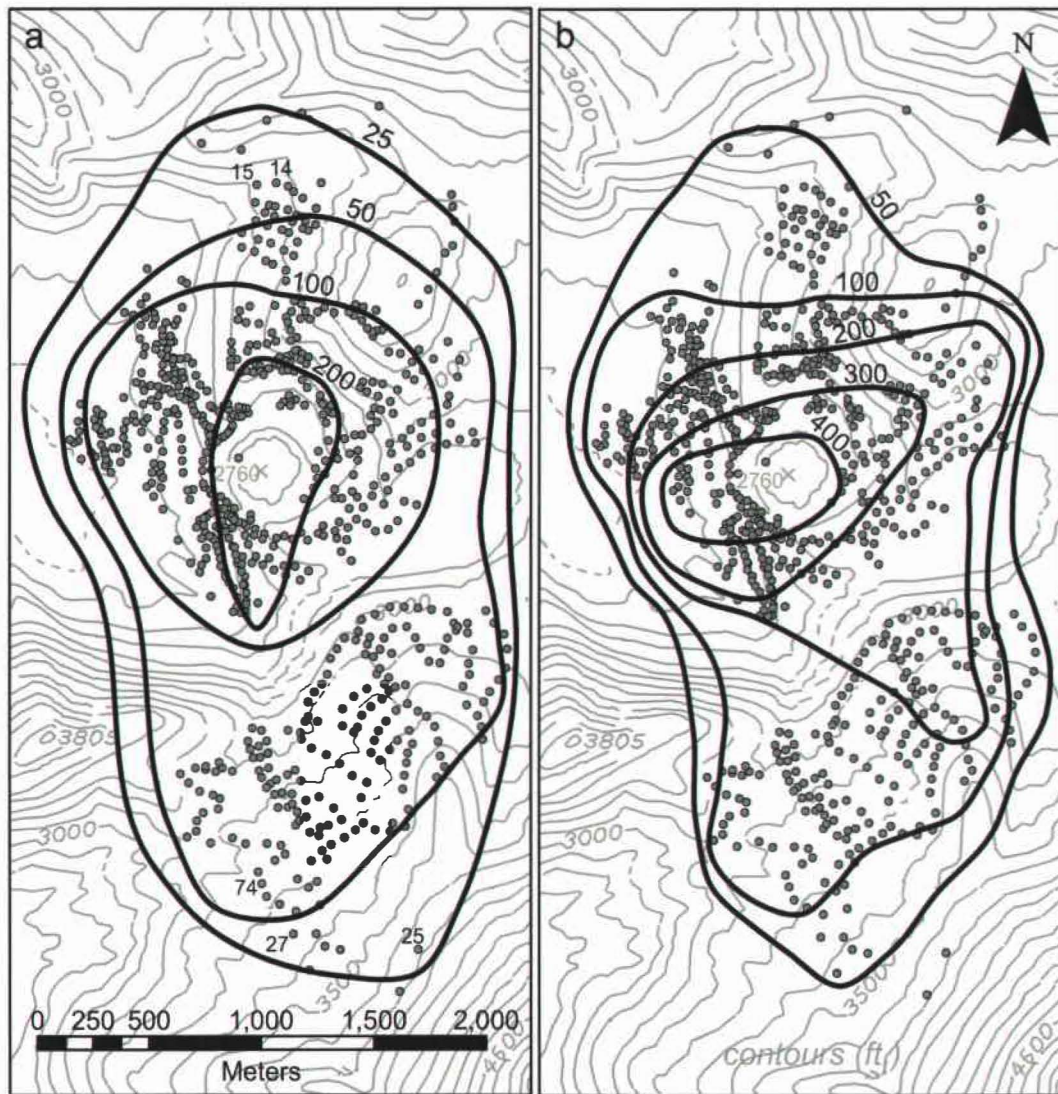


**Figure 3.5** Distribution of block size by a) average dimension (cm) and b) average dimension times density ( $\text{g}/\text{cm}^2$ ). On both maps, isopleths enclose the current dome and define a N-S dispersal axis, but when density is considered (b), NE and SE spurs are defined. Numbered blocks are referred to in the text.

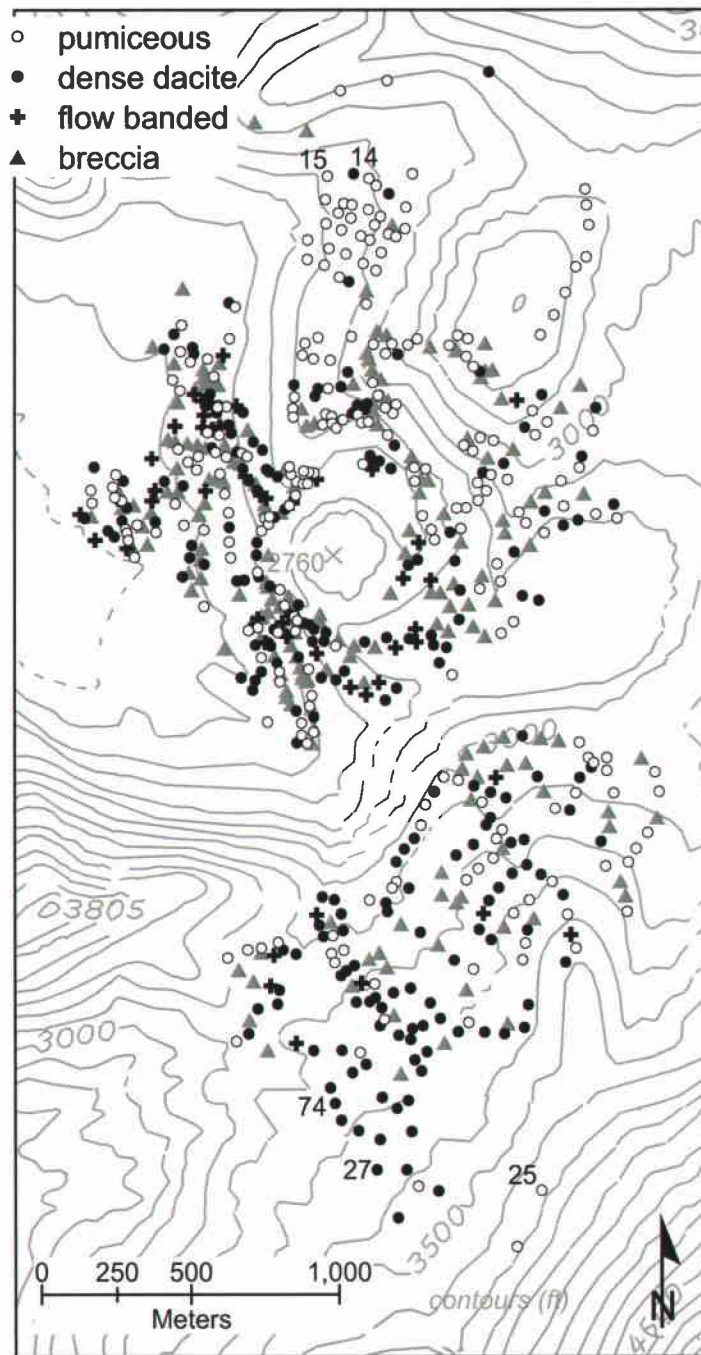


**Figure 3.6** Distribution of block lithologies. The average dimension (cm) for five blocks referred to in the text is also shown.

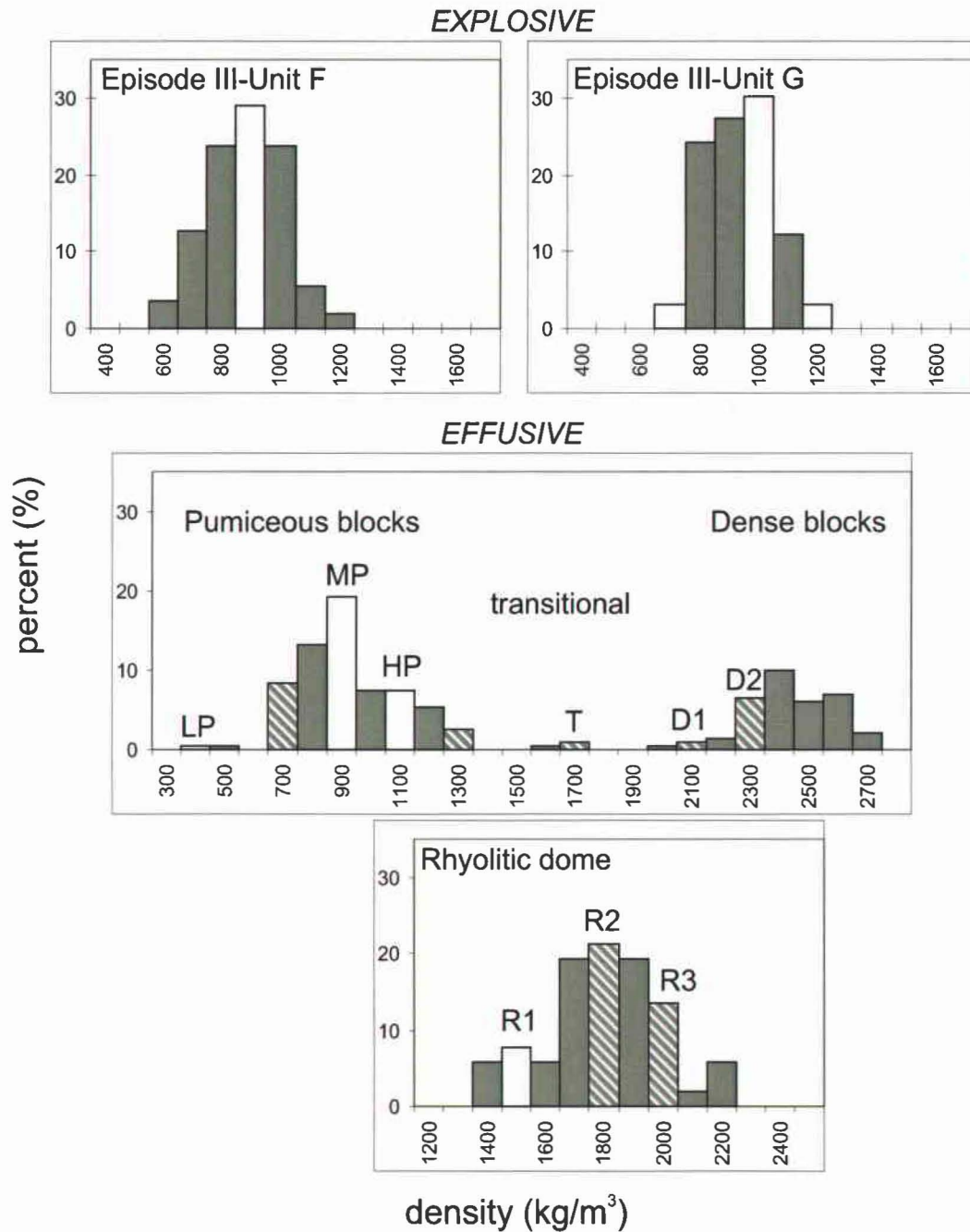


**Figure 3.7** Density distributions measured in samples from Plinian Episode III, the block bed, and the rhyolitic Episode V dome. Densities highlighted in white correspond to individual clasts selected for image analysis; stripes indicate clasts in which images were collected but not quantified. LP, MP, and HP are low ( $310 \text{ kg/m}^3$ ), modal ( $840 \text{ kg/m}^3$ ), and high ( $1060 \text{ kg/m}^3$ ) density pumiceous blocks; T is transitional between pumiceous and dense ( $1690 \text{ kg/m}^3$ ); D1 and D2 have measured densities of  $2040 \text{ kg/m}^3$  and  $2240 \text{ kg/m}^3$ ; R1, R2, and R3 from the Episode V dome have increasing densities of  $1490 \text{ kg/m}^3$ ,  $1740 \text{ kg/m}^3$ , and  $1970 \text{ kg/m}^3$ .

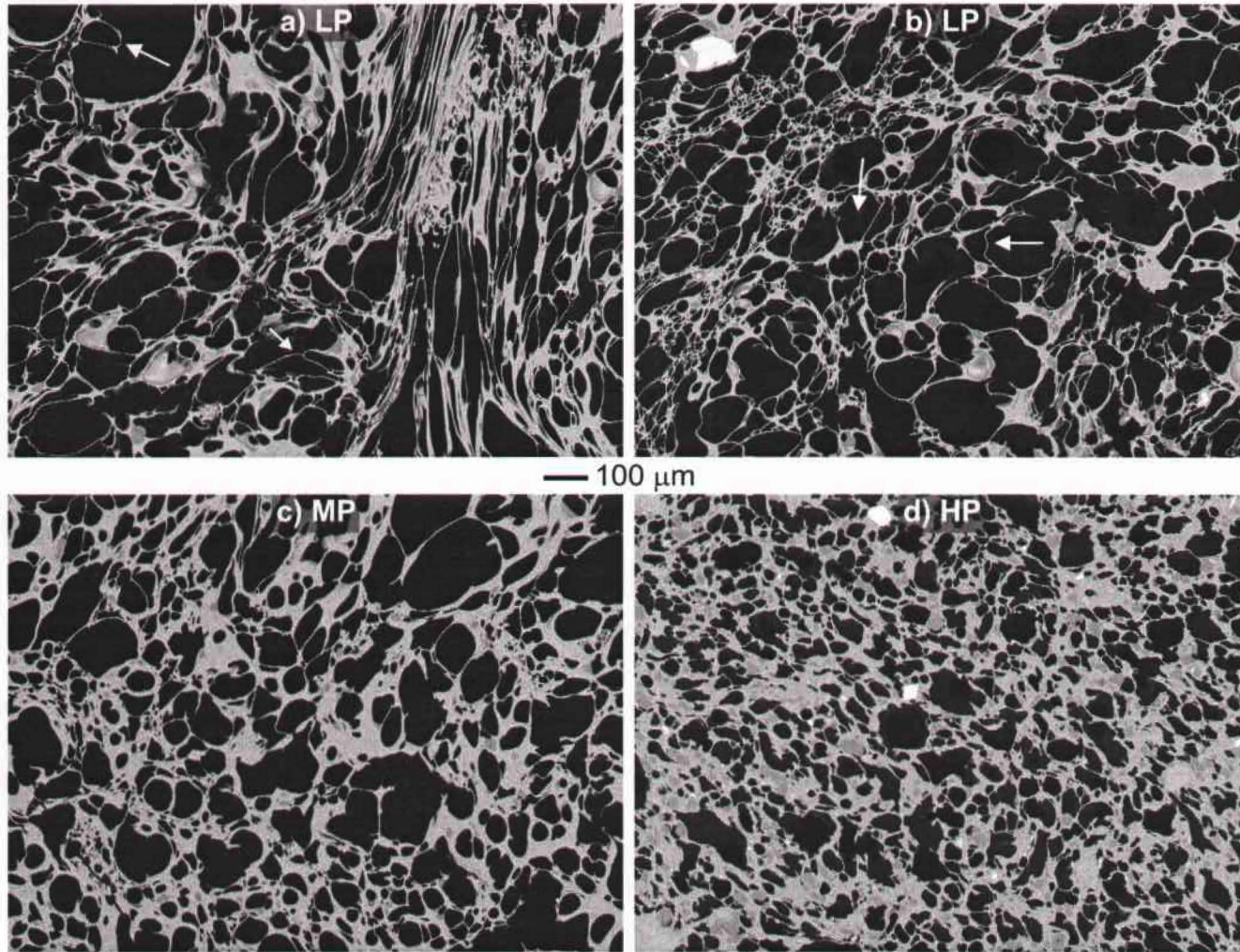


**Figure 3.8** BSE images at the same scale for low (a and b), modal (c), and high (d) density pumiceous blocks (LP, MP, and HP, respectively). Arrows point to coalescence features such as very thin bubble walls, wrinkled walls, and smaller bubbles expanding into larger bubbles.

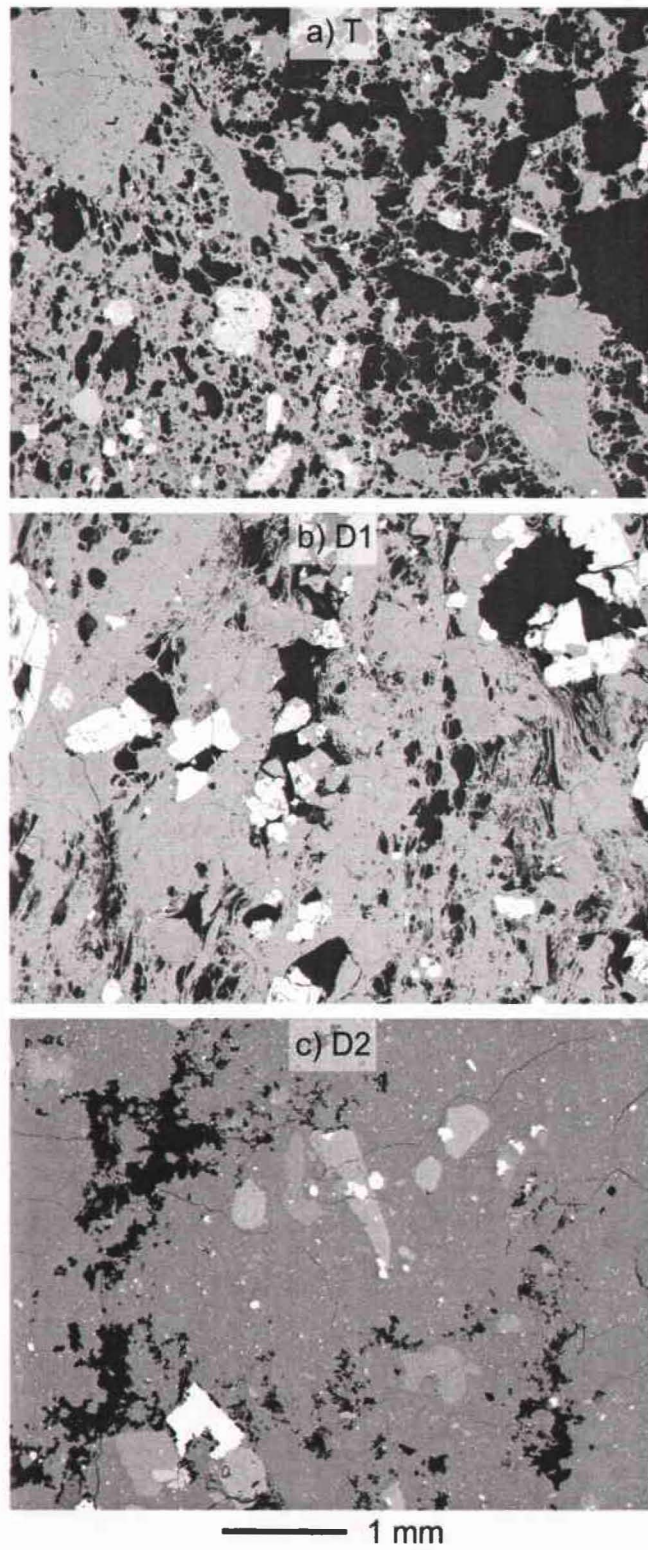
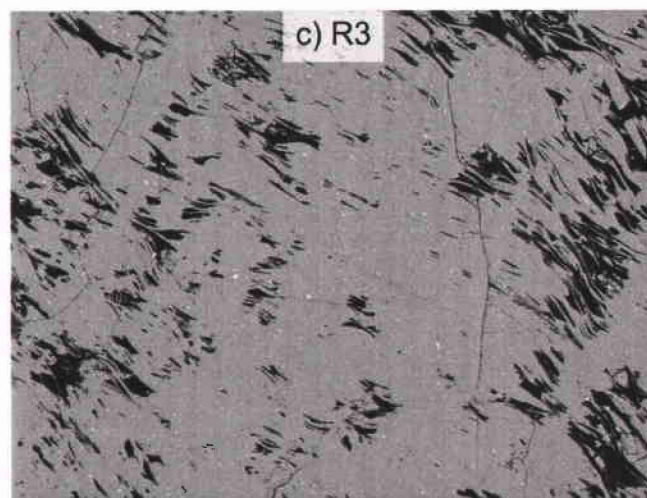
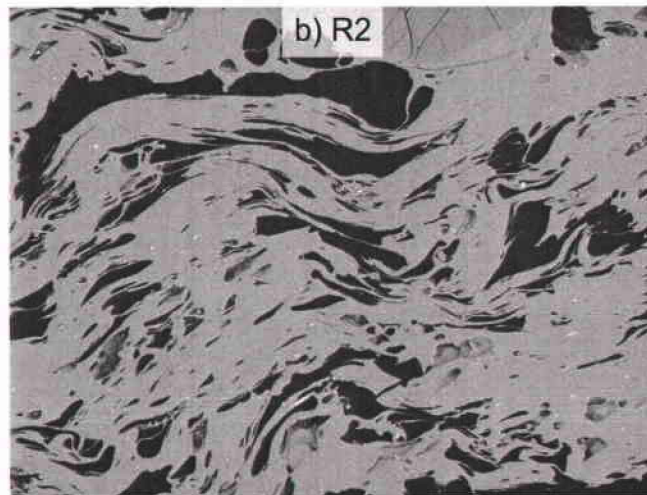
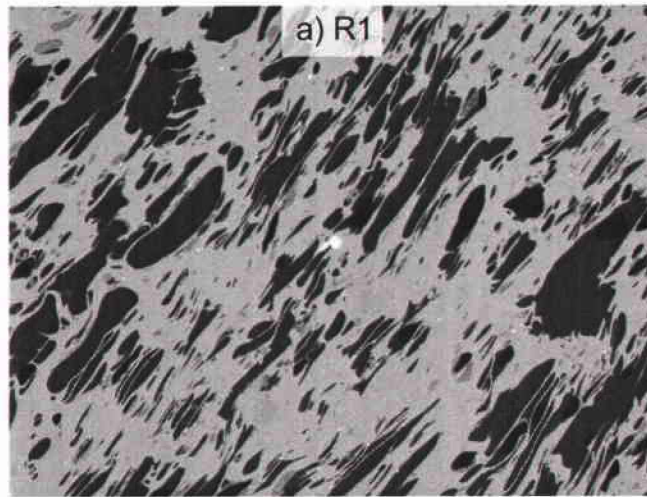


**Figure 3.9** BSE images of transitional (a) and dense dacites (b, c).



— 100  $\mu\text{m}$

**Figure 3.10** BSE images of rhyolitic Episode V dome. Notice the increase in microfractures as density increases.

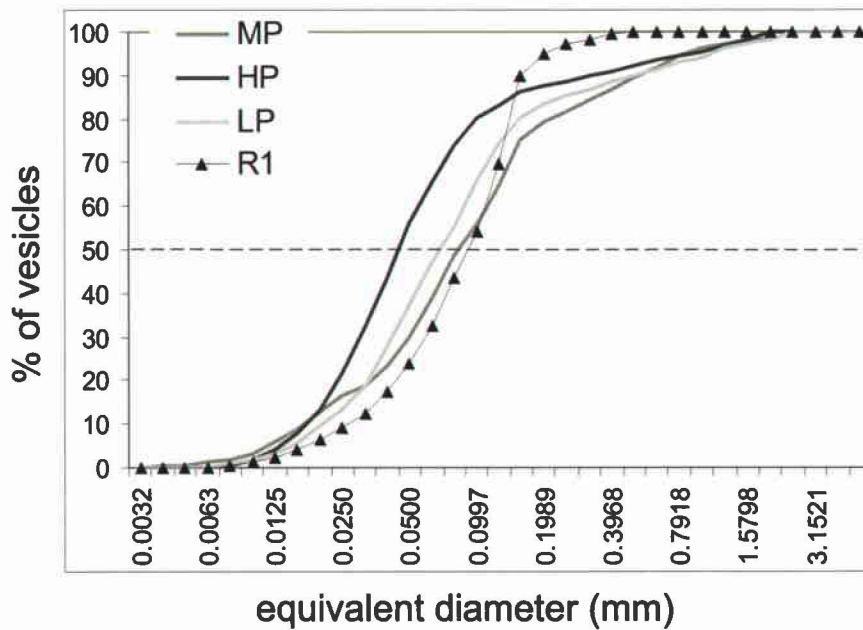
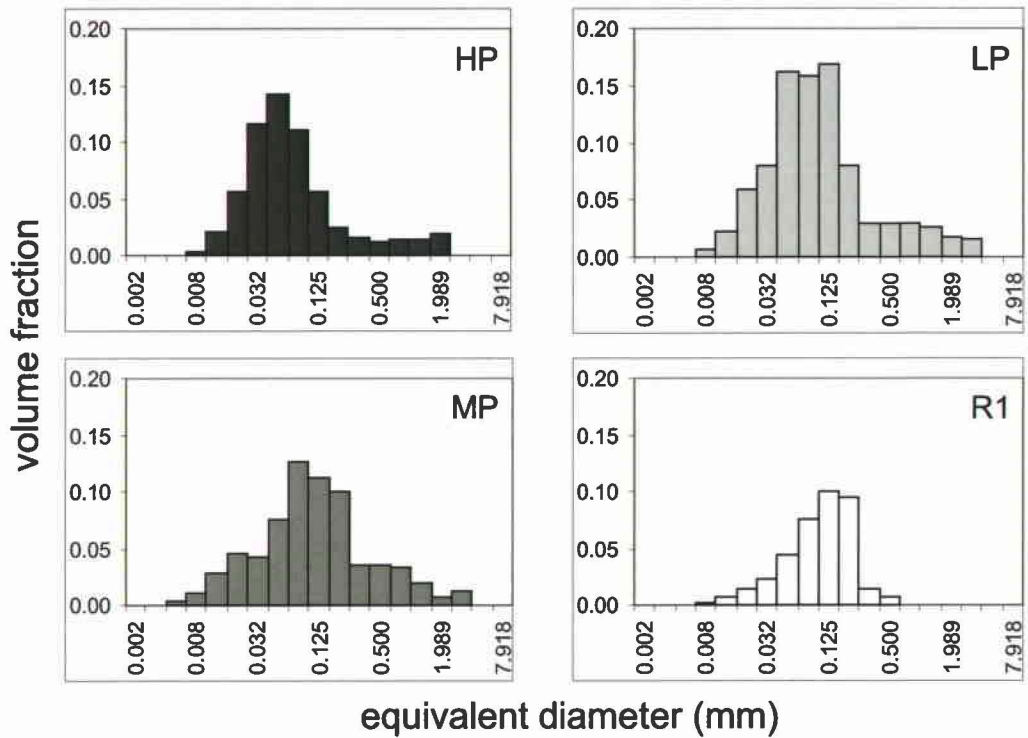


**Figure 3.11** Distributions of vesicle volume for HP, MP, LP, and R1. Top: Histograms showing the distribution of volume fraction against vesicle size. Bottom: Cumulative volume percent plot; intersection of 50th percentile with curves gives median vesicle sizes.

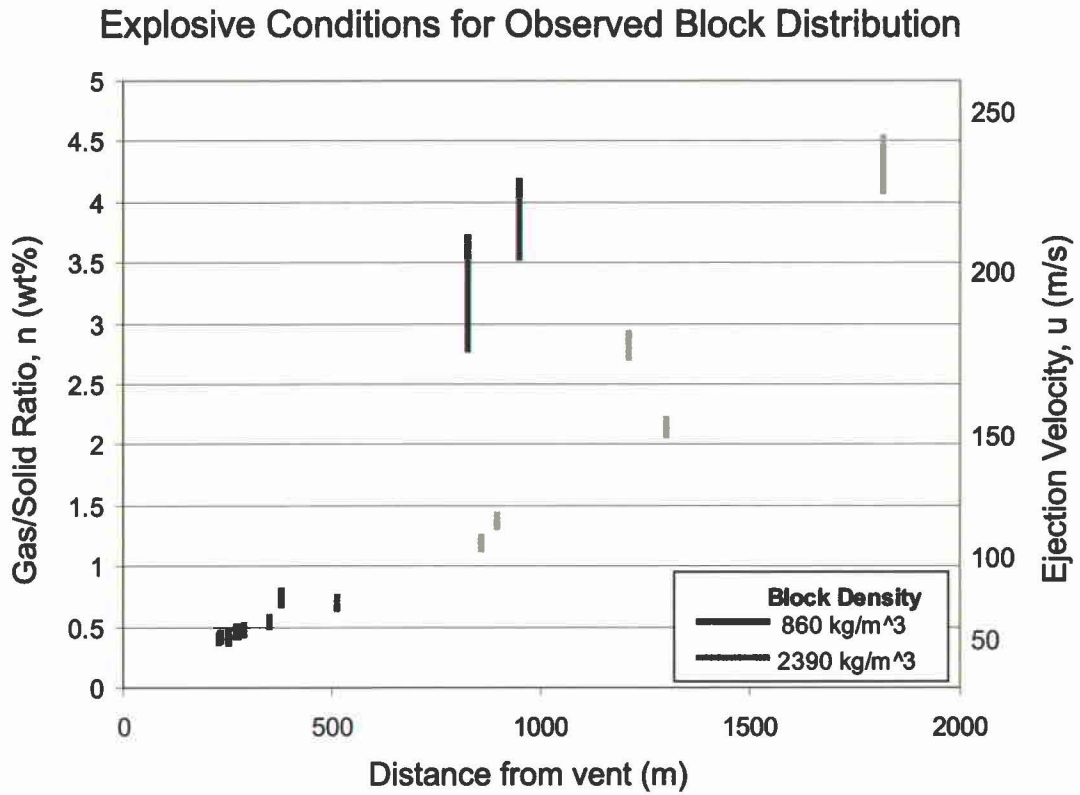


**Figure 3.12** Model results showing relationship between relative amount of gas and velocities needed to disperse blocks of a given size and distance.

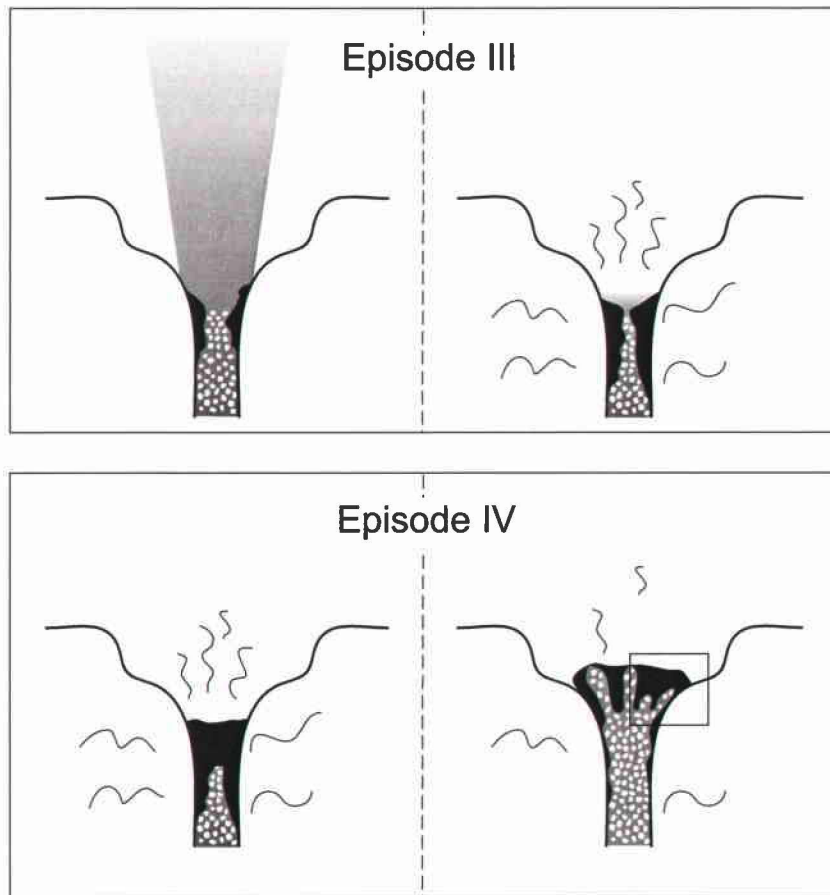


**Figure 3.13** Cartoon illustrating shifts in eruption style and degassing during episodes III and IV. As open-system degassing intensified, magma and gas decoupled and gas escaped freely marking the end of Plinian activity and Episode III. Degassed, dense magma accumulated on the conduit walls; the dense magma eventually capped the vent and was ultimately extruded by gas-rich dacite still ascending. Bubble collapse removed pathways for gas to escape, gas exsolution exceeded the capacity of the system to passively degas, and Vulcanian eruptions ensued. Rectangular region in last panel is enlarged in Figure 3.14.

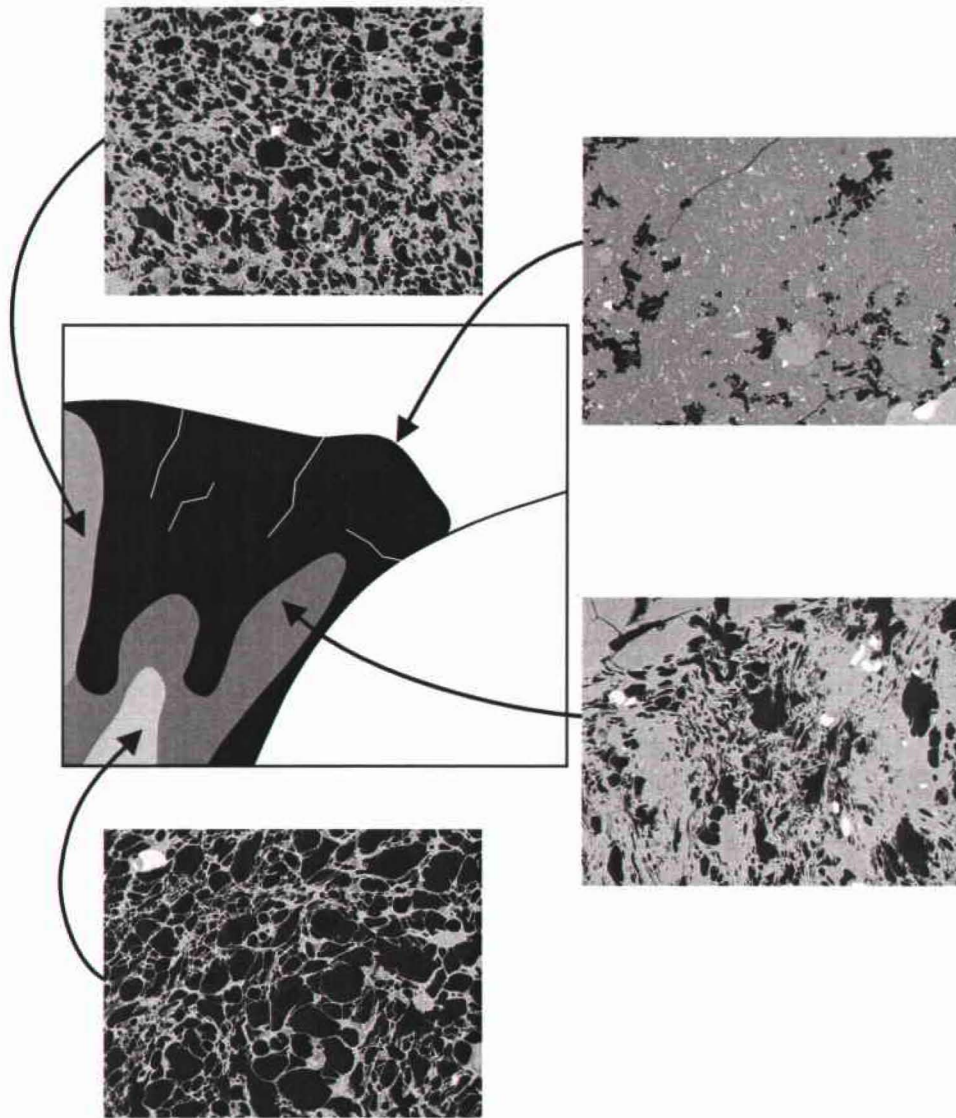


**Figure 3.14** Enlarged region on Figure 3.13. Heterogeneity in the Episode IV melt effected the outcome, i.e., disruption, compared to the stability of the Episode V dome.

## CHAPTER 4

### **Episode I: variations in vesiculation with changes in vent geometry and eruptive composition**

#### **4.1 Abstract**

Three episodes of powerful explosive activity occurred during the 1912 eruption of Novarupta, Alaska, USA before a switch to effusive dome growth. The second and third of these, episodes II and III, were classical plinian events characterized by a stable plume and generating a succession dominated by fall deposits of chemically homogeneous dacitic pumice. Episode I shows two striking contrasts to this behavior. First, two chemically distinctive magmas, rhyolite and dacite-andesite, were erupted in steadily changing proportions. Second, the eruption simultaneously generated large volumes of both ignimbrite and Plinian fall. This paper explores the form and underlying causes of the changes in eruptive behavior during Episode I via textural analysis of pyroclasts.

Plinian fall Layer A of Episode I was purely rhyolitic and was followed by a rapid decline in rhyolite abundance and concomitant increase in dacite in Layer B. Episode I products have been extensively sampled at two key sites; ranges in bulk density are consistently narrower for the erupted rhyolite than for the coeval dacite. Mean vesicularities of the rhyolitic pumice are remarkably consistent throughout layers A and B. The density range, however, shows an interesting trend, being initially wide before narrowing and flaring again at the end of phase A. In contrast, vesicularity means, minima, and maxima in dacite pumices all progressively narrow with time through phase

B. Vesicle volume distributions (VVDs) and cumulative number densities indicate continuous bubble nucleation and growth were strongly overprinted by bubble coalescence in both melts. As in the later Plinian episodes, these observations are consistent with closed-system disequilibrium degassing during Episode I, but a complex ascent history involving first rhyolite as the conduit became established and then dacite seeking to displace the rhyolite resulted in a wide range of vesicularities in samples from lower Layer A and Layer B.

## **4.2 Introduction**

### **4.2.1 Magma ascent and degassing**

The history of magma ascent and degassing in the conduit during an explosive eruption is recorded in the textures of the eruption products. The significance of vesiculation processes such as bubble nucleation, growth, coalescence, and collapse can be constrained by studying vesicle size and volume distributions (VSDs and VVDs), vesicle shapes, and glass wall thicknesses (Cashman and Mangan 1994; Klug et al. 2002; Gurioli et al. 2004). By understanding the interplay between these processes, the influence of style, timing, and extent of magma degassing on eruption dynamics can be discerned (Mangan et al. 1993; Cashman and Mangan 1994; Mangan and Cashman 1996). Furthermore, eruption dynamics and thereby magma ascent and degassing are intimately linked to external factors such as vent and conduit geometry (Macedonio et al. 1994; Papale 1998). This linkage generates a feedback between vesiculation/degassing and the evolving vent-conduit structure, i.e., changes in one produces changes in the

other. Thus, on a broader scale, textures provide insights into the development of the volcanic plumbing system and the connection between parameters both internal, e.g., rheology and volatile content, and external, e.g., conduit diameter and vent structure, to the magma.

Previous studies of silicic eruptions have examined the textures of pyroclasts in contrasting deposit types. Klug et al. (2002) studied flow versus fall deposits, and others concentrated on ejecta with different crystallinities, e.g. Klug and Cashman (1994), Polacci et al. (2001), Gurioli et al. (2004) studied white and gray pumice from Mount St. Helens 1980, Pinatubo 1991, and Vesuvius 79, respectively. All of these studies have focused on differences in vesiculation accompanying abrupt transitions during the course of an eruption. Abrupt transitions during the Novarupta 1912 eruption have likewise been considered in the previous chapters of this dissertation. Of the five episodes that comprised this eruption, only Episode I was characterized by a progressive transition in both emplacement style and in the dominant composition of erupting material (Hildreth 1983; Hildreth 1991; Fierstein and Hildreth 1992). During this opening episode, a sustained Plinian column coincided with ignimbrite generation. Volumetrically a shift occurred in the dominance of fall versus flow with flow becoming more significant with time. Superimposed on this shift in the dominant emplacement style was a shift in the dominant composition of ejecta, moving from rhyolite to dacite.

#### **4.2.2 Goals**

This study has three main goals. The first is to constrain the conditions of magma ascent and vesiculation during Episode I when two melt types were erupted

simultaneously from the vent system. Does one composition affect the ascent and vesiculation history of the other, or do the two melts simply share the conduit but effectively do not see one another? Establishing the influence of vent/conduit opening and evolution on magma degassing is the second objective. Questions to this end include (i) are the changing stresses in the shallow conduit from eruption initiation to peak mass eruption rate (MER) imprinted in the textures of the eruption products, and (ii) how intimately are changes in vent geometry, mass flux, emplacement style, and magma degassing linked? The third aim of this study is to contrast ascent and vesiculation processes during Episode I with the more simple Plinian episodes II-III that followed. Here we have an opportunity to contrast melt fragmenting to form a stable Plinian plume with that generating coeval fall and voluminous ignimbrite; do textures in the pyroclasts reflect the much higher discharge rates implicit in Episode I with respect to episodes II and III? To address these issues, we use microtextures of dacite and rhyolite pumice from this opening episode to understand changing eruption dynamics.

## **4.3 Previous work**

### **4.3.1 Eruptive sequence**

The 1912 eruption of Novarupta began on 6 June and over the ensuing 60 hours progressed through three explosive episodes. Episode I was perhaps the most complex in terms of composition and emplacement style. Superimposed over two phases of fall deposition (resulting in layers A and B) plus coeval ignimbrite emplacement was a major

shift in the composition of the magma (Hildreth 1983; Hildreth 1991; Fierstein and Hildreth 1992).

Layer A, the first of the Episode I fall deposits, is a rhyolite fall unit containing as much as 24 wt% lithics, making it the most lithic-rich of all the 1912 fall deposits (Fierstein and Hildreth 1992). Layer B overlies A and is defined only by the onset of a dacite and andesite contribution to the ejecta and not by a significant time-break (Fig. 4.1); the deposition of layers A and B during Episode I was continuous. Layer B becomes more dacite (and andesite) rich as the episode continued, from >98% rhyolite at its base to only ~10% rhyolite at its top (Hildreth 1991). It can be divided into three subunits on the basis of composition and grain size. B<sub>1</sub> has 82-99% rhyolite, B<sub>2</sub> has 51-93% rhyolite in its lower half and 40% rhyolite in its top, and B<sub>3</sub> has 20-38% rhyolite at its base and only 11-25% rhyolite at its top (Fig. 4.2) (Fierstein and Hildreth 1992).

More than 98% of the total  $11 \pm 3 \text{ km}^3$  of 1912 ignimbrite was emplaced during Episode I (Hildreth and Fierstein 2000). The main Valley of Ten Thousand Smokes (VTTS) ignimbrite is a composite deposit of at least one major and several minor flow units all emplaced during Episode I (Fierstein and Hildreth 1992). Pumice in the early flows were predominantly rhyolite, and like the Episode I fall deposits, dacite and andesite proportions increase in successive flows. The ignimbrite sequence began with relatively small volume ( $0.5\text{-}1.0 \text{ km}^3$ ) all-rhyolite flows that are interbedded with fall Layer A (Fig. 4.2) (Fierstein and Hildreth 1992). Another small flow followed that was contemporaneous and compositionally equivalent to subunit B<sub>1</sub>, but the largest flows ( $\sim 10 \text{ km}^3$ ) are correlative with B<sub>2</sub> (Figs. 4.1, 4.2). The final small volume flows are

andesite-rich with no fall equivalents; they were deposited after the Plinian column had decayed. Thus, most of the ignimbrite sequence in the VTTS is contemporaneous with fall layers A-B (Fig. 4.2). As the amount of dacite and andesite ejecta increased through B<sub>2</sub> time, the volumetric rate of ignimbrite production increased while fall deposition decreased; 90 vol% of Layer A was comprised of fallout whereas 80 vol% of Layer B was accounted for by ignimbrite (Fierstein and Hildreth 1992).

#### **4.3.2 Vent structure**

Adding to the complexity of Episode I was the development of a 2-km wide crater at Novarupta and compensatory collapse of the 5.5 km<sup>3</sup> Katmai caldera 10 km east (Hildreth 1983; Hildreth 1991; Fierstein and Hildreth 1992). Before the eruption of the rhyolitic phase A magma through Jurassic sedimentary rocks of the Naknek Formation, no vent existed at Novarupta. The vent thus opened and became established during the initial period of the eruption. Episode I stratigraphy suggests this vent simultaneously supported two eruption styles, Plinian and ignimbrite-forming, and therefore probably enlarged and evolved in a complex fashion. The final expression of the vent during Episode I was a 2-km wide crater that truncates Falling, Baked, and Broken Mountains (Fig. 4.3). This crater was largely infilled by moderately to densely welded vitrophyres by the close of Episode I. Subsequent episodes erupted through a narrower inner vent established through the vitrophyre fill at a site close to the center of the Episode I crater. This vent is now filled by the current rhyolitic Novarupta dome. Episodes II and III were predominantly characterized by fall deposits which in turn mantled and filled the structural depression created during Episode I. As the eruption progressed, concentric

step-faulting, slumping, and subsidence also occurred around the vent and in part created the arcuate fractures present today (Hildreth 1987; Fierstein and Hildreth 1992).

In the Novarupta area, local basement comprised of sandstones and siltstones of the Naknek Formation extends to a depth of ~1500 m. Because the 1912 sedimentary lithic clasts are all from the Naknek, the vent was thus excavated to a depth no greater than 1500 m (Hildreth 1987). As previously stated, Plinian fall Layer A is the most lithic rich fall layer. This enrichment is the result of the initial opening of the conduit and reaming of the vent.

#### **4.4 Current study**

##### **4.4.1 Methods**

As for the Episode II and III dacites (Chapter 2), samples of Layer A rhyolitic pumices and Layer B rhyolitic and dacitic pumices were collected at two key sections, 89-1 and 95-7 (Fig. 4.4). Episode I fallout is strongly directed to the SE and confined to a 90° sector extending from the vent. Site 95-7, ~6 km from the vent, was originally sampled in 1995. Most deposits within the first 8 km from vent, however, are poorly preserved. The steep terrain in this dispersal sector favored rapid remobilization of tephra, as did the abundance of snow in June (Hildreth 1987). To complement the samples collected at 95-7, a much more complete section at site 89-1 at 13 km from the vent was sampled during subsequent fieldwork in 2003. Sampling spanned layers A and B with special attention to the transitions between A, B<sub>1</sub>, B<sub>2</sub>, and B<sub>3</sub> (Fig. 4.5). Following Houghton and Wilson (1989), the density of each clast within the collected samples was

measured and vesicularity was calculated using a dense rock equivalent (DRE) density of  $2350 \text{ kg/m}^3$  for the rhyolites and  $2450 \text{ kg/m}^3$  for the dacites (Spera 2000).

Based on the bulk density data, individual clasts were selected to study the textural changes through Episode I in thin section. To accurately assess the complete range and distribution of all bubble sizes present in the Episode I clasts, images at four magnifications were captured using a flatbed scanner and a scanning electron microscope (SEM) and analyzed according to the methods described in Chapter 2. The clasts from both sites were studied, and vesicle size and volume distributions (VSDs, VVDs) were determined for four clasts from 95-7. Vesicle areas were binned by size and converted to area ( $N_A$ ) and volume ( $N_V$ ) number densities following the method of Sahagian and Proussevitch (1998). The cumulative number density ( $N_{V \text{ total}}$ ) referenced to the matrix of the clast, i.e., total clast volume less the phenocrysts, was determined by summing the number density for each bin size ( $N_V$ ). Cumulative number densities referenced to the melt volume ( $N_{V \text{ total}}^m$ ) were also determined. Whereas  $N_{V \text{ total}}$  is the cumulative number density of vesicles based on the entire clast volume including the vesicles themselves,  $N_{V \text{ total}}^m$  excludes the vesicle volume portion of the whole clast volume and thereby is referenced to the glass alone (Klug et al. 2002).

#### **4.4.2 Density and bulk vesicularity**

The 89-1 samples clearly show temporal trends in the densities of the fallout pumices that we link in later sections to shifts in ascent and eruption dynamics (Fig. 4.6).

**Layer A:** Samples of rhyolitic pumice from Layer A show a distinctive trend. The earliest samples have comparatively wide ranges of density/vesicularity. Range narrows

sharply, however, with increasing stratigraphic height because the maximum density decreases from c. 1200 to 900 kg/m<sup>3</sup>. The mean and minimum densities remain relatively constant at 700 kg/m<sup>3</sup> and 500 kg/m<sup>3</sup>, respectively. In the upper third of Layer A the trend of decreasing max density abruptly reverses, and both mean and maximum density increase up section as the contact with Layer B is approached (Fig. 4.6).

**Layer B:** The rhyolite samples across Layer B show relatively uniform densities and have much narrower density ranges (~400 – 1100 kg/m<sup>3</sup>) than coeval dacites of Layer B (~400 – 2000 kg/m<sup>3</sup>). Rhyolites from B<sub>3</sub> show maxima that are uniform and lower than those of the underlying units (Fig. 4.6). Dacite first appears in B<sub>1</sub>, and the stratigraphically lowest dacite samples show very wide density/vesicularity ranges (500 – 2000 kg/m<sup>3</sup>). In the entire eruption, this range is only matched by the Episode IV block bed which is inferred to have formed by disruption of a lava dome or plug (Chapter 3). Mean, minimum, and maximum densities of the dacitic clasts all decrease from the bottom of B<sub>1</sub> to the top of B<sub>3</sub>, and the trend is most marked in the dense clasts (Fig. 4.6). Mean densities of rhyolite and dacite from B<sub>2</sub> and B<sub>3</sub> begin to converge (at ~710 kg/m<sup>3</sup>) around the transition between B<sub>2</sub> and B<sub>3</sub>, and the values of dacitic clasts from the top of B<sub>3</sub> are actually slightly lower (670 kg/m<sup>3</sup>) than their rhyolite counterparts (710 kg/m<sup>3</sup>).

**Comparison with episodes II and III:** The trends described above and illustrated in Figure 4.6 are not seen in samples from the later Plinian episodes (Fig. 4.7). The very high maximum densities encountered in Episode I deposits are also absent in those of episodes II and III. Instead, density and vesicularity remain constant throughout Episode II. During Episode III the maximum and mean densities progressively increase, but the

density/vesicularity range never reaches that seen in the earliest dacite pumice from Layer B.

#### 4.4.3 Qualitative observations

Clasts representing the high, modal, and low densities for dacite (Layer B) and rhyolite (layers A and B) in the samples from both sites were used in this study. Scans were made of thin sections from pumices from Layer A and from subunits B<sub>1</sub>, B<sub>2</sub>, and B<sub>3</sub>. High magnification backscatter electron (BSE) images were also collected for modal density clasts from layers A, B and C from site 95-7 (Fig. 4.8).

The most significant textural changes in pumice erupted during Episode I are seen in the size, distribution, and shape of large bubbles in both rhyolites and dacites (Figs. 4.9, 4.10). Bubbles in rhyolite clasts from the base of Layer A are stretched, forming fabrics (Fig. 4.9). This elongation in bubble shape is most apparent in 0.5 to 2.5 mm vesicles. No noticeably elongated fabrics are recorded in rhyolites from upper Layer A and Layer B. In these sections, bubbles are much more equant. In all Layer A clasts, large bubbles often form clusters separated by thin glass walls. Such clusters are less conspicuous in the Layer B rhyolites, but the largest vesicles have complex, amoeboid shapes.

Vesicle textures in dacite pumices from B<sub>1</sub> are similar to their rhyolitic analogs. While the populations of large bubbles in B<sub>1</sub> and B<sub>2</sub> rhyolites appear to be similar, large bubbles in B<sub>2</sub> dacites are quite distinct compared with their B<sub>1</sub> counterparts. B<sub>2</sub> dacitic pumices are characterized by regions with very large bubbles (2-5 mm diameter) forming distinct bubble trains (Fig. 4.10). The B<sub>3</sub> dacites also have a significant

population of large bubbles (2-4 mm) distributed homogeneously throughout each clast making them the most vesicular dacites of Episode I (Fig. 4.10).

The thickness of the glass walls separating the bubbles is generally thin (~10-25  $\mu\text{m}$ ) for both the dacites and the rhyolites of Episode I. The clusters of large, elongate bubbles in the rhyolites from Layer A (Fig. 4.11) have very thin walls (~5  $\mu\text{m}$ ) while regions of small-intermediate bubbles (25-125  $\mu\text{m}$  diameter) are ubiquitously interspersed and are associated with thicker glass walls (~50  $\mu\text{m}$ ). In rhyolite and dacite pumices from Layer B the range of wall thicknesses is slightly decreased (~5-30  $\mu\text{m}$ ) compared to Layer A rhyolites with the majority in the 15-30  $\mu\text{m}$  size range (Fig. 4.11).

Coalescence features, like the ones described in Chapter 2, e.g. wrinkling, rupture, are abundant in all Episode I pumices (Fig. 4.11). Wrinkling of the very thin walls (~5  $\mu\text{m}$ ) around the larger bubbles in all clasts is commonly seen. Thin walls (5-10  $\mu\text{m}$ ) between two equally sized bubbles resulting from approximately equal pressures exerted on either side are common in all bubble size ranges. Remnants of walls after rupture has occurred as the bubbles merge are also plentiful. Finally, larger bubbles without elongation have mostly amoeboid rather than spherical shapes indicative of bubble-bubble interactions.

While mingling is most common between andesite-dacite and andesite-rhyolite compositions (Hildreth 1983; Fierstein and Hildreth 1992), dacite-rhyolite banded clasts were found in Layer B of Episode I. One such clast belonging to subunit B<sub>1</sub> was examined microscopically (Fig. 4.12), and overall, the textures of the alternating bands matched the all-dacite and all-rhyolite clasts. The general bubble size of the dacitic

component is slightly smaller, but otherwise no major differences were apparent in bubble textures between the two compositions.

#### **4.4.4 Vesicle size data for selected clasts**

**VSD and VVD:** Five clasts were selected for assessment of vesicle size and volume distributions (VSDs and VVDs). VVD histograms showing the volume fraction of vesicularity per vesicle diameter were used to evaluate the number of bubble populations, the dominant bubble size(s), and the total size range. Measured vesicle sizes reinforce the visual trends described qualitatively above. Three rhyolitic clasts were selected from the density/vesicularity modes (Fig. 4.8) of samples from layers A, B, and C, respectively. The Layer A rhyolite is not characterized by a unimodal distribution (Fig. 4.13); the volume fraction is distributed more evenly among sizes than for any previously studied Plinian pumice from the 1912 eruption (Chapter 2). In fact, this distribution might be described as slightly bimodal with a 315  $\mu\text{m}$  main peak and a smaller peak at 80  $\mu\text{m}$ , and its largest bubbles are in the 2 mm size range. The VVD of a Layer B rhyolite is skewed toward small-intermediate bubble sizes (30-80  $\mu\text{m}$ ) with a coarse tail extending to 3 mm (Fig. 4.13). As in Layer B, the rhyolitic pumice from Layer C is unimodal but its mode is at 200  $\mu\text{m}$ . Median vesicle sizes also record the shift in dominance from larger to smaller vesicles from Layer A to Layer B; the median vesicle size in the Layer A clast is 136  $\mu\text{m}$  and in B is 48-58  $\mu\text{m}$  (Table 4.1).

The single analyzed dacite from Layer B does not have a strongly unimodal distribution, particularly compared to pumice clasts from episodes II and III (Chapter 2). The VVD is skewed toward smaller bubble sizes and has a less distinct coarse tail, and its

largest bubbles are in the 2 mm size range versus the >3 mm bubbles in the Layer B rhyolite (Fig. 4.13).

**Vesicle number densities:** Variations in bubble nucleation and growth can also be discerned by comparing cumulative number densities ( $N_{Vtotal}$  or  $N_{Vtotal}^m$ ) between layers (and episodes) and from plots of number density ( $N_V$ ) versus size ( $L$ ). If nucleation dominates over growth, numerous small bubbles will comprise the volume fraction. Conversely, a short-lived nucleation event followed by prolonged growth might result in fewer bubbles of large size. While bulk vesicularity in the above mentioned cases might be equal, differences in the cumulative number densities ( $N_{Vtotal}$  or  $N_{Vtotal}^m$ ) would reflect the different processes. Consistent with the qualitative observations and the VVDs, both  $N_{Vtotal}$  and  $N_{Vtotal}^m$  values for the Layer A pumice are smaller than those of Layer B pumice. Also, the values for rhyolite and dacite clasts from Layer B are approximately equal (Table 4.1). Gaonac'h et al. (1996a; 1996b) and Blower et al. (2001a; 2001b) modeled power-law relationships on vesicle number versus size plots for bubble populations for simulations of continuous nucleation and steady-state growth. On a log-log plot, number density data for Episode I ejecta coincide with the data for the episodes II and III ejecta (Fig. 4.13). The data fit a linear trend with a slope of -3.8 for all except the smallest bubbles ( $\leq 30 \mu\text{m}$ , or  $L \leq 1.5$ ).

## 4.5 Interpretation

### 4.5.1 Vesiculation history of Episode I melts

From features indicative of bubble-bubble interactions, e.g., wall wrinkling to rupture, the signature of coalescence is apparent in the images of Episode I pumice (Fig. 4.11). Broad modes and distinct coarse tails on VVD histograms are also signs of syneruptive growth and coalescence on size distributions (Orsi et al. 1992; Klug and Cashman 1994; Gaonac'h et al. 1996a; Simakin et al. 1999; Blower et al. 2001a; Blower et al. 2002). When bubbles reach a certain size, growth occurs primarily through coalescence and creates broad modes. Outsized bubbles result from large bubbles interacting and create the coarse tails on the histograms. As for episodes II and III, the Episode I vesicle populations are described by such distributions (Figs. 4.13; also 2.11, 3.11).

Episode I pumices are also distinguished by an absence of microlites and high bubble number densities ( $10^7$ - $10^9$  cm<sup>-3</sup>). These high bubble number densities are reproduced in nucleation experiments on silicic magmas and in numerical modeling only under high degrees of supersaturation and disequilibrium degassing (Mourtada-Bonnefoi and Laporte 1999; Mangan and Sisson 2000; Mangan et al. 2004). By analog to these experimental results, both the rhyolite and dacite magmas experienced disequilibrium degassing. The absence of microlites further supports disequilibrium degassing and favors homogeneous nucleation. Delayed, disequilibrium degassing and high supersaturation pressures would also correspond to the high intensity and explosivity seen during the Novarupta 1912 eruption (Mangan et al. 2004).

Power law size distributions with exponents of  $\sim 3.8$  describe bubbles  $>30 \mu\text{m}$  on plots of Episode I cumulative number densities (Fig. 4.13). This power law exponent is higher than values determined by experimental simulations and modeling of continuous nucleation (Blower et al. 2001a; Blower et al. 2002) but is consistent with values achieved by modeling cascading coalescence (Gaonac'h et al. 1996a; Gaonac'h et al. 2004). In contrast, the exponential size distribution of bubbles  $\leq 30 \mu\text{m}$  best fits models of prolonged nucleation and growth by diffusion and decompression (Blower et al. 2001a; Blower et al. 2002; Klug et al. 2002). This population could result from nucleation just prior to quenching (insufficient time for growth and coalescence). Thus, nucleation was continuous, and once nucleated, bubbles grew by diffusion/decompression. However, when bubbles reached a critical size ( $30 \mu\text{m}$  for 1912 pumice), further growth was dominated by bubble coalescence.

In ejecta representing the end of the Plinian eruption and subsequent dome effusion (Chapters 2, 3), a prevalence of collapse textures is indicative of prolonged residence time of magma in the conduit permitting development of mature bubble textures. Textures in Episode I pumice, in comparison to episodes IV and V, were created predominantly by bubble nucleation and growth and lack collapse signatures. Reminiscent of layers C-F, modal density rhyolite and dacite from layers A and B have mostly thin glass walls and the bubbles lack the pinched, irregular shapes seen in the Episode IV and V domes (Chapter 3). Continuous nucleation and growth appear to have been overprinted by major coalescence during ascent of the melt.

#### **4.5.2 Signature of conduit formation during eruption of phase A**

The first known eruption of rhyolitic melt at Novarupta was during phase A of the 1912 eruption, and no vent structure was known in the area prior to the eruption. This allows us to ask the question: what was the influence of conduit formation and widening on the initial ascent and vesiculation of the opening phase? The first erupted products, or Layer A, and specifically lower A, can be examined to answer this question, and the signature appears to be threefold. First, we observe a relatively broad density/vesicularity range in the earliest erupted samples (Layer A, Fig. 4.6). Second, the Layer A vesicle size distribution is skewed toward coarser bubble sizes (Fig. 4.13). Third, we observe stretched or elongated large bubbles in the pyroclasts (bottom A, Fig. 4.9).

To discern the relationship between conduit dynamics and textural signatures, the interplay between conduit geometry, mass flux, and shear zones are considered. In a simple model for a Bingham fluid flowing in a pipe with a relatively small width, as in the case of conduit formation, velocity values would continually increase towards the center of the conduit in parabolic fashion, and shearing occurs across the entire width (Fig. 4.14). If with time the conduit width increases, under the same rheological conditions, shear zones develop along the sides of the conduit and bound a non-shearing plug. Ascent of this plug is described by a region of almost constant velocity bounded by sharp velocity gradients close to the conduit walls (Fig. 4.14) (Cas and Wright 1987; Dobran 2001; Holman 2002).

The ascent of the Layer A rhyolitic melt marked the opening of the Novarupta conduit. We assume that the conduit radius during this initial ascent was relatively small

and increased as Episode I continued based on the high percentage of wall-rock lithics in the Layer A fall deposits. Thus at the beginning of the eruption, velocity could be described with a parabolic profile, and marginal portions of the melt would experience a relatively slow ascent. Slower ascent would mean more time for the magma to efficiently degas, i.e., more closely approximate equilibrium degassing, and for bubbles to grow and experience extended coalescence (Proussevitch and Sahagian 1996). The result would be fewer but larger bubbles and ultimately a higher degree of connectivity (Gardner et al. 1996). Open pathways would also drive outgassing of marginal melt via the conduit walls (Jaupart 1998) and result in clasts with lower vesicularities (Polacci et al. 2001; Polacci et al. 2003). Variation in velocity and ascent rate across the conduit would explain the broad density range of the Layer A samples. Plug flow would not yet have developed at the start of the eruption, so shearing would be expected across the entire width of the conduit. Shearing after bubble nucleation would stretch vesicles (Marti et al. 1999; Polacci et al. 2001; Polacci et al. 2003), and the early Layer A rhyolites show the most conspicuously elongated vesicles of all the Episode I products. As the conduit evolved and widened, plug flow would ensue so that only the small proportion of the magma that was ascending along the conduit margins would experience significant shear. Magma across most of the width of the conduit, i.e., within the plug, would ascend at approximately equal velocity and experience similar degassing histories. This is in accordance with the observation that the pyroclasts from the top of Layer A show a smaller range in densities and no noticeable vesicle elongation.

#### 4.5.3 Comparison of coeval dacite and rhyolite

The dacite and rhyolite magmas erupted simultaneously during phase B were characterized by similar degassing histories based on the qualitative and quantitative data on the respective vesicle populations. Textures in both appear to have resulted from continuous vesicle nucleation, growth by diffusion and decompression, and a strong influence of coalescence. The compositions did mingle and produce rhyolite-dacite banded clasts; as stated above, the dacitic bands had slightly smaller bubbles compared to rhyolitic bands, but both demonstrated the same textural signatures. That is, the onset of mingling appears to have had little effect on the vesiculation pattern of either composition.

Textures in co-erupted compositions can also be compared using all-rhyolite and all-dacite clasts erupted at the same time. During phase B<sub>2</sub>, approximately equal proportions of dacite and rhyolite were erupted, but the large bubbles of the all-rhyolite and all-dacite clasts are distinctly different, even between clasts with similar densities (Figs. 4.6, 4.9, 4.10). Unusually large bubbles in the B<sub>2</sub> dacite are also seen in B<sub>3</sub> dacite (Fig. 4.10), and in layer B<sub>3</sub>, dacite completely dominates the erupting material. Large bubbles might suggest a slower ascent and therefore a path proximal to the conduit walls. Marginal ascent would also mean ascent in shear zones, but vesicle elongation is not prevalent in any dacite pumice. Furthermore, by phase B<sub>3</sub> dacite would all but fill the conduit and therefore not be confined to the margins. The differences between the rhyolite and dacite textures may reflect that for a significant portion of their ascent, dacite

and rhyolite traveled in separate conduits with contrasting ascent histories and only met in the shallow conduit immediately beneath Novarupta.

#### 4.5.4 Contrasting behavior of dacitic melt during episodes I, II and III

Comparing the dacite melt erupted during phase B of Episode I with that erupted during episodes II and III, contrasts between magmas of identical bulk composition but erupted at different intensities can be made. If Episode I lasted for a total of ~16 hours and erupted a total of ~9.5 km<sup>3</sup> of magma (Fierstein and Hildreth 1992; Hildreth and Fierstein 2000), the *average* magma discharge rate including ignimbrite was  $4.0 \times 10^8$  kg/s ( $=9.5 \text{ km}^3 \cdot 2400 \text{ kg/m}^3 \cdot 16 \text{ hr}^{-1}$ ) (Hildreth 1991). Considering episodes I-III are constrained to have lasted in total ~60 hours and subtracting Episode I (16 hrs) as well as several hours for the breaks between episodes, 4 km<sup>3</sup> of magma erupted during ~35-40 hours during episodes II and III combined. Hence, the average magma discharge rate during episodes II-III was  $8.7 \times 10^7$  kg/s (DRE: 2450 kg/m<sup>3</sup>) and thus decreased compared to Episode I.

In terms of bubble number density ( $N_{V \text{ total}}$  and  $N_{V \text{ total}}^m$ ), dacitic pumices in Episode I (when fall deposition was accompanied by voluminous ignimbrites) and the clasts in episodes II and III (characterized by more stable but lower intensity Plinian eruption) are remarkably similar  $7 \times 10^7 - 2 \times 10^9 \text{ cm}^{-3}$  (Tables 2.1, 4.1). More significant contrasts exist between values of bulk vesicularity. The range between vesicularity minima and maxima for the sample of the earliest erupted dacitic melt (phase B<sub>1</sub>) is the largest of all 1912 dacitic samples from episodes I-III (Figs. 4.6, 4.7, 2.5), including the other dacitic pumice from later phases (B<sub>2</sub>, B<sub>3</sub>) of Episode I. The range of

density/vesicularity is even more striking than in the earliest erupted rhyolite. This range in the B<sub>1</sub> dacite sample rivals that of the Episode IV blocks (Fig. 3.7; Tables 3.2, 3.3) postulated to have formed due to significant development of zones of open-system degassing and has interesting implications for the entry of dacitic melt into the 1912 eruption. Are the dense dacitic clasts the result of dacitic melt forcing its way through a conduit filled with rhyolitic magma? Alternatively, do the low densities imply the dacitic melt had to open a new arm of the conduit system *before* coming in contact with its rhyolitic analog?

#### 4.6 Conclusions

Plinian activity during episodes I-III of the 1912 eruption produced pyroclasts with undeniable textural similarities. Bubble number densities in the order of  $10^7$ - $10^9$  cm<sup>-3</sup> and broadly unimodal VVDs signify rapid ascent of the melt phases, bubble nucleation via disequilibrium degassing, and growth strongly influenced by coalescence. However, distinctive signatures are observed for the first rhyolite (phase A) and the first dacite (Phase B<sub>1</sub>) to be erupted during Episode I. The Layer A rhyolite features can be directly linked in time to the opening and evolution of the 1912 conduit. A parabolic velocity profile describes ascent of melt through a relatively narrow conduit, i.e., during the initial stages of conduit formation. Non-plug flow, a wide and continuous range of ascent velocities, and significant shear across the conduit resulted in the wide range of densities and elongated vesicles seen in the lower Layer A rhyolitic samples. The first dacite erupted, subunit B<sub>1</sub>, was also characterized by a wide range of densities compared to both Episode I rhyolites as well as episode II-III dacites. Since the conduit width had

increased by phase B, and plug flow develops with increased conduit width, the wide range of densities cannot directly be explained by changes in conduit radius. Unusually large bubbles in Episode I dacite additionally suggests a complex ascent relationship between the rhyolite and dacite melt sharing the shallow conduit at the same time.

#### **4.7 Acknowledgements**

Our work was supported by NSF grant EAR-01-06700. Images were collected on the SEM belonging to HIGP (Hawaii Institute of Geophysics & Planetology).

**Table 4.1** Results of vesicle quantification.

Composition	Layer	Density (kg/m <sup>3</sup> )	Vesicularity (%)	N <sub>A total</sub> (cm <sup>-2</sup> )	N <sub>V total</sub> (cm <sup>-3</sup> )	N <sup>m</sup> <sub>V total</sub> (cm <sup>-3</sup> )	n no./cm <sup>3</sup> /cm	Size	no. included	Median (μm)	Mode (μm)	Skew	Kurtosis
								Range (μm)					
D	C	650	73.4	1.6E+05	1.0E+08	4.3E+08	4.2E+11	8-3152	2220	75	80	1.25	0.68
R		650	72.5	5.8E+04	3.7E+07	1.2E+08	1.3E+11	8-2504	733	133	200	0.85	-0.81
D	B	670	75.2	4.0E+05	5.4E+08	1.9E+09	3.9E+12	4-1989	2747	58	80	0.69	-1.07
R		680	71.0	3.5E+05	5.4E+08	1.6E+09	4.4E+12	4-3152	1031	48	80	1.05	-0.19
R	A	640	72.7	8.7E+04	7.2E+07	2.2E+08	3.0E+11	8-1989	1550	136	300; 80*	0.44	-1.64

vesicularity - DRE values of 2350 and 2450 kg/m<sup>3</sup> were used to calculate vesicularities for rhyolites and dacites, respectively.

N<sub>A total</sub> - areal number density of vesicles

N<sub>V total</sub> - volumetric number density of vesicles; referenced to whole clast

N<sup>m</sup><sub>V total</sub> - volumetric number density of vesicles; referenced to melt only

n - population number density

\* - subpeak

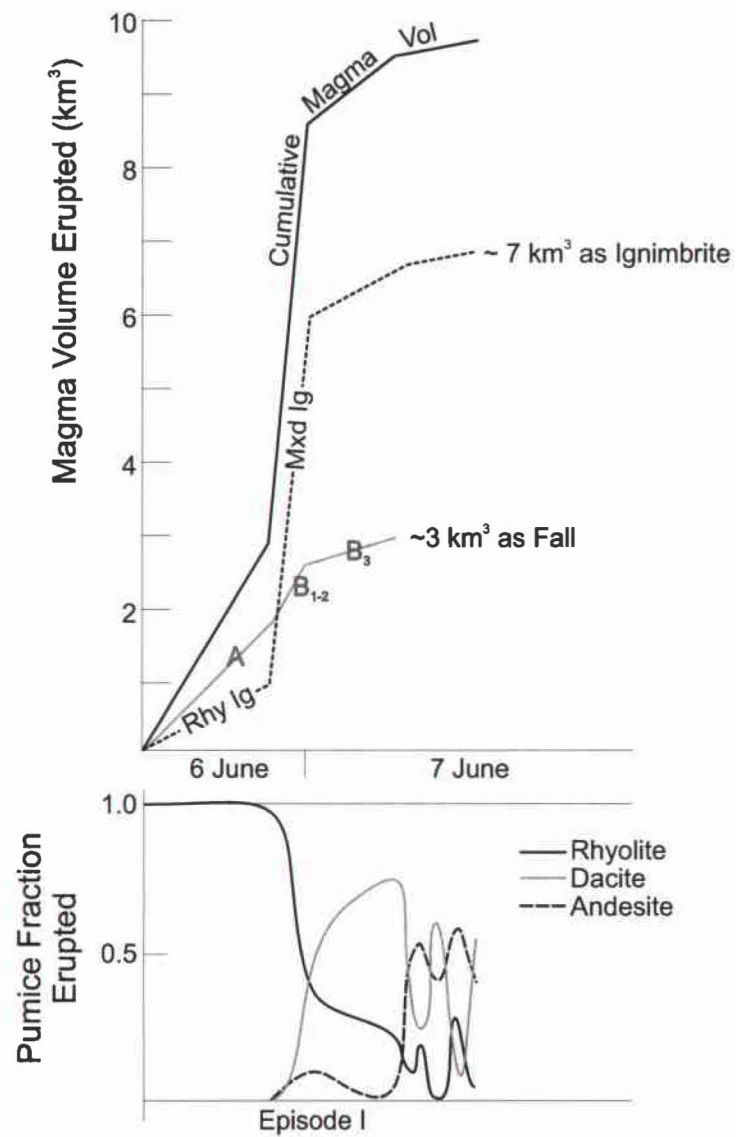


**Figure 4.1** modified from Hildreth and Fierstein (2000); plots of increasing magma volume per flow unit and corresponding changes in proportions of erupting material per composition.

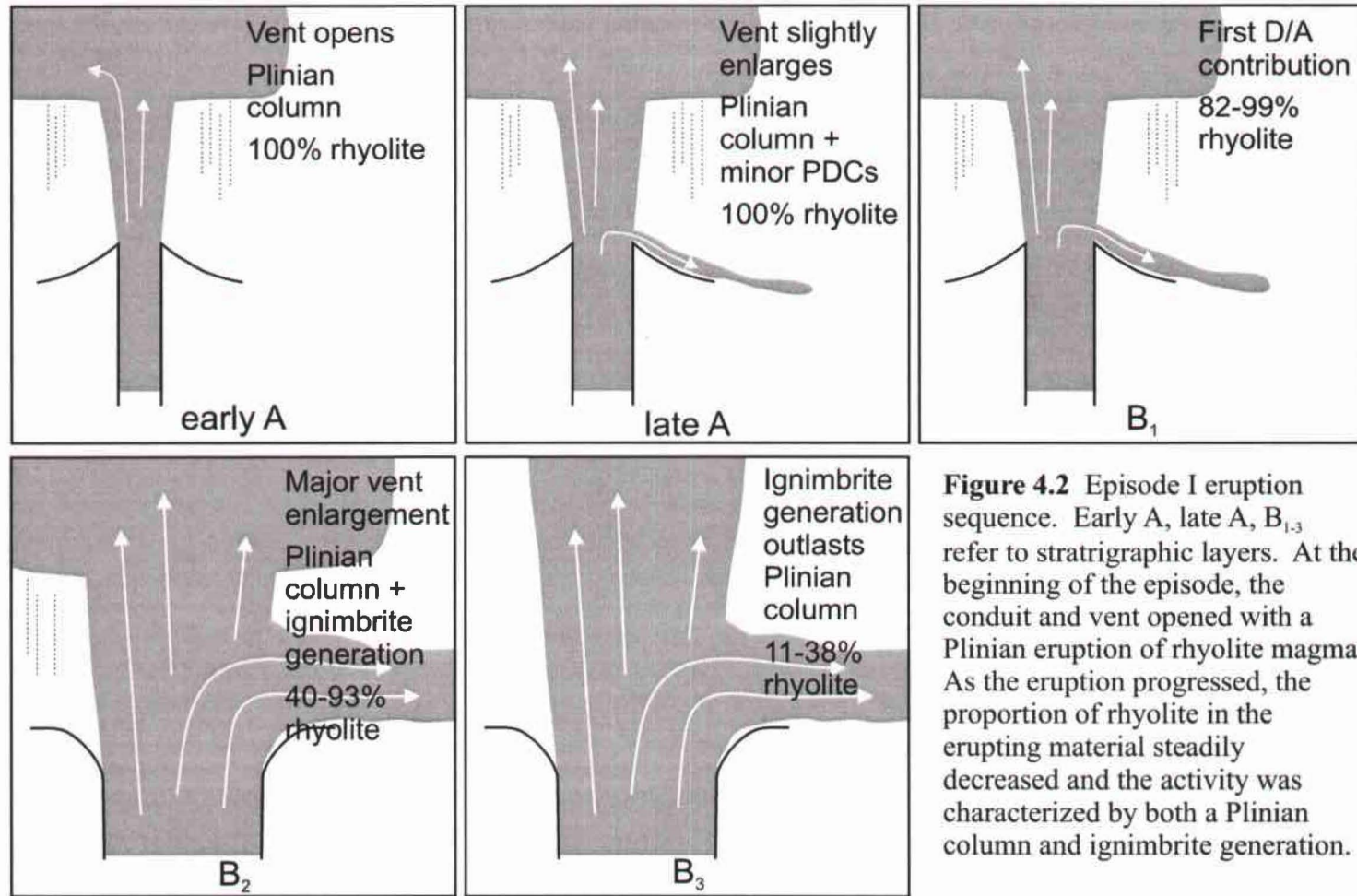


**Figure 4.2** Episode I eruption sequence. Early A, late A, B<sub>1-3</sub> refer to stratigraphic layers. At the beginning of the episode, the conduit and vent opened with a Plinian eruption of rhyolite magma. As the eruption progressed, the proportion of rhyolite in the erupting material steadily decreased and the activity was characterized by both a Plinian column and ignimbrite generation.



1 km

**Figure 4.3** Aerial photo in the ESE perspective of the near vent region. The Episode I crater is traced with a dashed line; the current dome (Episode V) is marked (N). Falling mountain (FM) was a pre-existing dacite dome truncated by the creation of the 2 km wide crater. Caldera collapse occurred 10 km E at Mount Katmai; the proximal vent region is filled with 1912 deposits including layers C-H and the main valley filling ignimbrite (VFI).

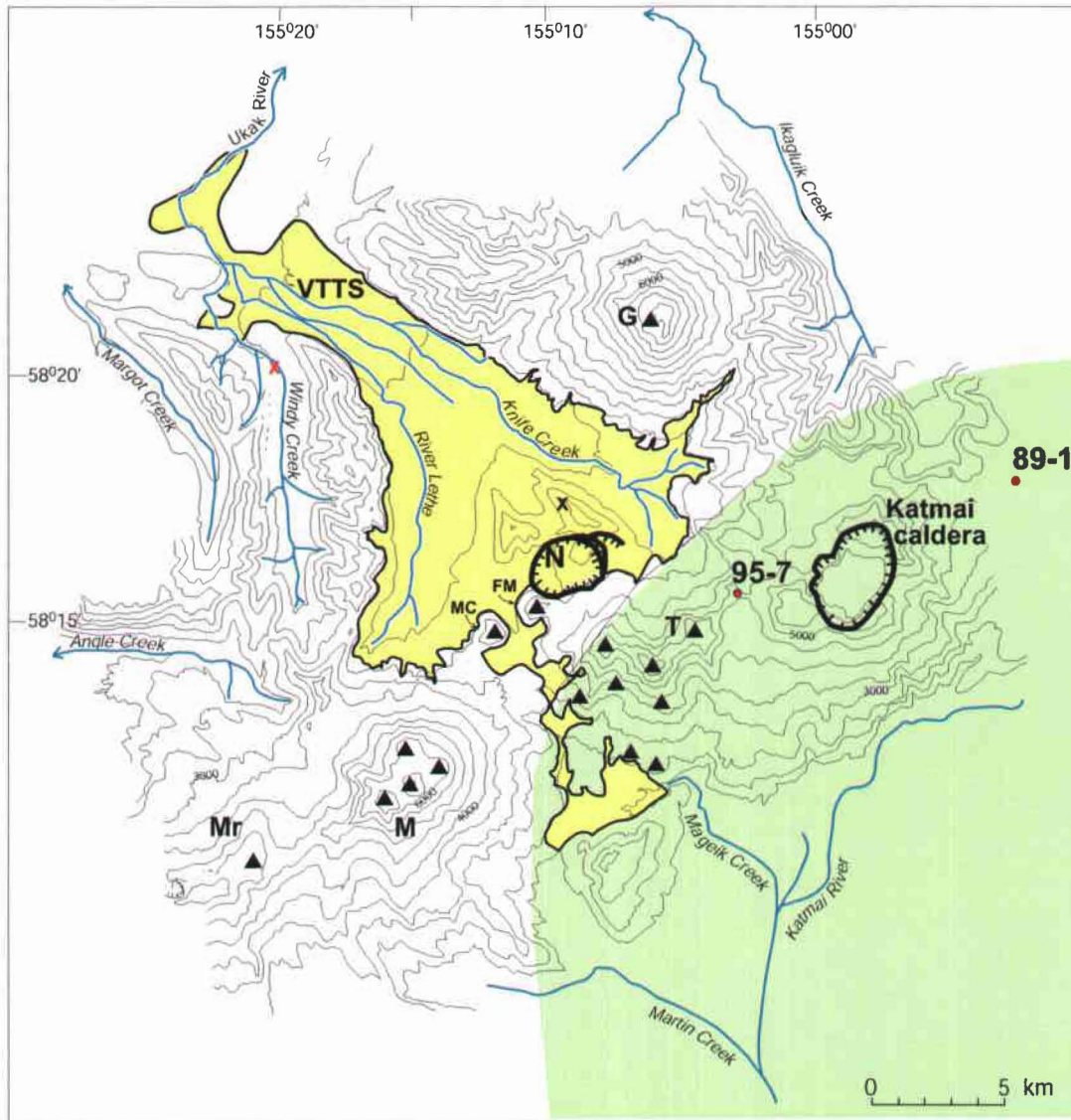


**Figure 4.4** modified from Hildreth and Fierstein (2000); dispersal area for Episode I fall deposits (layers A and B) shaded in green. Fallout is strongly directed SE of the Novarupta (N) vent due to wind and scouring by contemporaneous flows. Sample sites 89-1 and 95-7 indicated with dots. Valley of Ten Thousand Smokes (VTTS) ignimbrite in yellow; nearby composite volcanoes Martin (Mr), Mageik (M), Griggs (G), Trident (T); nearby domes Falling Mountain (FM), Mount Cerebus (MC).

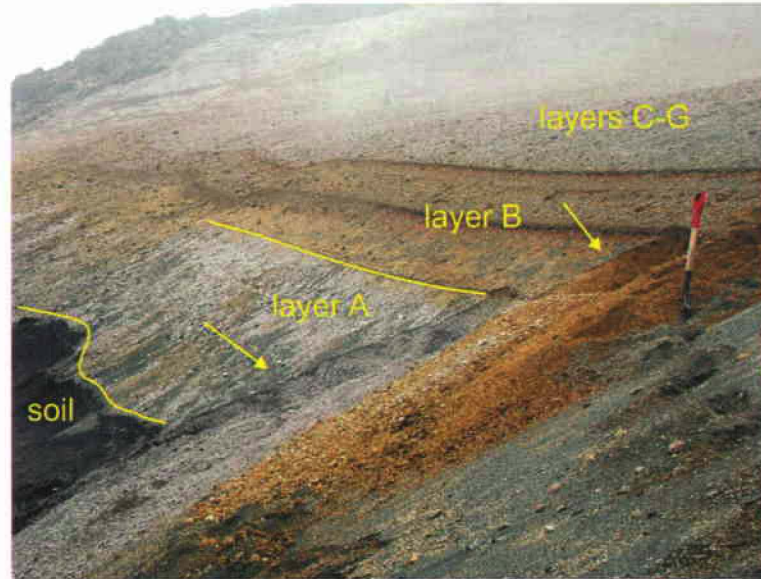


**Figure 4.5** Plinian fall layers at site 89-1. Arrows point to trenches dug while logging stratigraphy and collecting samples used to study transitions within eruptive episodes.

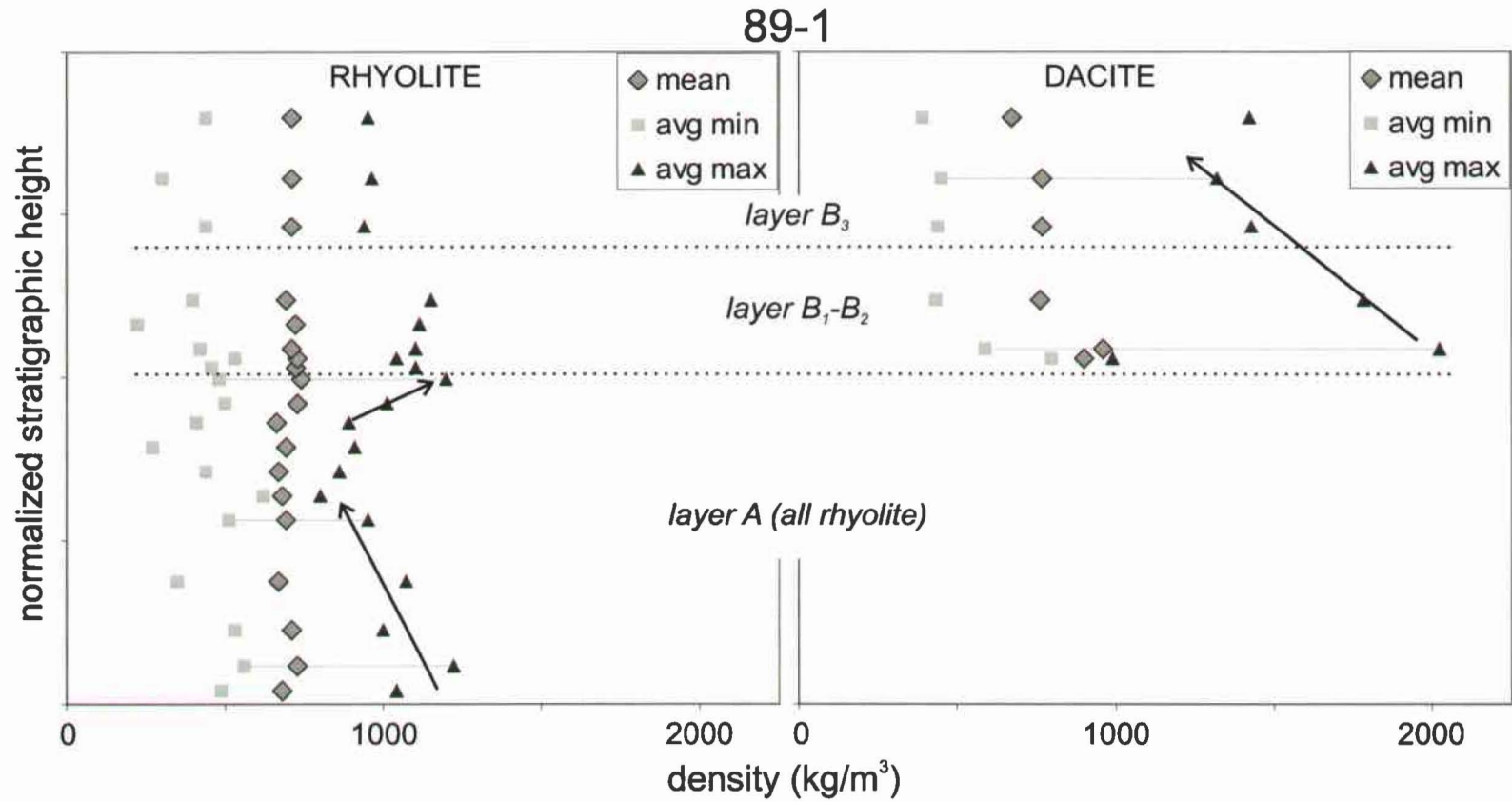


**Figure 4.6** Plot of density changes with stratigraphic height at site 89-1. Each sample consists of ~100 clasts of pumice; density measured for each clast. The mean of each sample is shown as well as the average of the three minimum density clasts (avg min) and the three maximum density clasts (avg max). Lines illustrate trends in the data. Layer  $B_3$  is distinguishable from lower B by a Katmai mud layer (Hildreth, 1991).

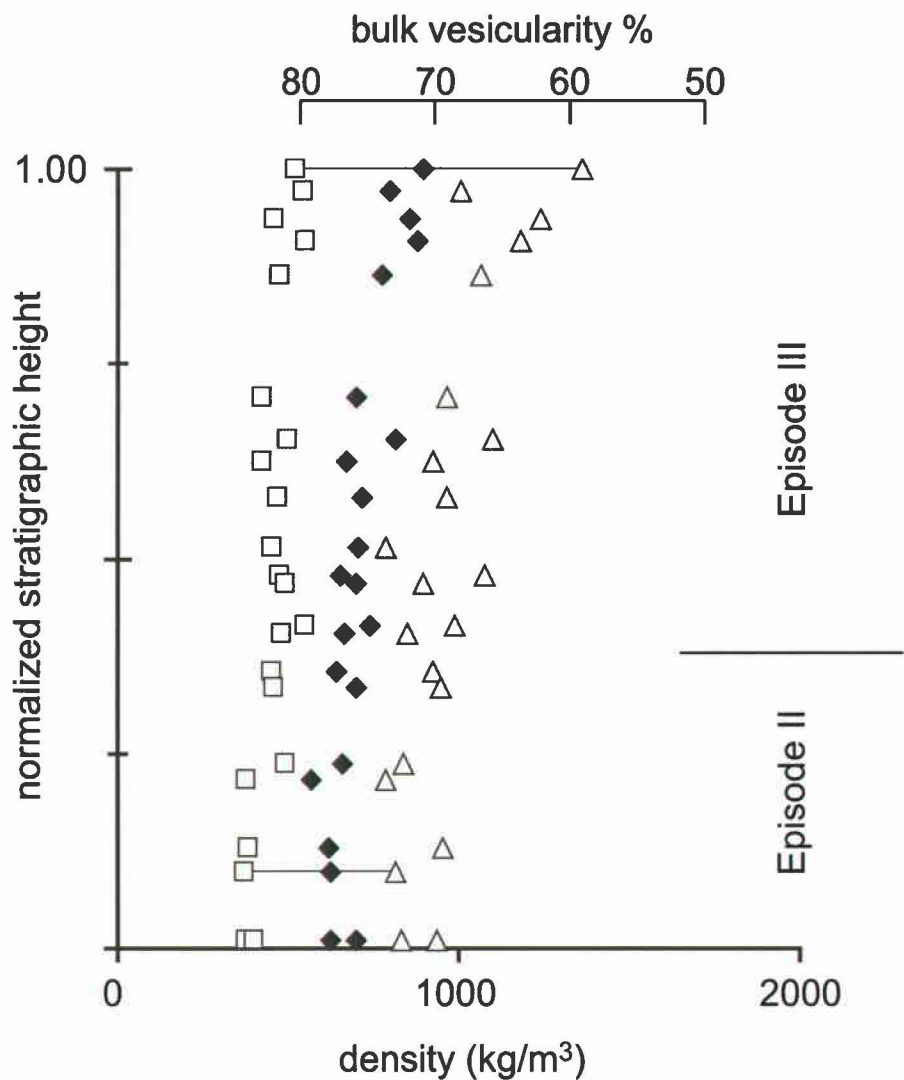


**Figure 4.7** Low, mean, and high density values against normalized stratigraphic height for samples collected throughout episodes II and III fall deposits at site 94-1 (Chapter 2). Triangles represent an average of the three maximum density clasts per sample; squares an average of the three minimum density clasts. Mean density value and the range in densities per sample increased as the eruption progressed.

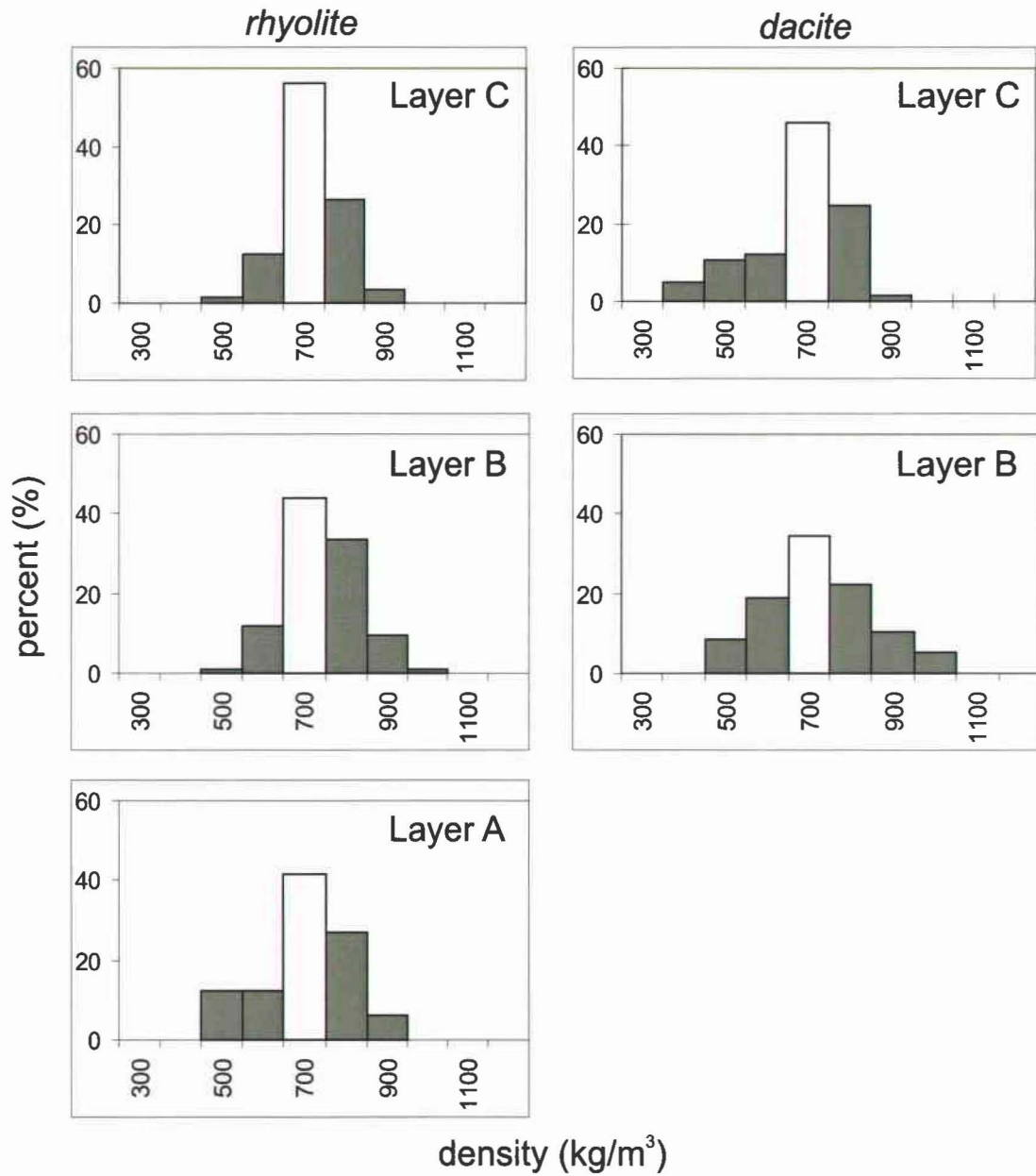


**Figure 4.8** Density distributions of bulk samples. Layer C dacite was collected at site 94-1 (Chapter 2). Pumice used for image analysis and vesicle quantification taken from peak density (white).

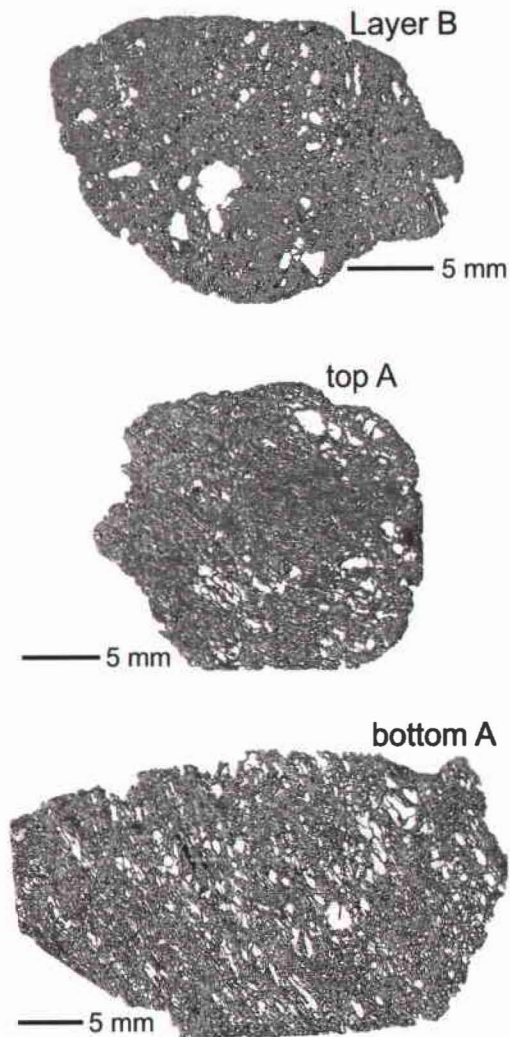


**Figure 4.9** Scanned thin sections of rhyolite pumice. Notice how bubble elongation is lost from Layer A to Layer B. The Layer B clast shown is representative of rhyolite throughout phase B (B<sub>1</sub>-B<sub>3</sub>). Rhyolite did not significantly contribute to episodes II-IV; the Episode V dome, however, is contaminated rhyolite.

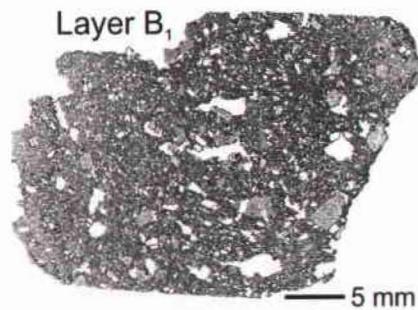
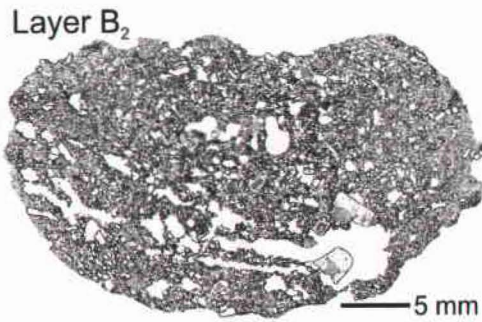
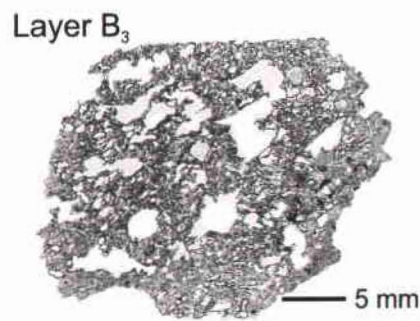
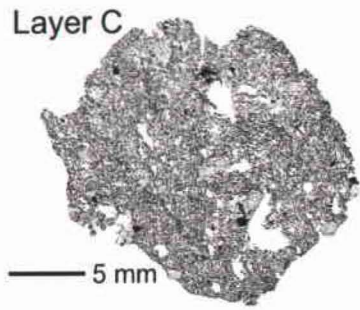


**Figure 4.10** Scanned thin sections of dacite pumice. As Phase B continued, the density decrease is marked by bubble trains and an increasing number of large bubbles. The first dacite erupted when the eruption continued in Episode II (Layer C) has similar density to Layer B<sub>3</sub> but lacks the large bubbles.

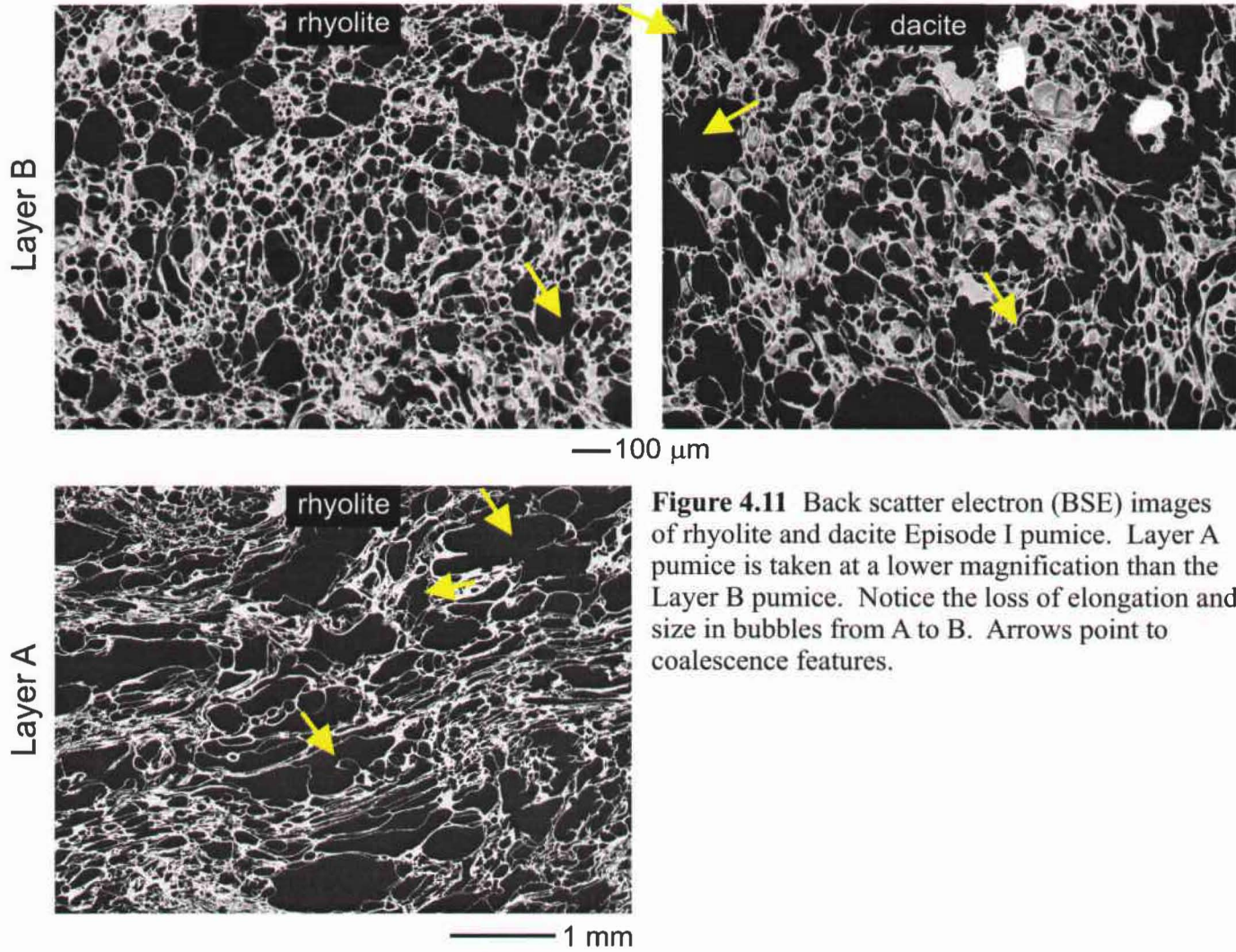


**Figure 4.11** Back scatter electron (BSE) images of rhyolite and dacite Episode I pumice. Layer A pumice is taken at a lower magnification than the Layer B pumice. Notice the loss of elongation and size in bubbles from A to B. Arrows point to coalescence features.

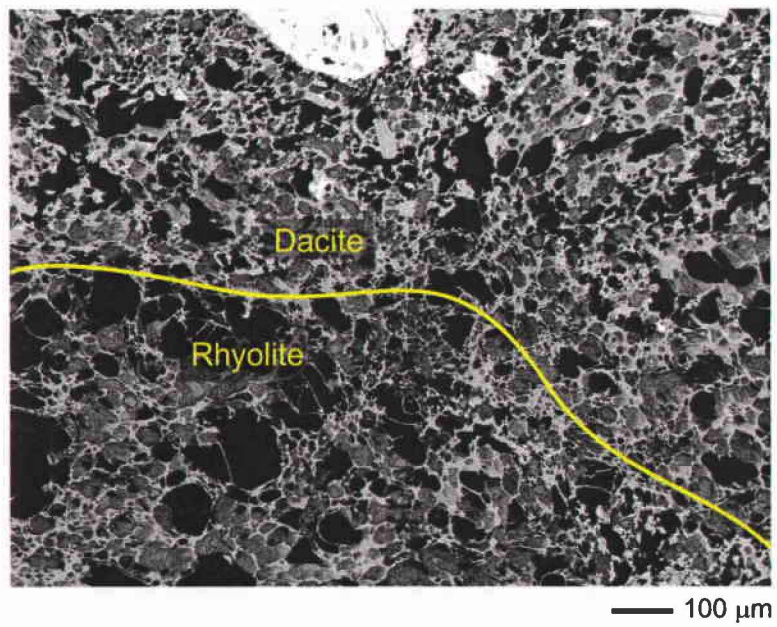
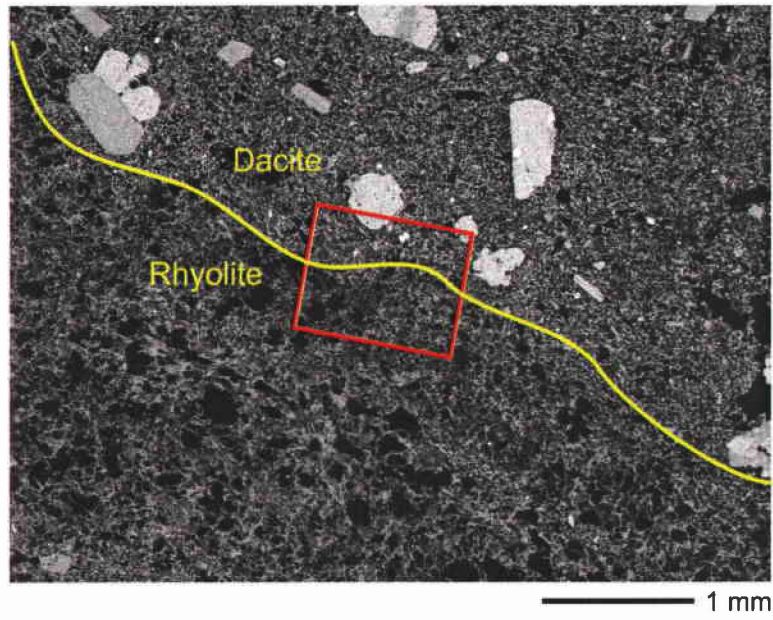


**Figure 4.12** BSE image across a rhyolite-dacite contact in a  $B_1$  clast. Red box enlarged in lower image. Vesicles are black.

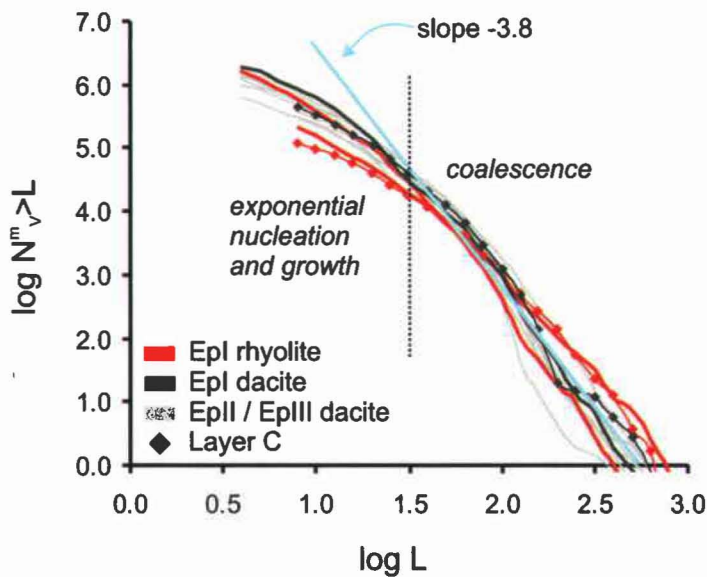
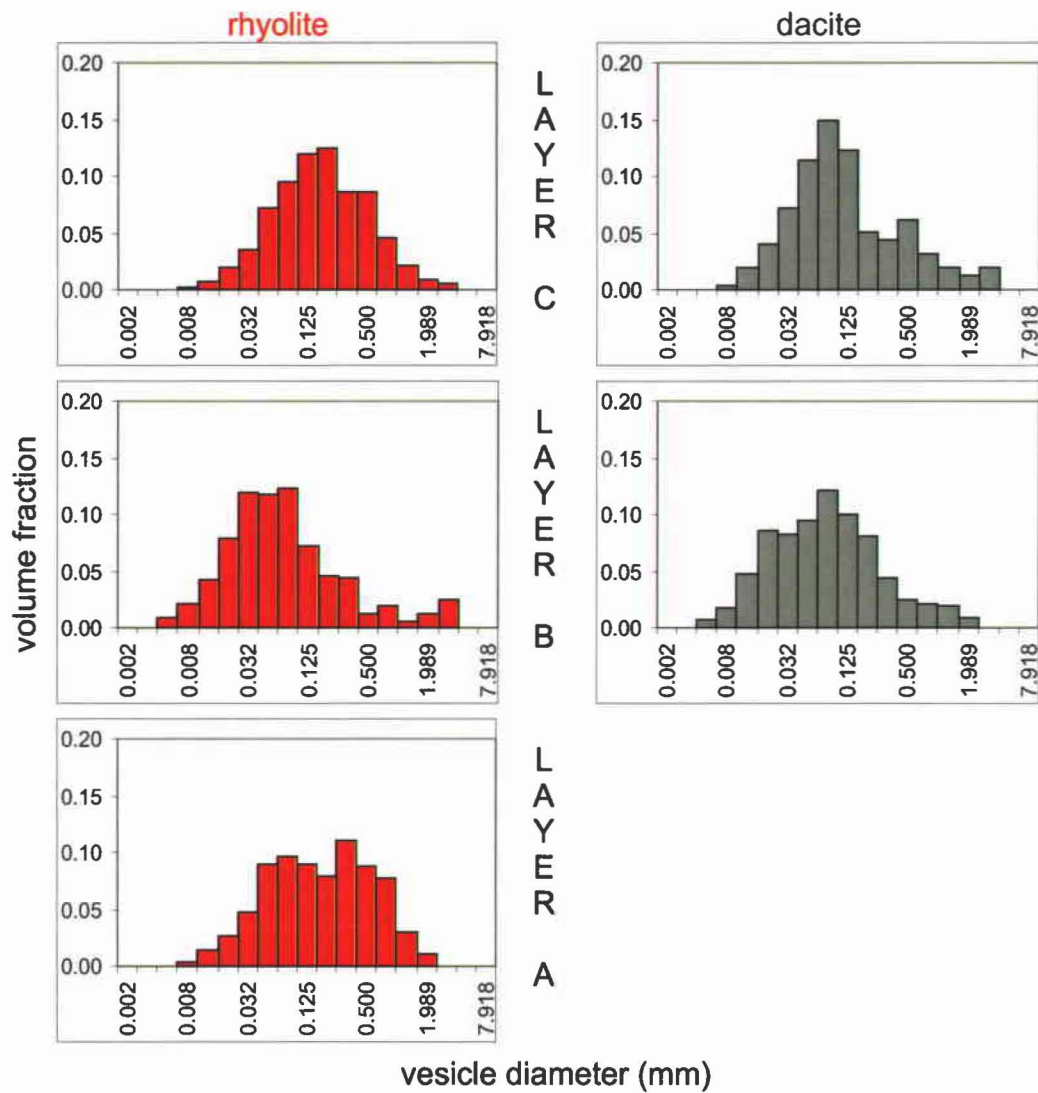


**Figure 4.13** TOP: vesicle volume distributions (VVDs) for layers A, B (Episode I) and C (start of Episode II) rhyolite and dacite pumice. BOTTOM: vesicle cumulative number densities ( $N_v^m > L$ ) against vesicle diameter sizes ( $L, \mu\text{m}$ ) on a log-log scale. Both rhyolite and dacite from Episode I coincides with Episode II-III dacite.

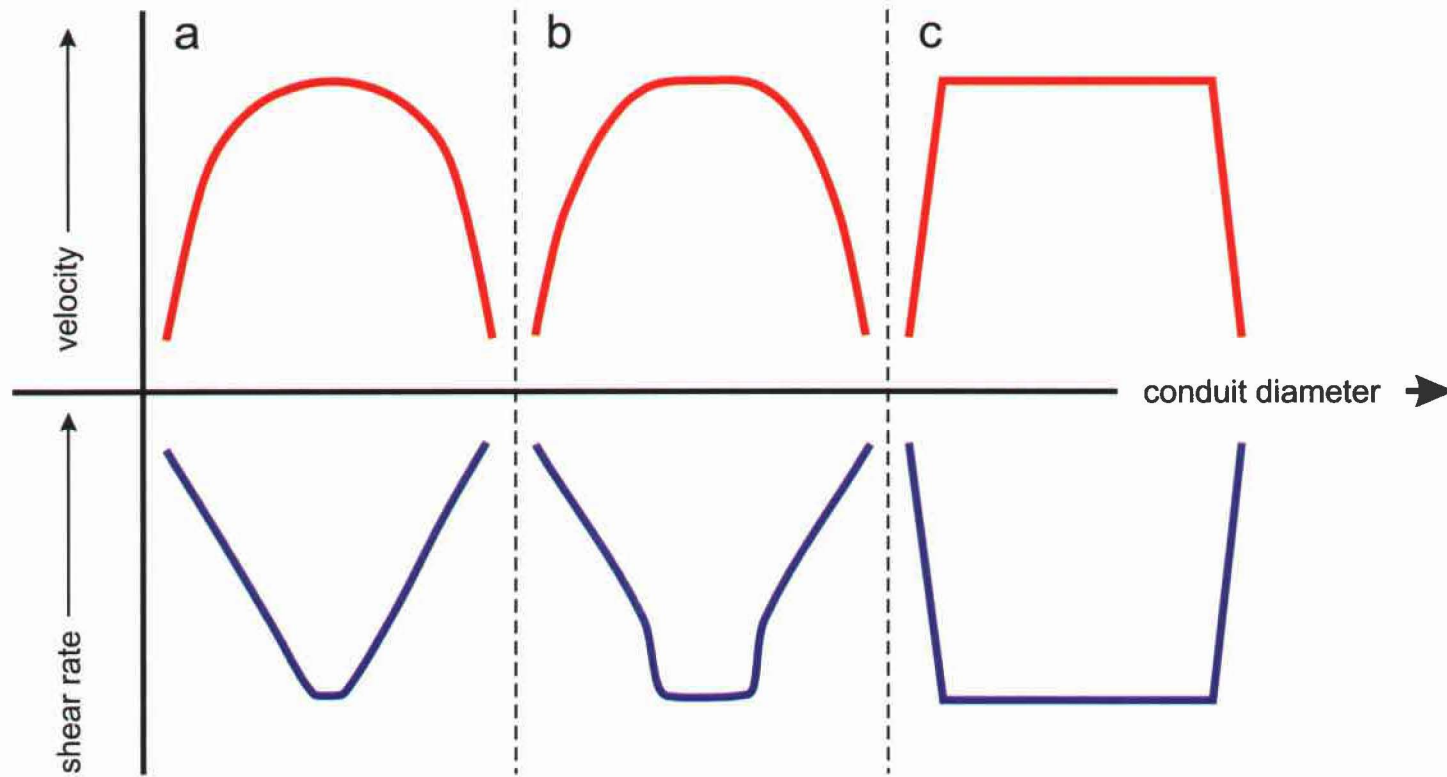


**Figure 4.14** Velocity and shear profiles across conduit width. When conduit width is small (a), shearing occurs across the entire width. If the width increases (b), a plug develops and is bounded by shear zones along the margins. Shear rates increase with an increase in the volumetric flux, but shear rates decrease if the flux stays constant. If the conduit becomes sufficiently wide (c), shearing does still occur along the margins but plug flow dominates.

## CHAPTER 5

### Conclusions

#### 5.1 Vesiculation and degassing processes during the 1912 eruption

The 1912 explosive products are strikingly uniform in their vesicularity. Pyroclasts have high bubble number densities ( $10^8$  to  $10^9$  cm<sup>-3</sup>) and a strong predominance of bubbles of diameter 50 to 125  $\mu$ m which suggests very similar vesiculation histories, particularly for the early stages of ascent and vesiculation involving nucleation and free growth of bubbles. This generalization holds true irrespective of melt composition (dacite versus rhyolite) and stratigraphic position. In fact, the products of all waxing and stable Plinian phases of the eruption show similar vesiculation histories. Strong, disequilibrium degassing and delayed nucleation and growth of vesicles produced pumice with high vesicularities and thin glass walls. Once initiated, nucleation is continuous; early bubble growth is controlled by diffusion and decompression. However, at a certain bubble size (our data suggest  $\sim 30$   $\mu$ m), coalescence becomes the dominant manner of growth and overprints nucleation signatures, e.g., smaller bubbles expanding into larger ones, amoeboid shapes. These similarities imply that changes during the eruption were driven by processes in the shallower portions of the conduit system.

However, the earliest erupted rhyolitic pumice from Episode I and the last erupted dacite clasts in Episode III are exceptions to the patterns described above. I suggest these

pumice reflect two significant variations on the pattern of rapid ascent and disequilibrium degassing that characterized episodes I through III of the eruption.

Textures in the first (rhyolitic) pyroclasts to erupt show strong long-tube fabric, consistent with conduit shear. Since no vent existed at Novarupta prior 1912, the first magma to ascend and create the conduit would have experienced significant shearing across the width of the conduit prior to the establishment of plug flow. The consistency and degree of elongation which describes the early Episode I products are absent in later pyroclasts erupted after a conduit was well established. Under these conditions, I infer that plug flow ensued. The proportion of magma experiencing shear was limited to the bounding shear zones and hence reduced in comparison to magma ascending with the initially parabolic velocity profile. Early ascent was probably significantly slower than during later open-conduit conditions, and additional residence time in the shallow conduit led to larger modal bubble sizes.

During Episode III, we see a progressive shift in bulk density samples towards an increased range of pumice density/vesicularity and towards a decreased mean vesicularity. These changes are forerunners of the shift to open-system degassing that I postulate drove the transition from explosive to effusive eruption. I infer slowed ascent and extended residence time in the conduit for melt traveling up the margins led to the onset of bubble collapse and outgassing co-eval with melt ascending along the axis that was still freely degassing. Rheological stiffening accompanied this process and further impeded the ascent of melt adjacent to the conduit margins. The thickness of this zone of partially outgassed melt increased both with time and with height in the conduit and

ultimately led to a reduction in effective conduit radius and a decrease in mass discharge rate. Such trends are not seen in the later products of episodes I and II, each of which were followed by a resumption in explosive activity.

The expanding range of clast density/vesicularity seen in the later products of Episode III is continued into effusive Episode IV. Textures ranging from pumiceous to dense in the Episode IV dacite dome/plug blocks suggest a history of heterogeneous degassing which ultimately led to destruction of the dome/plug via Vulcanian explosion(s). The densest juvenile material is characterized by low bubble number densities, low vesicularities, and pinched vesicle shapes and represents the natural continuation of bubble collapse and free gas escape that had begun by the end of Episode III. Episode IV block populations also include pumiceous juvenile dacite similar to the episodes II and III pumice which indicates at least some portions of the Episode IV melt experienced closed-system degassing. We suggest that stable dome growth was not possible while a significant portion of the magma was still ascending relatively rapidly and undergoing closed-system degassing.

A switch to eruption of rhyolitic melt which had presumably remained resident in some portion of the conduit system since Episode I led to extrusion of more uniformly outgassed magma with respect to Episode IV. The absence of strong, disequilibrium degassing in any portion of this late-stage rhyolitic melt probably ensured the stable growth of the Episode V dome.

## 5.2 General conclusions about vesiculation in silicic magma

The 1912 eruption of Novarupta in Alaska is an excellent case for studying conduit dynamics and evolving vent geometries. In addition to understanding the degassing and vesiculation patterns that defined the shifts and pauses throughout the five episodes of the 1912 eruption, broader insights can be made concerning conduit processes for silicic systems:

- Textures are a powerful tool for discerning internal changes in an ascending magma.
- The manner of degassing, specifically, affects eruption dynamics and is heralded by changes in the bulk density and microtextures of fall deposits.
- The significance of vesiculation processes including nucleation, growth (decompression, diffusion, *and* coalescence), and collapse relative to one another can be assessed qualitatively and quantitatively.
- Experimental results must be used in conjunction with natural samples. High number densities suggest large, explosive eruptions are characterized by disequilibrium degassing and at least partially subject to homogeneous nucleation.
- During magma ascent in a conduit, nucleation appears to be a continuous process, and early bubble growth is dominated by diffusion and decompression. After bubbles reach a certain size, growth is controlled predominantly by coalescence.
- Collapse is a later stage in bubble maturation and is marked by thicker glass walls, pinched bubble-shapes, and smaller cumulative number densities; it is associated with decoupled degassing (open-system).

- Collapse can be a self-limiting process. It occurs by gas escaping freely but effectively closes the pathways for the gas to escape and the system returns to closed-system degassing.
- Portions of co-erupted magma may share very different ascent and vesiculation histories which are likely linked to cross-conduit variations in ascent rate and conduit residence time.
- Magmas of different compositions sharing a conduit can degas independently of one another.

### **5.3 Transition from closed to open system degassing in silicic magmas**

From the peak of explosive activity to waning explosive activity to dome effusive activity, textures of the erupted products indicate progressively more of the melt passes through a transition between closed- and open-system degassing. We suggest this transition begins in the portions of the melt along the margins of the conduit where slower ascent velocity leads to extended residence time in the conduit and greater opportunity for approximation to equilibrium degassing. Given the effects of extended degassing on melt rheology as well as the onset of bubble connectivity via cascading coalescence, a threshold is exceeded in melt along the margins of the conduit beyond which pathways via permeability and relatively stable fractures allow open-system degassing. With time the annular zone of melt affected by this partial outgassing widens. These progressive internal changes, however, significantly affect eruptive regime only when the effective radius of the conduit is reduced to a point where discharge is first

inhibited and then ceases. Explosive activity and its associated disequilibrium degassing come to an end if the upper portion of the conduit is effectively blocked by outgassed melt. However continued closed system degassing of melt close to the axis of the conduit and ascent of fresh melt from depth may supply momentum needed for effusion of the overlying outgassed melt as lava domes or plugs. This process of early dome growth is inherently ephemeral because gas released from newly arrived melt will trigger Vulcanian explosions and dome disruption.

#### **5.4 Pauses and breaks during explosive silicic eruptions**

While convecting columns are often sustained on timescales of hours, sharp bedding planes in fall deposits of Plinian eruptions show pauses frequently occur throughout the course of explosive activity. Are such breaks caused by internal changes to the rheology of the melt ascending in the conduit, or are they due to external influences? Breaks caused by slowed magma ascent and outgassing in the shallow conduit are likely to lead to a permanent shift from explosive to effusive eruption style whereas, in the latter case, explosive volcanism may resume abruptly. Evidence suggests that both have occurred at Novarupta. At the closes of episodes I and II, no significant textural change occurs in the erupted melt. Instead, strong indirect evidence suggests that both breaks are associated with changes in vent geometry. At the close of Episode I, the vent had widened to form a 2-km wide crater which had become choked with fall back ejecta. Minor wall collapse terminated Episode II, and explosive volcanism only resumed when the vent was cleared by a blast which produced a pyroclastic density

current. Conversely, a progressive switch to dominantly open-system degassing first recorded in denser clasts led to the end of plinian Episode III.

How do we identify the cause of such breaks in older or less well exposed Plinian sequences? Size grading, i.e., changing grain size throughout pyroclastic deposits, is useful for interpreting shifts in eruption intensity, but changes in ascent rate and degassing histories are best discerned using changes in the vesicularity and textures of the pyroclasts. Meticulous sampling throughout the stratigraphy with special attention to the bottoms/tops of layers permits examination of variations in bulk vesicularity, VSD, and bubble shape, i.e., internal changes, with time. External causes can be ascertained using contrasts in the wall rock content above and below unconformities in the deposits in combination with the eruption style and the manner of emplacement of the deposits immediately overlying the break, e.g., the blast-like PDC4 at Novarupta.

Finally, many finer and progressive shifts in grain size are apparent in the 1912 Plinian deposits. These fine shifts reflect fluctuations in intensity more subtle than the abrupt shut-downs and pauses described and interpreted here. Explanation of the underlying causes of these variations is a new major challenge in physical volcanology.

## **5.5 Future directions**

This study has greatly enhanced our understanding of the degassing of silicic magmas during large and sustained eruptions and its effects on eruption style and intensity. In addition to the direct insights it yields for the 1912 eruption, from a broader

vantage of physical volcanology, it illuminates additional areas that can be considered in future studies:

- Bubble collapse remains the least understood or quantified of vesiculation processes yet is critical to understanding the explosive/effusive transition. New numerical models of bubble collapse and its effects on VSDs, VVDs, and number densities are immediately required.
- Experimental simulations of vesiculation in rhyolitic melts have focused on nucleation and growth, but many unanswered questions remain concerning bubble collapse, particularly its rates and its influence on bubble shapes. Laboratory constraints on this process would be useful.
- Few detailed VSD/VVD studies of silicic pumice have been performed. This lack of data has created a high priority for establishing a database of vesicle measurements across a wide range of eruptive intensities (subplinian to ultraplinian) and a diversity of melt composition, e.g., trachyte, phonolite, peralkaline rhyolite.
- Very few field studies are tied to rigorous sampling over narrow stratigraphic intervals, and few samples contain sufficient clasts to characterize the endmember (both high and low) vesicularities in single stratigraphic levels. This study has demonstrated the utility of characterizing clasts of very high density to understand across-conduit heterogeneity and its influence in altering eruption intensity.
- Laboratory investigations of melt rheology have focused on the influence of volatile loss in essentially static settings. Physical volcanology would benefit

from constraints on changing melt rheology with changing bubble size, thinning of glass walls, and the imposition of sudden non-linear accelerations due to melt expansion.

## APPENDIX

### Data repository

Textural analysis is characteristically data-rich, and during the course of this project, much data was collected for the products of the Novarupta 1912 eruption. The chapters of this dissertation use the data to accomplish the major objectives. The author recognizes, however, the value of the data in its raw form. As such, I have included in an attached DVD the relevant data in various stages of processing. In this way, the dissertation acts as a repository for the images collected as well as documents my area to volume conversion techniques.

Data is divided into *processed* and *raw*, or unprocessed, images:

**Raw:** The raw data are the original images captured directly from a scanner or SEM as TIFFs (i.e. with a .tiff file extension). They are initially divided into *scans* and *SEM*, and each of these categories are further divided into *Episode I*, *Episodes II-III*, and *Episodes IV-V* following Chapters 2-4. Every image contained within each episode-folder was collected from a clast itself collected from a depositional layer resulting from fall erupted during that particular episode. *Episode I* contains *dacites*, *rhyolites*, and a separate folder named *89-1 (Garcia)*. Images in this 89-1 folder were captured on a scanner owned by Michael Garcia, and all others scans were made on a scanner owned by Bruce Houghton from 2000- November 2004. *Episodes II-III* is divided into *andesites* and *dacites*.

*Episodes IV-V* is divided into *dense dacites*, *Ep V dome*, *flow banded*, *pumiceous*, and *transitional* to reflect the different categories of blocks characterizing the Episode IV and Episode V domes.

**Processed:** The processed data is immediately divided into *Episode I*, *Episodes II-III*, and *Episodes IV-V*. As in the *raw* data folder, every image contained within each episode-folder was collected from a clast itself collected from a depositional layer resulting from fall erupted during that particular episode. *Episode I* consists of *dacite*, *rhyolites*, and *only paper* folders. The *only paper* folder is further subdivided into *dacite*, *rhyolite*, and *RD banded* and houses Photoshop and bitmap images (giffs and jpegs) within clast-identified folders, e.g. *89-1-15D-20*, that were processed only for illustrative purposes, not for use in Scion. The *dacite* and *rhyolites* folders directly under the *Episode I* also contain folders named with individual clast identifications, e.g. *95-7-10-14*. Every clast-id folder in the processed data category outside of the *only paper* folder contains four additional folders: *numbers*, *paper*, *scan*, and *SEM*. The *SEM* folder contains the binary images of the higher magnification images collected on the SEM and used in Scion to measure vesicles, crystals, etc. (*bin images*). It also contains the Photoshop images made during the creation of the binary images (*psd layers*). *Scan* contains the binary and photoshop files created when processing the image collected using a flatbed scanner. Here, *paper* refers to Photoshop and bitmap images (giffs and jpegs) that have been used in both Scion and for illustrative purposes such as figures of chapters 2-4. The *numbers* folders have two types of Microsoft Excel spreadsheets: 1)

spreadsheets with area, length, and axes measurements made per vesicle per image, and  
2) spreadsheets which detail the process of converting from vesicle area to volume.

*Episodes II-III* includes *andesite*, *dacites*, and *rhyolite* folders, each of which contain  
clast-id folders following the same taxonomy as in the *Episode I* folder, i.e., numbers,  
paper, scan, and SEM. *Episodes IV-V* is divided into *dense dacites*, *Ep V dome*,  
*pumiceous*, and *transitional*, and each of these are further subdivided into clast-id folders.

When the images within each individual clast folder, itself within each *Episode IV-V*  
folder, were processed in Scion, the taxonomy of the clast-id folder follows the above  
description (*numbers*, *scan*, *SEM*, and *paper* if it was also used in a figure).

RECEIVED

AS

FOLLOWS



## REFERENCES

- Anderson SW, Fink JH (1989) The development and distribution of surface textures at the Mount St. Helens Dome. *IAVCEI Proceedings in Volcanology* 2: 25-46
- Anderson SW, Fink JH, Rose WI (1995) Mount St. Helens and Santiaguito lava domes: the effect of short-term eruption rate on surface texture and degassing processes. *Journal of Volcanology and Geothermal Research* 69: 105-116
- Barberi F, Cioni R, Rosi M, Santacroce R, Sbrana A, Vecci R (1989) Magmatic and phreatomagmatic phases in explosive eruptions of Vesuvius as deduced by grain size and component analysis of the pyroclastic deposits. *Journal of Volcanology and Geothermal Research* 38: 287-307
- Barmin A, Melnik O, Sparks RSJ (2002) Periodic behavior in lava dome eruptions. *Earth and Planetary Science Letters* 199: 173-184
- Blower JD, Keating JP, Mader HM, Phillips JC (2001a) Inferring volcanic degassing processes from vesicle size distributions. *Geophysical Research Letters* 28: 347-350
- Blower JD, Keating JP, Mader HM, Phillips JC (2002) The evolution of bubble size distributions in volcanic eruptions. *Journal of Volcanology and Geothermal Research* 120: 1-23
- Blower JD, Mader HM, Wilson SDR (2001b) Coupling of viscous and diffusive controls on bubble growth during explosive volcanic eruptions. *Earth and Planetary Science Letters* 193: 47-56

- Bursik MI, Carey SN, Sparks RSJ (1992) A gravity current model for the May 18, 1980 Mount St. Helens plume. *Geophysical Research Letters* 19: 1663-1666
- Bursik MI, Woods AW (1991) Buoyant, superbuoyant and collapsing eruption columns. *Journal of Volcanology and Geothermal Research* 45: 347-350
- Carey S, Sigurdsson H (1989) The intensity of Plinian eruptions. *Bulletin of Volcanology* 51: 28-40
- Carey S, Sigurdsson H, Gardner JE, Criswell W (1990) Variations in column height and magma discharge during the May 18, 1980 eruption of Mount St Helens. *Journal of Volcanology and Geothermal Research* 43: 99-112
- Carey S, Sparks RSJ (1986) Quantitative models of the fallout and dispersal of tephra from volcanic eruption columns. *Bulletin of Volcanology* 48: 109-125
- Cas RAF, Wright JV (1987) *Volcanic Successions: Modern and Ancient*. Allen and Unwin London, 528 pp
- Cashman KV (1992) Groundmass crystallization of Mount St Helens dacite, 1980-1986 - a tool for interpreting shallow magmatic processes. *Contributions to Mineralogy and Petrology* 109: 431-449
- Cashman KV, Mangan MT (1994) Physical aspects of magmatic degassing. II. Constraints on vesiculation processes from textural studies of eruptive products. In: Carroll MR, Holloway JR (ed) *Volatiles in Magmas*, 30, pp 447-478
- Cashman KV, Marsh BD (1988) Crystal size distribution (CSD) in rocks and the kinetics and dynamics of crystallization. II. Makaopuhi Lava Lake. *Contributions to Mineralogy and Petrology* 99: 292-305

- Cashman KV, Sturtevant B, Papale P, Navon O (2000) Magmatic fragmentation. In: Sigurdsson H (ed) Encyclopedia of Volcanoes, Academic Press pp 421-430
- Cioni R, Santacroce R, Sbrana A (1999) Pyroclastic deposits as a guide for reconstructing the multi-stage evolution of the Somma-Vesuvius Caldera. Bulletin of Volcanology 61: 207- 222
- Coombs ML, Gardner JE (2001) Shallow-storage conditions for the rhyolite of the 1912 eruption at Novarupta, Alaska. Geological Society of America Bulletin 29: 775-778
- Curtis GH (1968) The stratigraphy of the ejecta of the 1912 eruption of Mount Katmai and Novarupta, Alaska. Geological Society of America Bulletin 72: 153-210
- Dingwell DB (1996) Volcanic dilemma: flow or blow? Science 273: 1054-1055
- Dingwell DB (1998) The glass transition in hydrous granitic melts. Physics of the Earth and Planetary Interiors 107: 1-8
- Dingwell DB, Webb SL (1990) Relaxation in silicate melts. European Journal of Mineralogy 2: 427-449
- Dobran F (2001) Volcanic Processes: Mechanisms in Material Transport. Kluwer Academic/Plenum Publishers New York, 620 pp

- Druitt TH, Young SR, Baptie B, Bonadonna C, Calder ES, Clarke AB, Cole PD, Harford CL, Herd RA, Luckett R, Ryan G, Voight B (2002) Episodes of cyclic Vulcanian explosive activity with fountain collapse at Soufrière Hills Volcano, Montserrat. In: Druitt TH, Kokelaar BP (ed) *The Eruption of Soufrière Hills Volcano, Montserrat, from 1995 to 1999*, 21, Geological Society, London, Memoirs pp 281-306
- Eichelberger JC (1995) Silicic volcanism: ascent of viscous magmas from crustal reservoirs. *Annual Review of Earth and Planetary Sciences* 23: 41-63
- Eichelberger JC, Carrigan CR, Westrich HR, Price RH (1986) Non-explosive silicic volcanism. *Nature* 323: 598-602
- Eichelberger JC, Izbekov PE (2000) Eruption of andesite triggered by dyke injection: contrasting cases at Karymsky Volcano, Kamchatka and Mt Katmai, Alaska. *Philos Trans R Soc Lond Ser A-Math Phys Eng Sci* 358: 1465-1485
- Eichelberger JC, Koch FG (1979) Lithic fragments in the Bandelier Tuff, Jemez mountains, New Mexico. *Journal of Volcanology and Geothermal Research* 5: 115-134
- Ernst GGJ, Sparks RSJ, Carey SN, Bursik MI (1996) Sedimentation from turbulent jets and plumes. *Journal of Geophysical Research* 101: 5575-5589
- Fagents SA, Wilson L (1993) Explosive volcanic eruptions-VII. The ranges of pyroclasts ejected in transient volcanic explosions. *Geophysical Journal International* 113: 359-370

- Fierstein J, Hildreth W (1992) The plinian eruptions of 1912 at Novarupta, Katmai National Park, Alaska. *Bulletin of Volcanology* 54: 646-684
- Fierstein J, Houghton BF, Wilson CJN, Hildreth W (1997) Complexities of plinian fall deposition at vent: an example from the 1912 Novarupta eruption (Alaska). *Journal of Volcanology and Geothermal Research* 76: 215-227
- Fink JH, Anderson SW (2000) Lava domes and coulees. In: Sigurdsson H (ed) *Encyclopedia of Volcanoes*, Academic Press pp 307-319
- Fink JH, Malin MC, Anderson SW (1990) Intrusive and extrusive growth of the Mount St Helens lava dome. *Nature* 348: 435-437
- Fink JH, Manley CR (1987) Origin of pumiceous and glassy textures in rhyolite flows and domes. *Geol Soc Am Spec Pap* 212: 77-88
- Francis P (1993) Pyroclastic flows: ignimbrites. In: *Volcanoes, a Planetary Perspective*, pp 208-235
- Gaonac'h H, Lovejoy S, Schertzer D (2004) Scaling vesicle distributions and volcanic eruptions. *Bulletin of Volcanology online*: August
- Gaonac'h H, Lovejoy S, Stix J, Schertzer D (1996a) A scaling growth model for bubbles in basaltic lava flows. *Earth and Planetary Science Letters* 139: 395-409
- Gaonac'h H, Stix J, Lovejoy S (1996b) Scaling effects on vesicle shape, size and heterogeneity of lavas from Mount Etna. *Journal of Volcanology and Geothermal Research* 74: 131-153

- Gardner CA, Cashman KV, Neal CA (1998) Tephra-fall deposits from the 1992 eruption of Crater Peak, Alaska: implications of clast textures for eruptive processes. *Bulletin of Volcanology* 59: 537-555
- Gardner JE, Hilton M, Carroll MR (1999) Experimental constraints on degassing of magma: isothermal bubble growth during continuous decompression from high pressure. *Earth and Planetary Science Letters* 168: 201-218
- Gardner JE, Thomas RME, Jaupart C, Tait S (1996) Fragmentation of magma during Plinian volcanic eruptions. *Bulletin of Volcanology* 58: 144-162
- Geschwind CH, Rutherford MJ (1995) Crystallization of microlites during magma ascent: the fluid mechanics of 1980-1986 eruptions at Mount St Helens. *Bulletin of Volcanology* 57: 356-370
- Gonnermann HM, Manga M (2003) Explosive volcanism may not be an inevitable consequence of magma fragmentation. *Nature* 426: 432-435
- Griggs RF (1922) *The Valley of Ten Thousand Smokes*. National Geographic Society Washington, D.C., 340 pp
- Gurioli L, Houghton B, Cashman K, Cioni R (2004) Complex changes in eruption dynamics during the 79 AD eruption of Vesuvius. *Bulletin of Volcanology* 67: 144-159
- Hammer JE, Cashman KV, Hoblitt RP, Newman S (1999) Degassing and microlite crystallization during pre-climactic events of the 1991 eruption of Mt. Pinatubo, Philippines. *Bulletin of Volcanology* 60: 355-380

- Hammer JE, Rutherford MJ, Hildreth W (2002) Magma storage prior to the 1912 eruption at Novarupta, Alaska. *Contributions to Mineralogy and Petrology* 144: 144-162
- Harris AJL, Rose WI, Flynn LP (2003) Temporal trends in lava dome extrusion at Santiaguito 1922-2000. *Bulletin of Volcanology* 65: 77-89
- Hess KU, Dingwell DB (1996) Viscosities of hydrous leucogranitic melts: a non-Arrhenian model. *American Mineralogist* 81: 1297-1300
- Hildreth W (1983) The compositionally zoned eruption of 1912 in the Valley of Ten Thousand Smokes, Katmai National Park, Alaska. *Journal of Volcanology and Geothermal Research* 18: 1-56
- Hildreth W (1987) New perspectives on the eruption of 1912 in the Valley of Ten Thousand Smokes, Katmai National Park, Alaska. *Bulletin of Volcanology* 49: 680-693
- Hildreth W (1991) The timing of caldera collapse at Mount Katmai in response to magma withdrawal towards Novarupta. *Geophysical Research Letters* 18: 1541-1544
- Hildreth W, Fierstein J (2000) Katmai volcanic cluster and the great eruption of 1912. *Geological Society of America Bulletin* 112: 1594-1620
- Hildreth W, Mahood GA (1986) Ring-fracture eruption of the Bishop Tuff. *Geological Society of America Bulletin* 97: 396-403
- Hirth JP, Pound GM, St. Pierre GR (1970) Bubble nucleation. *Metallurgical Transactions* 1: 939-945
- Holman JP (2002) *Heat Transfer*. McGraw-Hill 665 pp

- Houghton BF, Hobden BJ, Cashman KV, Wilson CJN, Smith RT (2003) Large-scale interaction of lake water and rhyolitic magma during the 1.8 ka Taupo eruption, New Zealand. In: White JDL, Smellie JL, Clague DA (ed) Explosive Subaqueous Volcanism, Geophysical Monograph 140, American Geophysical Union pp 97-109
- Houghton BF, Wilson CJN (1989) A vesicularity index for pyroclastic deposits. *Bulletin of Volcanology* 51: 451-462
- Houghton BF, Wilson CJN, Del Carlo PO, Coltelli M, Sable JE, Carey R (2004a) The influence of conduit processes on changes in style of basaltic plinian eruptions: Tarawera 1886 and Etna 122 BC. *Journal of Volcanology and Geothermal Research* 137: 1-14
- Houghton BF, Wilson CJN, Fierstein J, Hildreth W (2004b) Complex proximal deposition during the Plinian eruptions of 1912 at Novarupta, Alaska. *Bulletin of Volcanology* 66: 95-133
- Hurwitz S, Navon O (1994) Bubble nucleation in rhyolite melts: experiments at high pressure, temperature, and water content. *Earth and Planetary Science Letters* 122: 267-280
- Jaupart C (1996) Physical models of volcanic eruptions. *Chemical Geology* 128: 217-227
- Jaupart C (1998) Gas loss from magmas through conduit walls during eruption. In: Gilbert JS, Sparks RSJ (ed) *The Physics of Explosive Volcanic Eruptions*, 145, Geological Society, Special Publications pp 73-90

- Jaupart C, Allegre CJ (1991) Gas content, eruption rate and instabilities of eruption regime in silicic volcanoes. *Earth & Planetary Science Letters* 102: 413-429
- Jaupart C, Tait S (1994) Dynamics of eruptive phenomena. In: Carroll MR, Holloway JR (ed) *Volatiles in Magmas, Reviews in Mineralogy Mineralogical Society of America* pp 213-238
- Klug C, Cashman KV (1994) Vesiculation of May 18, 1980, Mount St. Helens magma. *Geology* 22: 468-472
- Klug C, Cashman KV (1996) Permeability development in vesiculating magmas: implications for fragmentation. *Bulletin of Volcanology* 58: 87-100
- Klug C, Cashman KV, Bacon CR (2002) Structure and physical characteristics of pumice from the climactic eruption of Mount Mazama (Crater Lake), Oregon. *Bulletin of Volcanology* 64: 486-501
- Kokelaar BP (2002) Setting, chronology and consequences of the eruption of Soufrière Hills Volcano, Montserrat (1995-1999). In: Druitt TH, Kokelaar BP (ed) *The Eruption of Soufrière Hills Volcano, Montserrat, from 1995 to 1999*, 21, Geological Society, London, *Memoirs* pp 1-43
- Koyaguchi T (1994) Grain-sized variation of tephra derived from volcanic umbrella clouds. *Bulletin of Volcanology* 56: 1-9
- Lowenstern JB (1993) Evidence for a copper-bearing fluid in magma erupted at the Valley of Ten Thousand Smokes, Alaska. *Contributions to Mineralogy and Petrology* 114: 409-421

- Lyakhovskiy V, Hurwitz S, Navon O (1996) Bubble growth in rhyolitic melts: experimental and numerical investigation. *Bulletin of Volcanology* 58: 19-32
- Macedonio G, Dobran F, Neri A (1994) Erosion processes in volcanic conduits and application to the AD 79 eruption of Vesuvius. *Earth and Planetary Science Letters* 121: 137-152
- Manga M, Castro J, Cashman KV, Loewenberg M (1998) Rheology of bubble-bearing magmas. *Journal of Volcanology and Geothermal Research* 87: 15-28
- Mangan MT, Cashman KV (1996) The structure of basaltic scoria and reticulite and inferences for vesiculation, foam formation, and fragmentation in lava fountains. *Journal of Volcanology and Geothermal Research* 73: 1-18
- Mangan MT, Cashman KV, Newman S (1993) Vesiculation of basaltic magma during eruption. *Geology* 21: 157-160
- Mangan MT, Mastin L, Sisson T (2004) Gas evolution in eruptive conduits: combining insights from high temperature and pressure decompression experiments with steady-state flow modeling. *Journal of Volcanology and Geothermal Research* 129: 23-36
- Mangan MT, Sisson T (2000) Delayed, disequilibrium degassing in rhyolite magma: decompression experiments and implications for explosive volcanism. *Earth and Planetary Science Letters* 183: 441-455
- Marsh BD (1988) Crystal size distribution (CSD) in rocks and the kinetics and dynamics of crystallization. I. Theory. *Contributions to Mineralogy and Petrology* 99: 277-291

- Marti J, Soriano C, Dingwell DB (1999) Tube pumices as strain markers of the ductile-brittle transition during magma fragmentation. *Nature* 402: 650- 653
- Martin GC (1913) The recent eruption of Katmai volcano in Alaska. *National Geographic Magazine* 24: 131-181
- Massol H, Jaupart C (1999) The generation of gas overpressure in volcanic eruptions. *Earth and Planetary Science Letters* 166: 57-70
- Matthews SJ, Gardeweg MC, Sparks RSJ (1997) The 1984 to 1996 cyclic activity of Lascar volcano, northern Chile: cycles of dome growth, dome subsidence, degassing and explosive eruptions. *Bulletin of Volcanology* 59: 72-82
- Mellors RA, Waite Jr. RB, Swanson DA (1988) Generation of pyroclastic flows and surges by hot-rock avalanches from the dome of Mount St. Helens volcano, USA. *Bulletin of Volcanology* 50: 14-25
- Melnik O (2000) Dynamics of two-phase conduit flow of high-viscosity gas-saturated magma: large variations of sustained explosive eruption intensity. *Bulletin of Volcanology* 62: 153-170
- Melnik O, Sparks RSJ (1999) Nonlinear dynamics of lava dome extrusion. *Nature* 402: 37- 41
- Melnik O, Sparks RSJ (2002) Dynamics of magma ascent and lava extrusion at Soufrière Hills Volcano, Montserrat. In: Druitt TH, Kokelaar BP (ed) *The Eruption of Soufrière Hills Volcano, Montserrat, from 1995 to 1999*, 21, Geological Society, London, *Memoirs* pp 153-171

- Moore JG, Lipman PW, Swanson DA, Alpha TR (1981) Growth of lava domes in the crater, June 1980-January 1981. US Geol Surv Prof Pap 1250: 541-547
- Mourtada-Bonnefoi CC, Laporte D (1999) Experimental study of homogenous bubble nucleation in rhyolitic magmas. *Geophysical Research Letters* 26: 3505-3508
- Navon O, Lyakhovsky V (1998) Vesiculation processes in silicic magmas. In: Gilbert GS, Sparks RSJ (ed) Geological Society of London, Special Publication, 145, pp 27-50
- Orsi G, Gallo G, Heiken G, Wohletz K, Yu E, Bonani G (1992) A comprehensive study of pumice formation and dispersal: the Cretatio tephra of Ischia (Italy). *Journal of Volcanology and Geothermal Research* 53: 329-354
- Paladio-Melosantos ML, Solidum R, Scott WE, R.B. Q, Umbal JV, Rodolfo KS, Tubianosa BS, Delos Reyes PJ (1995) Tephra falls of the 1991 eruptions of Mount Pinatubo. In: Newhall CGP, R.S. (ed) *Fire and Mud: Eruptions and Lahars of Mount Pinatubo, Philippines*, Washington Press pp 513-535
- Papale P (1998) Volcanic conduit dynamics. In: Freundt A, Rosi M (ed) *From magma to tephra: modelling physical processes of explosive volcanic eruptions*, Elsevier pp 55-89
- Parfitt EA, Wilson L (1999) A Plinian treatment of fallout from Hawaiian lava fountains. *Journal of Volcanology and Geothermal Research* 88: 67- 75
- Pinkerton H, Stevenson RJ (1992) Methods of determining the rheological properties of magmas at sub-liquidus temperatures. *Journal of Volcanology and Geothermal Research* 53: 47-66

- Polacci M, Papale P, Rosi M (2001) Textural heterogeneities in pumices from the climactic eruptions of Mount Pinatubo, 15 June 1991, and implications for magma ascent dynamics. *Bulletin of Volcanology* 63: 83-97
- Polacci M, Pioli L, Rosi M (2003) The Plinian phase of the Campanian Ignimbrite eruption (Phlegrean Fields, Italy): evidence from density measurements and textural characterization of pumice. *Bulletin of Volcanology* 65: 418-432
- Proussevitch AA, Sahagian DL (1996) Dynamics of coupled diffusive and decompressive bubble growth in magmatic systems. *Journal of Geophysical Research* 101: 17447-17455
- Proussevitch AA, Sahagian DL (1998) Dynamics and energetics of bubble growth in magmas: analytical formulation and numerical modeling. *Journal of Geophysical Research* 103: 18223-18251
- Proussevitch AA, Sahagian DL, Kutolin VA (1993) Stability of foams in silicate melts. *Journal of Volcanology and Geothermal Research* 59: 161-178
- Pyle DM (1989) The thickness, volume and grain-size of tephra fall deposits. *Bulletin of Volcanology* 51: 1-15
- Rosi M, Paladio-Melosantos ML, Dimuro A, Leoni R, Bacolcol T (2001) Fall vs flow activity during the 1991 climactic eruption of Pinatubo Volcano (Philippines). *Bulletin of Volcanology* 62: 549- 566
- Rust AC, Manga M, Cashman KV (2003) Determining flow type, shear rate and shear stress in magmas from bubble shapes and orientations. *Journal of Volcanology and Geothermal Research* 122: 111-132

- Sahagian DL, Proussevitch AA (1998) 3D particle size distributions from 2D observations - stereology for natural applications. *Journal of Volcanology and Geothermal Research* 84: 173- 196
- Sato H, Fujii T, Nakada S (1992) Crumbling of dacite dome lava and generation of pyroclastic flows at Unzen volcano. *Nature* 360: 664-666
- Self S (1992) Krakatau revisited: the course of events and interpretation of the 1883 eruption. *GeoJournal* 28: 109-121
- Self S, Rampino MR (1981) The 1883 eruption of Krakatau. *Nature* 294: 699-704
- Sigurdsson H, Carey SN, Espindola JM (1984) The 1982 eruptions of El Chichon volcano, Mexico: stratigraphy of pyroclastic deposits. *Journal of Volcanology and Geothermal Research* 23: 11-37
- Simakin A, Armienti P, Epel'baum M (1999) Coupled degassing and crystallization: experimental study at continuous pressure drop with application to volcanic bombs. *Bulletin of Volcanology* 61: 275-287
- Sparks RSJ (1986) The dimensions and dynamics of volcanic eruption columns. *Bulletin of Volcanology* 48: 3-15
- Sparks RSJ, Brazier S (1982) New evidence for degassing processes during explosive eruptions. *Nature* 295: 218-220
- Sparks RSJ, Bursik MI, Ablay GJ, Thomas RME, Carey SN (1992) Sedimentation of tephra by volcanic plumes. II. Controls on thickness and grain-size variations of tephra fall deposits. *Bulletin of Volcanology* 54: 685-695

- Sparks RSJ, Bursik MI, Carey SN, Gilbert JS, Glaze LS, Sigurdsson H, Woods AW  
(1997) Volcanic Plumes. John Wiley & Sons Chichester, 574 pp
- Spera FJ (2000) Physical properties of magma. In: Sigurdsson H (ed) Encyclopedia of  
Volcanoes, Academic Press pp 171-190
- Stevenson RJ, Bagdassarov NS, Dingwell DB, Romano C (1998) The influence of trace  
amounts of water on the viscosity of rhyolites. *Bulletin of Volcanology* 60: 89-97
- Suzuki-Kamata K, Kamata H, Bacon CR (1993) Evolution of the caldera-forming  
eruption at Crater Lake, Oregon, indicated by component analysis of lithic  
fragments. *Journal of Geophysical Research* 98: 14059-14074
- Swanson DA (1990) A decade of dome growth at Mount St. Helens, 1980-90.  
*Geoscience Canada* 17: 154-157
- Swanson DA, Dzurisin D, Holcomb RT, Iwatsubo EY, Chadwick WW, Casadevall  
TJ, Ewert JW, Heliker CC (1987) Growth of the lava dome at Mount St. Helens,  
Washington (USA), 1981-1983. *Geol Soc Am Spec Pap* 212: 1-16
- Swanson DA, Holcomb RT (1990) Regularities in growth of the Mount St. Helens dacite  
dome, 1980-1986. In: Fink J (ed) *Lava Flows and Domes*, Springer-Verlag pp 3-  
24
- Thomas N, Jaupart C, Vergnolle S (1994) On the vesicularity of pumice. *Journal of  
Geophysical Research* 99: 15,633-15,644
- Toramaru A (1988) Formation of propagation pattern in two-phase flow systems with  
application to volcanic eruptions. *Geophysical Journal* 95: 613-623

- Toramaru A (1989) Vesiculation process and bubble size distributions in ascending magmas with constant velocities. *Journal of Geophysical Research* 94: 17523-17542
- Toramaru A (1990) Measurement of bubble size distributions in vesiculated rocks with implications for quantitative estimation of eruptive processes. *Journal of Volcanology and Geothermal Research* 43: 71-90
- Touloukian YS, Judd WR, Roy RF (1981) *Physical Properties of Rocks and Minerals*. McGraw-Hill New York, 548 pp
- Ui T, Matsuwo N, Sumita M, Fujinawa A (1999) Generation of block and ash flows during the 1990-1995 eruption of Unzen Volcano, Japan. *Journal of Volcanology and Geothermal Research* 89: 123-137
- Voight B, Elsworth D (2000) Instability and collapse of hazardous gas-pressurized lava domes. *Geophysical Research Letters* 27: 1- 4
- Voight B, Sparks RSJ, Miller AD, Stewart RC, Hoblitt RP, Clarke A, Ewart J, Aspinall WP, Baptie B, Calder ES, Cole P, Druitt TH, Hartford C, Herd RA, Jackson P, Lejeune AM, Lockhart AB, Loughlin SC, Luckett R, Lynch L, Norton GE, Robertson R, Watson IM, Watts R, Young SR (1999) Magma flow instability and cyclic activity at Soufrière Hills Volcano, Montserrat, British West Indies. *Science* 283: 1138-1142
- Waitt RB, Dzurisin D (1981) Proximal air-fall deposits from the May 18 eruption; stratigraphy and field sedimentology. *US Geological Survey Professional Paper* 1250: 601-616

- Walker GPL (1973) Explosive volcanic eruptions - a new classification scheme. *Geol Rundsch* 62: 431-446
- Westrich HR, Eichelberger JC (1994) Gas transport and bubble collapse in rhyolitic magma: an experimental approach. *Bulletin of Volcanology* 56: 447-458
- Whitham A, Sparks R (1986) Pumice. *Bulletin of Volcanology* 48: 209-223
- Wilson CJN, Hildreth W (1997) The Bishop Tuff: new insights from eruptive stratigraphy. *Journal of Geology* 105: 407-439
- Wilson CJN, Walker GPL (1985) The Taupo eruption, New Zealand. I. General aspects. *Philosophical Transactions of the Royal Society of London A* 314: 199-228
- Wilson L, Sparks RSJ, Walker GPL (1980) Explosive volcanic eruptions -IV. The control of magma properties and conduit geometry on eruption column behaviour. *Geophys J R Astr Soc* 63: 117-148
- Wilson L, Walker GPL (1987) Explosive volcanic eruptions - VI. Ejecta dispersal in plinian eruptions: the control of eruption conditions and atmospheric properties. *Geophys J R Astr Soc* 89: 657-679
- Wolf KJ, Eichelberger JC (1997) Syneruptive mixing, degassing, and crystallization at Redoubt Volcano, eruption of December, 1989 to May 1990. *Journal of Volcanology and Geothermal Research* 75: 19-37
- Woods AW (1988) The fluid-dynamics and thermodynamics of eruption columns. *Bulletin of Volcanology* 50: 169-193
- Woods AW, Bower SM (1995) The decompression of volcanic jets in a crater during explosive volcanic eruptions. *Earth and Planetary Science Letters* 131: 189-205

Woods AW, Koyaguchi T (1994) Transitions between explosive and effusive eruptions  
of silicic magmas. *Nature* 370: 641-644